

Analysis of Curved Frequency Selective Surfaces

by

**Zvonimir Sipus
Marko Bosiljevac
Sinisa Skokic**

SUBMITTED BY: Prof. Zvonimir Sipus
Faculty of Electrical Engineering and Computing
University of Zagreb
Unska 3
Zagreb, HR-10000, Croatia

16 May 2008

REPORT DOCUMENTATION PAGE				Form Approved OMB No. 0704-0188	
Public reporting burden for this collection of information is estimated to average 1 hour per response, including the time for reviewing instructions, searching existing data sources, gathering and maintaining the data needed, and completing and reviewing the collection of information. Send comments regarding this burden estimate or any other aspect of this collection of information, including suggestions for reducing the burden, to Department of Defense, Washington Headquarters Services, Directorate for Information Operations and Reports (0704-0188), 1215 Jefferson Davis Highway, Suite 1204, Arlington, VA 22202-4302. Respondents should be aware that notwithstanding any other provision of law, no person shall be subject to any penalty for failing to comply with a collection of information if it does not display a currently valid OMB control number. PLEASE DO NOT RETURN YOUR FORM TO THE ABOVE ADDRESS.					
1. REPORT DATE (DD-MM-YYYY) 5-10-2007		2. REPORT TYPE Final Report		3. DATES COVERED (From – To) 5 April 2007 - 05-Apr-08	
4. TITLE AND SUBTITLE Analysis of Curved Frequency Selective Surfaces			5a. CONTRACT NUMBER FA8655-07-1-3018		
			5b. GRANT NUMBER 		
			5c. PROGRAM ELEMENT NUMBER 		
6. AUTHOR(S) Dr. Zvonimir Sipus			5d. PROJECT NUMBER 		
			5d. TASK NUMBER 		
			5e. WORK UNIT NUMBER 		
7. PERFORMING ORGANIZATION NAME(S) AND ADDRESS(ES) University of Zagreb Unska 3 Zagreb HR-10000 Croatia				8. PERFORMING ORGANIZATION REPORT NUMBER N/A	
9. SPONSORING/MONITORING AGENCY NAME(S) AND ADDRESS(ES) EOARD PSC 821 BOX 14 FPO AE 09421-0014				10. SPONSOR/MONITOR'S ACRONYM(S) 	
				11. SPONSOR/MONITOR'S REPORT NUMBER(S) Grant 07-3018	
12. DISTRIBUTION/AVAILABILITY STATEMENT Approved for public release; distribution is unlimited.					
13. SUPPLEMENTARY NOTES					
14. ABSTRACT This report results from a contract tasking University of Zagreb as follows: 1. Formulation of the problem. First period of the project is reserved for making a detailed formulation of the problem. Our starting point will be the existing MoM based program for analyzing patch arrays on placed on cylindrical and spherical structures (programs CyMPA and SMiPA that are developed under the projects F61775-99-WE040 and F61775-01-WE024). The main difference between radiation and scattering problems is in the excitation model. We will assume two types of excitations: a plane wave impinging on a curved periodic structure (needed for calculating RCS of the curved FSS), and the far field radiation pattern of an antenna inside the radome (needed for calculating the radiation pattern of the antenna with radome; the radome is usually in the far-field region). Both the plane wave and the field radiated by the primary antenna will be expanded into a series of cylindrical or spherical harmonics. Another large difference is in the size of the considered structure: the radome is usually very large in terms of the wavelength. 2. Modeling the RCS/radiation pattern with approximate way of calculating mutual coupling between patches/apertures. The process of determining the scattered field from the FSS radome can be divided into two steps. In the first step the real or equivalent currents on patches or slots will be determined, while the electromagnetic field radiated by this currents will be computed in the second step. The array size will be the reason why the mutual coupling effects will be calculated in an approximate way: each patch or slot will be considered in an equivalent infinite planar or cylindrical environment. By this we will be able to analyze conformal arrays of patches and apertures of different size. 3. Modeling the RCS/radiation pattern with rigorous way of calculating mutual coupling between patches/apertures. 4. Development of experimental model.					
15. SUBJECT TERMS EOARD, radar, Conformal Array Antennas, Antennas					
16. SECURITY CLASSIFICATION OF:			17. LIMITATION OF ABSTRACT UL	18. NUMBER OF PAGES 76	19a. NAME OF RESPONSIBLE PERSON GEORGE W YORK, Lt Col, USAF
a. REPORT UNCLAS	b. ABSTRACT UNCLAS	c. THIS PAGE UNCLAS			19b. TELEPHONE NUMBER (Include area code) +44 (0)20 7514 4354

TABLE OF CONTENTS

1 INTRODUCTION.....	2
2 PROJECT OBJECTIVE AND REALIZED OUTCOMES	5
3 PROJECT OUTCOMES – ANALYSIS METHOD	8
3.1 ANALYSIS OF FREQUENCY SELECTIVE SURFACES ON SPHERICAL STRUCTURES	9
3.1.1 <i>Introduction.....</i>	9
3.1.2 <i>Method of Analysis</i>	10
3.1.4 <i>Mutual coupling calculation</i>	15
3.1.5 <i>Hybrid method for the analysis of curved FSS.....</i>	19
3.1.6 <i>Subarray approach of analyzing curved FSS.....</i>	24
3.1.7 <i>Calculation of radiation pattern of a FSS reflector system.....</i>	25
3.1.8 <i>The analysis of dual structure – slots in the curved PEC surface.....</i>	28
3.1.9 <i>Structure of the program.....</i>	31
4 PROJECT OUTCOMES - RESULTS	33
4.1 NUMERICAL RESULTS	34
4.1.1 <i>Scattering properties of curved FSS.....</i>	34
4.1.2 <i>Subarray approach of analyzing curved FSS.....</i>	52
4.1.3 <i>Radiation pattern of the FSS reflector system and of the FSS radome</i>	55
4 CONCLUSIONS	63
5 BIBLIOGRAPHY	66
6 APPENDIX.....	68
6.1 cFSS PROGRAM - TEXT FILE INTERFACE.....	69
6.1.1 <i>The cFSS.in file.....</i>	70
6.1.2 <i>Description of the output files</i>	72

1 INTRODUCTION

Introduction

A conformal antenna or a periodic structure can be defined as a structure which conforms to a surface whose shape is mainly determined by considerations other than electromagnetic, e.g. aerodynamic or hydrodynamic considerations [1]. In other words, conformal structures can be mounted on various airborne objects (fighter jets, smart missiles, rockets) without disturbing their aerodynamical properties. This definition should be broadened with antennas or periodic structures whose shape is not planar and is determined with specific electromagnetic reasons like coverage requirements. For example, arrays on cylindrical structures offer a possibility either to create directed beams in arbitrary direction in horizontal plane, or to create an omnidirectional pattern [1]. Spherical arrays have the capability of directing single or multiple beams through a complete hemisphere. Therefore, spherical arrays are a good candidate for satellite terminals, telemetry and command applications, performed from a ground station [2], [3]. Curved periodic structures are mainly used in multi-frequency reflector systems where one reflector is reflective in one frequency band and it is transparent in another frequency band [4]. Curved periodic structures are also used in realization of frequency selective radomes, i.e. radomes that provide mechanical and electromagnetic protection.

Analysis methods for planar frequency selective surfaces (FSS) have matured and are nowadays commonly included in many commercial electromagnetic solvers. Curved FSS on the other hand is still however quite a hot topic. The main reason for such a situation is that the fundamental properties of planar FSS, namely the periodicity and the infinite extent of the surface, are lost when analyzing curved FSS. The absence of this infinite periodicity means that the analysis can no longer be simplified by observing only a single unit cell, and therefore the analysis of the entire FSS has to be done at once.

Curved FSS are mostly used for obtaining frequency selective subreflectors in multifrequency reflector systems, or for making frequency selective radomes (Fig. 1.1). In the first case, curved FSS allows the reflector system to be used for dual (or more) frequency bands, i.e. there is a separate feed antenna for each frequency band. In the second case, curved FSS enables mechanical and electromagnetic protection of objects (mostly antennas) inside the radome.

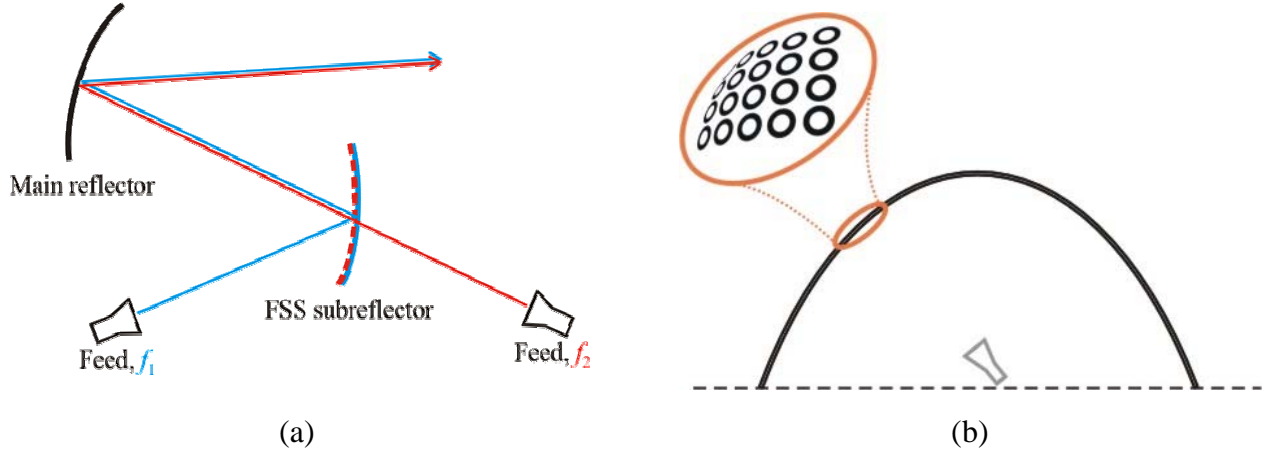


Figure 1.1 Applications of curved FSS: (a) multifrequency reflector system; (b) frequency selective radome.

Since structures (radomes or reflectors) that contain FSS are electrically very large, the geometrical optics is commonly used for the analysis. In this classical approach, a bundle of rays is launched from the source (usually an antenna inside the radome or an antenna exciting a subreflector). Each ray is traced forward from the source to the curved FSS. The transmitted ray is determined by considering the transmission coefficient of the equivalent planar FSS. The far field is then obtained by implementing the equivalence principle. The main drawback of this approach is that the transmission through the structure is calculated using the locally planar approximation, ignoring the influence of the curvature and the finiteness of the FSS on its transmission/reflection properties.

FSS (i.e. the large finite array) in the proposed new approach is divided into N subarrays that are separately analyzed using a rigorous full-wave method. The subarrays have to overlap because the same element in a subarray will have different induced physical or equivalent currents depending on whether it is simulated as an inner element or an edge element, since the edge elements “do not see” the rest of the array environment. The scattered field is calculated as a superposition of the electromagnetic field radiated by the inner parts of N subarrays. This divides an extremely large-scale electromagnetic problem into a sum of simple (small-size) problems and allows the possibility to analyze a general conformal FSS structure using such overlapping subarrays, that is, spherical periodic structures of an appropriate (local) radius of curvature.

2 PROJECT OBJECTIVE AND REALIZED OUTCOMES

Project objective and realized outcomes

We have proposed a 12-month effort to develop software for analyzing curved frequency selective surfaces (curved FSS) mounted on single- and double-curved structures. Two types of periodic structures are to be analyzed: structures with patches and structures with apertures. The developed program is planned to calculate the following characteristics: (a) reflection (radar cross-section) from the curved structure, (b) transmission (radiation pattern) through the curved structure, (c) losses due to the presence of the periodic structure. Our starting point were the existing MoM based programs for analyzing patch arrays placed on cylindrical and spherical structures (programs CyMPA and SMiSPA that were developed under the projects F61775-99-WE040 and FA8655-04-1-3050) and in a way this project is a continuation and an upgrade of these programs.

The realized outcomes of the project are:

- Program “cFSS” that analyzes spherical frequency selective periodic structures consisting of circular ring elements. Circular rings as elements for building curved FSS were selected due to their good polarization and resonant frequency properties. The program calculates:
 - Current distribution at each ring in the subarray of the analyzed FSS without mutual coupling taken into account,
 - Current distribution at each ring in the subarray of the analyzed FSS with mutual coupling between the ring elements rigorously taken into account,
 - Scattered field of the analyzed subarray with and without mutual coupling taken into account,
 - Transmission coefficient of the analyzed subarray,
 - Electromagnetic properties of the whole curved FSS structure, obtained by calculating scattered electromagnetic field of the whole FSS (the needed current distribution is obtained by solving a set of subarray problems),
 - Radiation pattern of the FSS reflector system where the primary feed is characterized with the known far-field radiation pattern,
 - Radiation pattern of the FSS radome system where, as FSS elements, circular annular apertures are considered (so-called dual problem).

Due to the complexity and the size of the analyzed problems a series of numerical acceleration techniques is used in order to trim the computation time. First, the analyzed conformal FSS is divided into overlapping spherical subarrays of an appropriate (local) radius of curvature. This approach is significantly more efficient because such smaller subarrays are much easier to analyze, and also allows the possibility to analyze arbitrary conformal structures. In the final step of the algorithm these subarrays with their parameters are all merged together into a global MoM matrix which when solved gives the solution of the entire problem.

Next, in order to efficiently calculate the mutual coupling terms, needed for every pair of elements in the array, we introduce two additional potential like auxiliary functions, which contain the information about the coordinates only in respective arguments of a product of Legendre and exponential functions. The simplification is achieved through application of the additional theorem for associated Legendre functions, which allows the functions to be transformed from one coordinate system to another very easily. This results in a significant reduction in the number of evaluations of the highly oscillating integrals, which are needed when evaluating element-to-element interaction. Apart from the significant reduction in computation time this method proved to be also more accurate compared to the standard element-by-element approach.

Finally, in order to further reduce the computation time a hybrid method was developed, which combines the spectral domain approach with either a basic free space method or Uniform Theory of Diffraction, a choice that depends on the actual analyzed problem. The essential idea of this hybrid method is to extract the slowly varying core of the Green's function from the MoM coupling integrals and calculate it using an appropriate simpler and faster method. The reason for introducing this step is in the fact that the used spectral domain approach is an excellent choice for analyzing multilayered problems only to a certain structure size (compared to wavelength). For larger problems the method is extremely time consuming, and therefore not practical for FSS analysis. The needed acceleration is achieved through the mentioned extraction, and the use of simpler methods for the extracted analysis problem that, consequently, have to approximate the multilayered structure with a homogeneous space.

All together these techniques allow that a very large FSS structure can be analyzed in reasonable time, thus saving the time needed to be invested into the development of such structures.

The developed programs are written in FORTRAN program language since there is no faster programming language for computational physics (i.e. computational electromagnetics). The program is independent of the machine, and can be compiled and ran on every machine that has a FORTRAN 90 compiler. Furthermore, for MS Windows PC environment, a graphical user interface is developed to allow for easier setting of input parameters, and to obtain graphical presentation of the results. On other machines or operating systems communication with the program is made via input/output ASCII files. In more details, the input file should be filled before running the program, and the results are written into the output file that can be graphically presented by any data displaying program.

3 PROJECT OUTCOMES – ANALYSIS METHOD

3.1 Analysis of frequency selective surfaces on spherical structures

3.1.1 Introduction

The approaches to the analysis of curved FSS can be divided into several groups [4]:

- 1. Finite structure approach**

In this approach there are no simplifications, current distribution on each element in the array environment is rigorously determined. In order to obtain that, special mathematical techniques are needed for such a large-scale problem. Furthermore, this approach will require large computational time, which is not practical in the design process.

- 2. Spherical-wave spectrum approach**

In this approach the incoming electromagnetic waves are represented as sum of spherical wave harmonics. Therefore, transmission and reflection coefficients of curved FSS are locally determined for each spherical wave using local curvature and periodicity information.

- 3. Locally planar FSS approach**

This is the simplest approach (and therefore less accurate). The ray techniques are used to represent the radiation pattern of the antenna inside the radome or of the feed antenna of the reflector system. The amplitude and the phase of each ray are corrected using transmission and reflection coefficients of the equivalent planar FSS, and the final radiation pattern is obtained using physical optics (PO) principle. The main drawback of this approach is that the transmission through the structure is calculated using the locally planar approximation, ignoring the influence of the curvature and the finiteness of the FSS on its transmission/reflection properties.

Our approach belongs to the second group. The curved FSS (i.e. the large finite array) is divided into N subarrays, which are separately analyzed using a rigorous full-wave method. Each subarray is locally approximated as a spherical FSS with a local radius of curvature (see Fig 3.1) The subarrays have to overlap because the same element in a subarray will have different induced physical or equivalent currents depending on whether it is simulated as an inner element or an edge element since the edge elements “do not see” the rest of the array environment. The scattered field is then calculated as a superposition of the electromagnetic field radiated by the inner parts of N subarrays. This divides an extremely large-scale electromagnetic problem into a sum of simple (small-size) problems. Consequently, we obtain the possibility to analyze a general conformal FSS structure using overlapping subarray approach, that is, by analyzing spherical periodic structures of an appropriate (local) radius of curvature.

The FSS structures considered in this paper are composed out of circular ring elements because of their good polarization properties and insensitivity of their resonant frequency on the angle of the incident plane wave [5].

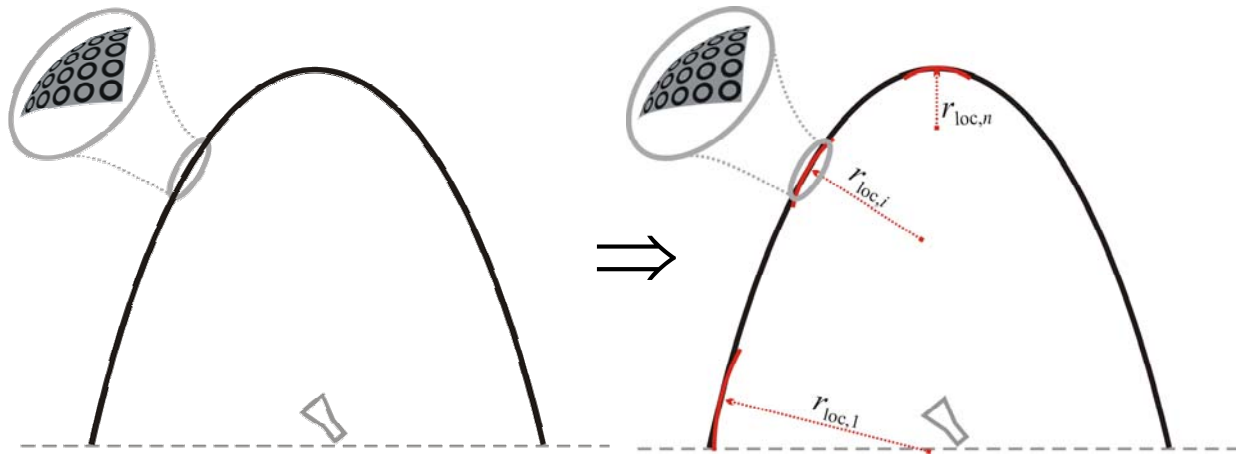


Figure 3.1. A doubly curved frequency selective radome with circular ring elements. Locally, the curved FSS can be approximated as a spherical FSS.

3.1.2 Method of Analysis

The geometry of the problem is given in Fig. 3.2. Circular rings of average radius R (radius to the center of the conductor) and conductor width W are embedded in a spherical structure. The coordinates of the ring center are $\theta = \theta^{ring}$ and $\phi = \phi^{ring}$. All rings have the same dimensions and their position can be obtained by rotating the central ring (the red ring in Fig.3.2.) around the sphere center. In other words, the center of the central ring is defined with $\theta^{ring} = 0^\circ$. Notice that there is no simple expression for the ring coordinates of a generally positioned ring. The rings are distributed along a hexagonal grid (as shown in Fig. 3.2.a) or along an icosahedral grid (Fig 3.2.b), which in both cases approximates the triangular grid of the equivalent planar FSS.

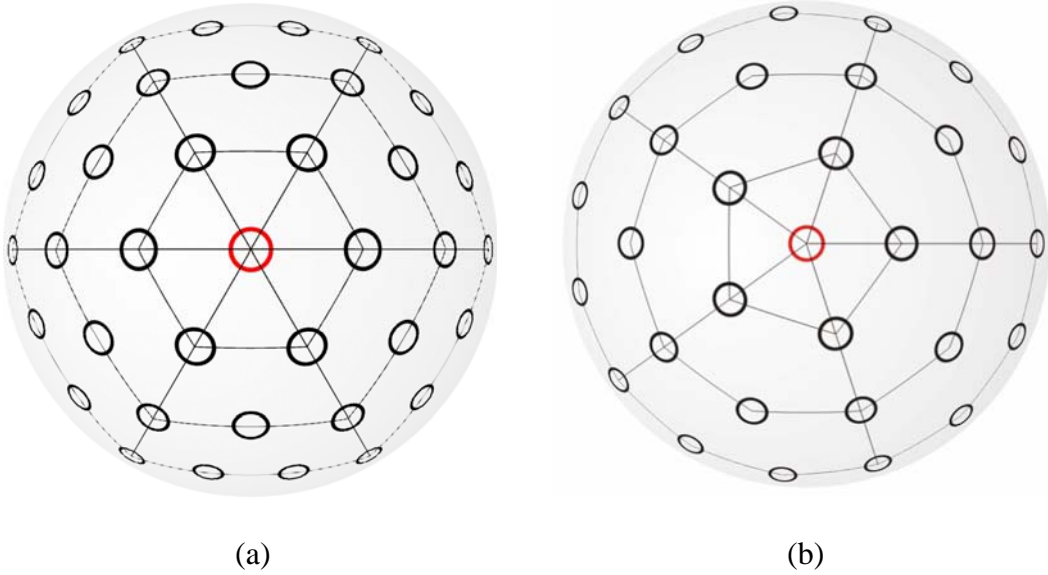


Figure 3.2. Geometry of the spherical FSS; (a) hexagonal structure, (b) icosahedral structure

The analysis approach is based on solving the integral equation for the electric field (EFIE), and on the moment method (MoM), where the elements of the MoM matrix are calculated in the spectral domain. We have selected entire-domain basis functions to represent the ring current, and the test functions were chosen following the Galerkin's approach.

Planar, circular-cylindrical and spherical multilayer structures can be analyzed by applying the adequate version of a two-dimensional Fourier transformation to both currents and EM fields in the directions where the structure is homogeneous [6], [7]. In the cylindrical case the Fourier transformation in the axial direction and Fourier series in the ϕ direction is applied, while in the spherical case (see Fig. 1) one performs the vector-Legendre transformation in θ and ϕ directions [8], [7]. Consequently, the EM fields excited by one spherical component have the same harmonic variation as the source, and the original three-dimensional problem is transformed to a spectrum of one-dimensional problems, which is much easier to solve.

The vector-Legendre transformation is defined as [8], [9]

$$\tilde{\mathbf{J}}(r, n, m) = \int_{-\pi}^{\pi} \int_0^{\pi} \frac{1}{\sqrt{2\pi S(n, m)}} \bar{\mathbf{L}}(n, m, \theta) \mathbf{J}(r, \theta, \phi) e^{-jm\phi} \sin \theta d\theta d\phi \quad (1a)$$

$$\mathbf{J}(r, \theta, \phi) = \sum_{n=0}^{\infty} \sum_{m=-n}^n \frac{1}{\sqrt{2\pi S(n, m)}} \bar{\mathbf{L}}(n, m, \theta) \tilde{\mathbf{J}}(r, n, m) e^{jm\phi} \quad (1b)$$

$$\bar{\mathbf{L}}(n, m, \theta) = \begin{bmatrix} P_n^{|m|}(\cos \theta) \sqrt{n(n+1)} & 0 & 0 \\ 0 & \frac{\partial P_n^{|m|}(\cos \theta)}{\partial \theta} & \frac{-jm P_n^{|m|}(\cos \theta)}{\sin \theta} \\ 0 & \frac{jm P_n^{|m|}(\cos \theta)}{\sin \theta} & \frac{\partial P_n^{|m|}(\cos \theta)}{\partial \theta} \end{bmatrix} \quad (1c)$$

$$S(n, m) = \frac{2n(n+1)(n+|m|)!}{(2n+1)(n-|m|)!} \quad (1d)$$

Here $P_n^{|m|}(\cos \theta)$ denotes the associated Legendre function. Comparing to the original definition from [8], we have extended the definition of vector-Legendre transformation to include the r vector component and we have included the same factor $1/\sqrt{2\pi S(n,m)}$ in both forward and inverse transformation in a symmetric way [9]. Furthermore, as a second step in obtaining numerically stable procedure, we have introduced normalized Legendre polynomials $\bar{P}_n^{|m|}$ and their derivatives as [9] :

$$\bar{P}_n^{|m|} = P_n^{|m|} \sqrt{\frac{(n-|m|)!}{(n+|m|)!}}, \quad \frac{\partial \bar{P}_n^{|m|}(\cos \theta)}{\partial \theta} = \frac{\partial P_n^{|m|}(\cos \theta)}{\partial \theta} \sqrt{\frac{(n-|m|)!}{(n+|m|)!}}. \quad (2)$$

Notice that for the normalization factor we have chosen the rapidly growing term inside the term $\sqrt{S(n,m)}$ (see eq. (1.d)). The term $\bar{L}/\sqrt{S(n,m)}$ in expressions (1a) and (1b) enables us to calculate normalized Legendre polynomials instead of Legendre polynomials, and $2n(n+1)/(2n+1)$ instead of $S(n,m)$, both of them being numerically stable. Thus, divisions of very large numbers are avoided.

The recursive equations for the normalized Legendre polynomials and their derivatives are:

$$\begin{aligned} \bar{P}_{n+1}^{|m|}(z) \sqrt{(n+1+|m|)(n+|m|)} &= \frac{1}{n-|m|+1} \cdot \\ &\cdot \left((2n+1) z \bar{P}_n^{|m|}(z) \sqrt{(n+|m|)(n-|m|+1)} - (n+|m|) \bar{P}_{n-1}^{|m|}(z) \sqrt{(n-|m|)(n-|m|+1)} \right), \end{aligned} \quad (3a)$$

$$(z^2 - 1) \frac{\partial \bar{P}_n^{|m|}(z)}{\partial z} \sqrt{n+|m|} = n z \bar{P}_n^{|m|}(z) \sqrt{n+|m|} - (n+|m|) \bar{P}_{n-1}^{|m|}(z) \sqrt{n-|m|}. \quad (3b)$$

The unknown current distribution is determined by solving the electric field integral equation (EFIE) numerically via Method of Moments (MoM). The elements of the MoM matrix are calculated in the spectral domain

$$Z_{ji} = - \sum_{m=-\infty}^{\infty} \sum_{n=|m|}^{\infty} r_{ring}^2 \tilde{\mathbf{J}}_j^T(r_{ring}, n, -m) \tilde{\mathbf{G}}(n, m, r_{ring} | r_{ring}) \tilde{\mathbf{J}}_i(r_{ring}, n, m), \quad (4)$$

where $\tilde{\mathbf{J}}(r_{ring}, n, m)$ represents the basis and test functions in the spectral domain.

There are two basic approaches to determine the Green's function of general multilayer structures: either to analytically derive an expression for it and then to code that expression, or to develop a numerical routine for the complete calculation. The analytic approach requires less computer time than the numerical approach. However, it is a very laborious process to analytically determine the Green's functions for substrates with more than two layers. Therefore, in such cases it is convenient to use a numerical algorithm that determines the Green's function directly. Another disadvantage of the analytic approach is that it is valid only for a very specific

geometry, so that a new derivation of the Green's functions is needed for even a slight change in the geometry, for example if the rings are rearranged inside the multilayer structure. For that reason we have developed the G1DMULT algorithm that calculates the spectral-domain Green's functions for planar, circular-cylindrical and spherical multilayer structures, i.e. the algorithm uses advantages of transforming the problem to the spectral domain. More details about the G1DMULT algorithm are given in [7].

The far field radiation pattern of a single ring element is obtained as follows. If we consider the θ - and ϕ -component of the electric field in the outermost region with the r -coordinate larger than the r -coordinate of the ring, we have only outward-traveling waves described by the Schelkunoff spherical Hankel function of the second kind $\hat{H}_n^{(2)}(k_0 r)$ [6], [10]. Therefore, in the outermost region we can relate the θ - and ϕ -component of the electric field with different r -coordinates r_1 and r_2 ($r_1 \gg r_2$) as

$$\tilde{E}_\theta(r_1, n, m) = \tilde{E}_\theta(r_2, n, m) \frac{r_2}{r_1} \frac{\hat{H}_n^{(2)'}(k_0 r_1)}{\hat{H}_n^{(2)'}(k_0 r_2)} \approx \tilde{E}_\theta(r_2, n, m) \frac{j^n r_2}{\hat{H}_n^{(2)'}(k_0 r_2)} \frac{e^{-jk_0 r_1}}{r_1} \quad (5a)$$

$$\tilde{E}_\phi(r_1, n, m) = \tilde{E}_\phi(r_2, n, m) \frac{r_2}{r_1} \frac{\hat{H}_n^{(2)}(k_0 r_1)}{\hat{H}_n^{(2)}(k_0 r_2)} \approx \tilde{E}_\phi(r_2, n, m) \frac{j^{n+1} r_2}{\hat{H}_n^{(2)}(k_0 r_2)} \frac{e^{-jk_0 r_1}}{r_1}. \quad (5b)$$

Here r_1 represents the r -component of the far field pattern. For numerical reasons it is practical to select the value of r_2 a bit larger than the radius of the whole antenna structure. The final solution is obtained by superposing all spectral solutions, see eq. (1b). The equations (5a) and (5b) can be easily obtained from the general EM field representation for spherical multilayer problems [7].

The radiation pattern of the array is obtained as a superposition of the fields excited by each ring. For that purpose it is convenient to introduce local coordinate systems with the origins located at the center of each ring. The local coordinate system “follows” the ring when it is moved from the central position, i.e. the z' axis of the local system is oriented normal to the ring center. The coordinates in the local coordinate system are determined using the following equations (see [11] for details)

$$\cos \theta' = \sin(\alpha_n) \sin \theta \cos(\phi - \beta_n) + \cos(\alpha_n) \cos \theta \quad (6a)$$

$$\cot \phi' = \frac{\cos(\alpha_n) \sin \theta \cos(\phi - \beta_n) - \sin(\alpha_n) \cos \theta}{\sin \theta \sin(\phi - \beta_n)} \quad (6b)$$

where α_n and β_n are the θ - and ϕ -coordinates of the center of each ring in the global coordinate system. The unit vectors in the local coordinate system can be determined from the following equations

$$\hat{e}_{\theta'} = -\frac{\cos \theta \sin \alpha_n \cos(\phi - \beta_{nm}) - \sin \theta \cos \alpha_n}{\sin \theta'} \hat{e}_\theta + \frac{\sin \alpha_n \sin(\phi - \beta_{nm})}{\sin \theta'} \hat{e}_\phi \quad (7a)$$

$$\hat{e}_{\phi'} = -\frac{\sin \alpha_n \sin(\phi - \beta_{nm})}{\sin \theta'} \hat{e}_\theta - \frac{\cos \theta \sin \alpha_n \cos(\phi - \beta_{nm}) - \sin \theta \cos \alpha_n}{\sin \theta'} \hat{e}_\phi \quad (7b)$$

Combining equations (6) and (7) one gets the θ - and ϕ -field components of the field excited by the antenna element with center coordinates (α_n, β_{nm})

$$E_{\theta, \alpha_n \beta_{nm}} = - \left[\frac{\cos \theta \sin \alpha_n \cos(\phi - \beta_{nm}) - \sin \theta \cos \alpha_n}{\sin \theta'} f_{\theta}(\theta', \phi') + \frac{\sin \alpha_n \sin(\phi - \beta_{nm})}{\sin \theta'} f_{\phi}(\theta', \phi') \right] \quad (8a)$$

$$E_{\phi, \alpha_n \beta_{nm}} = \left[\frac{\sin \alpha_n \sin(\phi - \beta_{nm})}{\sin \theta'} f_{\theta}(\theta', \phi') - \frac{\cos \theta \sin \alpha_n \cos(\phi - \beta_{nm}) - \sin \theta \cos \alpha_n}{\sin \theta'} f_{\phi}(\theta', \phi') \right] \quad (8b)$$

Here f_{θ} and f_{ϕ} represent the θ and ϕ components of the far field pattern of the central ring (i.e. of the ring with the center at $\theta = 0$).

3.1.3 Definition of the transmission coefficient

The transmission coefficient T for the curved FSS constructed out of circular ring elements is defined as the ratio of the magnitude of the total E-field (incident and scattered) at the point z , and the magnitude of the E-field due to the aperture field alone (i.e. in the absence of the array) [14]:

$$T = \frac{|E^{scatt} + E^{aperture}|}{|E^{aperture}|}. \quad (9)$$

The incident field $E^{aperture}$ in the upper expression is calculated as the far field at a distance z in the axial direction radiated by a circular aperture uniformly illuminated with a field of unit amplitude. It can be shown that the field $E^{aperture}$ is equal:

$$\mathbf{E}^{aperture} = \frac{jkR_{aperture}^2}{2z} e^{-jkz}, \quad (10)$$

where $R_{aperture}$ is the radius of the equivalent circular aperture described in Fig. 3.10. In the case of curved FSS printed on a dielectric, the influence of the dielectric slab is included in $E^{aperture}$.

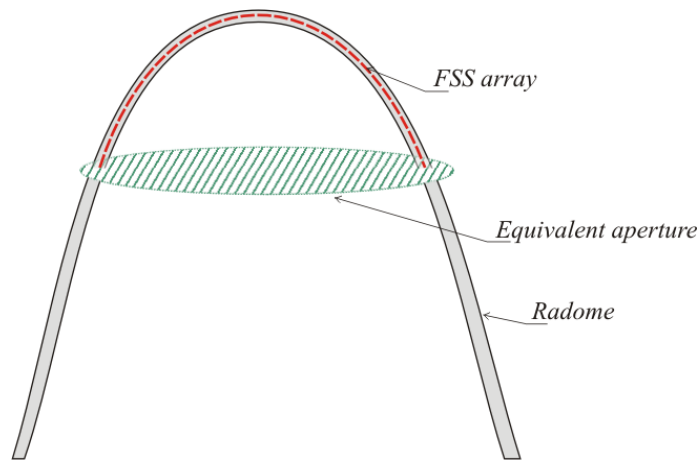


Figure 3.3. Definition of the equivalent aperture needed for transmission coefficient calculation.

3.1.4 Mutual coupling calculation

For the centered ring (i.e. for the ring with the center at the pole), the basis/test functions have simple domain boundaries and it is easy to calculate their vector-Legendre transforms. However, when calculating the mutual coupling between the rings one needs to calculate the vector-Legendre transforms of the basis and test functions with the domain on the ring located at an arbitrary position on the sphere. One approach is to numerically calculate the needed terms using the formulas that connect the global and local coordinate system. In more details, the vector-Legendre transform of the basis/test function located at the displaced ring is:

$$\tilde{\mathbf{J}}_i(r_{ring}, n, m) = \iint_{\text{patch}} \frac{1}{\sqrt{2\pi S(n, m)}} e^{jm\phi} \overline{\mathbf{L}}(n, m, \theta) \cdot \mathbf{J}_i(r_{ring}, \theta', \phi') \sin \theta' d\theta' d\phi' \quad (11)$$

where θ and ϕ are coordinates in the global coordinate system, and the pair θ' and ϕ' are coordinates in the local coordinate system. To illustrate this division into global and local coordinates, equation (11) is written once more as:

$$\tilde{\mathbf{J}}_i(r_{ring}, n, m) = \iint_{\text{patch}} \frac{1}{\sqrt{2\pi S(n, m)}} \underbrace{e^{jm\phi} \overline{\mathbf{L}}(n, m, \theta)}_{\text{global coordinates}} \cdot \underbrace{\mathbf{J}_i(r_{ring}, \theta', \phi') \sin \theta' d\theta' d\phi'}_{\text{local coordinates}} \quad (12)$$

Note that both matrix \mathbf{L} and basis functions \mathbf{J}_i are written with respect to the basis $(\hat{e}_\theta, \hat{e}_\phi, \hat{e}_r)$, which is the basis of the global coordinate system. The connection between local and global coordinate system is given by the following equations [11]:

$$\cos \theta = -\sin \alpha_n \sin \theta' \cos \phi' + \cos \alpha_n \cos \theta' \quad (13a)$$

$$\cot(\phi - \beta_n) = \frac{\cos \alpha_n \sin \theta' \cos \phi' + \sin \alpha_n \cos \theta'}{\sin \theta' \sin \phi'}, \quad (13b)$$

where α_n and β_n are the θ - and ϕ -coordinates of the center of each ring in the global coordinate system. Notice that the local coordinate system “follows” the ring when it is moved from the central position, i.e. the z' axis of the local system is oriented normal to the ring center. The connection between the unit vectors in the global and the local coordinate system is [11]:

$$\hat{e}_\theta = -\frac{\cos \theta \sin \alpha_n \cos(\phi - \beta_n) - \sin \theta \cos \alpha_n}{\sin \theta'} \hat{e}_{\theta'} - \frac{\sin \alpha_n \sin(\phi - \beta_n)}{\sin \theta'} \hat{e}_{\phi'}, \quad (14a)$$

$$\hat{e}_\phi = \frac{\sin \alpha_n \sin(\phi - \beta_n)}{\sin \theta'} \hat{e}_{\theta'} - \frac{\cos \theta \sin \alpha_n \cos(\phi - \beta_n) - \sin \theta \cos \alpha_n}{\sin \theta'} \hat{e}_{\phi'}, \quad (14b)$$

Unfortunately, this approach is very time consuming since for each considered basis/test function one needs to calculate a double integral of rapidly varying functions (for large m and n associate Legendre functions and $\exp(-jm\phi)$ are highly oscillating).

In order to make a more efficient program we have established the following relationship between the vector-Legendre transformation of the basis/test functions with the domain on the central ring (i.e. ring center is defined by $\theta = 0^\circ$), and on the ring whose center has coordinates θ

$= \alpha_n, \phi = \beta_n = 0$. As a first step, two functions $A_r^{J_i}$ and ψ^{J_i} are defined for a basis function \mathbf{J}_i located at the central ring

$$\mathbf{J}_i(r_{ring}, \theta, \phi) = \nabla \times (\hat{r} r_{ring} A_r^{J_i}(r_{ring}, \theta, \phi)) + \nabla \cdot (r_{ring} \psi^{J_i}(r_{ring}, \theta, \phi)). \quad (15)$$

In spherical coordinate system equation (4) can be written as

$$\mathbf{J}_i(r_{ring}, \theta, \phi) = \hat{\theta} \frac{1}{\sin \theta} \frac{\partial A_r^{J_i}}{\partial \phi} - \hat{\phi} \frac{\partial A_r^{J_i}}{\partial \theta} + \hat{\theta} \frac{\partial \psi^{J_i}}{\partial \theta} + \hat{\phi} \frac{1}{\sin \theta} \frac{\partial \psi^{J_i}}{\partial \phi}. \quad (16)$$

At the same time, the basis and test functions can be written as (the direct implementation of the inverse vector-Legendre transformation):

$$\begin{aligned} \mathbf{J}_i(r_{ring}, \theta, \phi) = & \sum_{n=1}^{\infty} \sum_{m=-n}^n \frac{1}{\sqrt{2\pi S(n, m)}} e^{jm\phi} \\ & \cdot \left\{ \hat{\theta} \left[\frac{\partial P_n^{|m|}(\cos \theta)}{\partial \theta} \tilde{J}_{i\theta}(r_{ring}, n, m) - \frac{jm P_n^{|m|}(\cos \theta)}{\sin \theta} \tilde{J}_{i\phi}(r_{ring}, n, m) \right] \right. \\ & \left. + \hat{\phi} \left[\frac{jm P_n^{|m|}(\cos \theta)}{\sin \theta} \tilde{J}_{i\theta}(r_{ring}, n, m) + \frac{\partial P_n^{|m|}(\cos \theta)}{\partial \theta} \tilde{J}_{i\phi}(r_{ring}, n, m) \right] \right\} \end{aligned} \quad (17)$$

If we compare the equations (16) and (17), we can see that the functions $A_r^{J_i}$ and ψ^{J_i} have the following form:

$$\begin{aligned} A_r^{J_i}(r_{ring}, \theta, \phi) = & - \sum_{n=1}^{\infty} \sum_{m=-n}^n \frac{1}{\sqrt{2\pi S(n, m)}} \tilde{J}_{i\phi}(r_{ring}, n, m) P_n^{|m|}(\cos \theta) e^{jm\phi}, \\ \psi^{J_i}(r_{ring}, \theta, \phi) = & \sum_{n=1}^{\infty} \sum_{m=-n}^n \frac{1}{\sqrt{2\pi S(n, m)}} \tilde{J}_{i\theta}(r_{ring}, n, m) P_n^{|m|}(\cos \theta) e^{jm\phi} \end{aligned} \quad (18)$$

The chosen representation is similar to the representation of the electric field via vector and scalar potentials. Note that these formulas do not depend on coordinate system, i.e. they are valid in both global and local coordinate systems. We can connect the representation of $A_r^{J_i}$ and ψ^{J_i} in different coordinate systems using the following property of the associated Legendre functions [12]:

$$P_n^m(\cos \theta') e^{-jm\phi'} = j^m \sqrt{\frac{(n+m)!}{(n-m)!}} \sum_{k=-n}^n j^{-k} \sqrt{\frac{(n-k)!}{(n+k)!}} P_{m,k}^n(\cos \theta_{12}) P_n^k(\cos \theta) e^{-jk\phi} \quad (19)$$

The function $P_{m,k}^n(\cos \theta_{12})$ is defined in [12] and θ_{12} is the angle between the global and the local coordinate system (notice that local coordinates have the prime in notation; the ϕ -coordinate of the center of the displaced ring is zero).

Consequently, by relating equations (18) and (19), one can derive the following form of $A_r^{J_i}$ and ψ^{J_i} with the domain at the displaced ring

$$\begin{aligned}
 A_r^{J_i}(r_{ring}, \theta, \phi) &= - \sum_{n=1}^{\infty} \sum_{k=-n}^n \frac{1}{\sqrt{2\pi S(n, k)}} P_n^{|k|}(\cos \theta) e^{jk\phi} \\
 &\quad \cdot \underbrace{\sum_{m=-n}^n (-j)^{|m|-|k|} P_{|m|, \text{sign}(m)-k}^n(\cos \theta_{12}) \tilde{J}_{i\phi}(r_{ring}, n, m)}_{\tilde{J}_{i\phi}^{\theta_{12}}(r_{ring}, n, k)}, \\
 \psi^{J_k}(r_{ring}, \theta, \phi) &= \sum_{n=1}^{\infty} \sum_{k=-n}^n \frac{1}{\sqrt{2\pi S(n, k)}} P_n^{|k|}(\cos \theta) e^{jk\phi} \\
 &\quad \cdot \underbrace{\sum_{m=-n}^n (-j)^{|m|-|k|} P_{|m|, \text{sign}(m)-k}^n(\cos \theta_{12}) \tilde{J}_{i\theta}(r_{ring}, n, m)}_{\tilde{J}_{i\theta}^{\theta_{12}}(r_{ring}, n, k)}.
 \end{aligned} \tag{20}$$

The basis and test functions in the spectral domain at the displaced ring (with the θ_{12} coordinate of the ring center) are simply obtained by eq. (15), i.e. terms $\tilde{J}_{i\theta}^{\theta_{12}}$ and $\tilde{J}_{i\phi}^{\theta_{12}}$ represent the vector Legendre transformation of the basis/test function located at the displaced ring. In the derivation of the equation (20) we have used the following property of the $P_{m,k}^n$ functions: $P_{m,-k}^n(\cos \theta_{12}) = P_{-m,k}^n(\cos \theta_{12})$.

If the ring center has the ϕ -coordinate different from zero, we can easily express the vector-Legendre transforms of basis/test functions using the following property of Fourier series $\tilde{\mathbf{J}}_{i1}(n, m) = \tilde{\mathbf{J}}_{i2}(n, m) e^{jm(\beta_1 - \beta_2)}$. In other words, when considering a set of rings with the same θ coordinate, one needs to calculate the vector-Legendre transforms of basis /test functions for one ring only.

Finally, in order to implement equation (20) one needs to somehow calculate functions $P_{m,k}^n(\cos \theta_{12})$. It is convenient to use recurrence formulas for such purposes under the condition that they are numerically stable. The applied recurrence formula is [12]:

$$\begin{aligned}
 \sqrt{(n-m)(n+m)} P_{m,k}^n(\cos \theta_{12}) &= \sqrt{(n-k)(n+k)} \cos \theta_{12} P_{m,k}^{n-1}(\cos \theta_{12}) \\
 &\quad + j \frac{\sin \theta_{12}}{2} \left[\sqrt{(n-k-1)(n-k)} P_{m,k+1}^{n-1}(\cos \theta_{12}) + \sqrt{(n+k-1)(n+k)} P_{m,k-1}^{n-1}(\cos \theta_{12}) \right].
 \end{aligned} \tag{21}$$

The applied method for calculating spectral representation of basis/test function is illustrated by the flow chart in Fig. 3.4.

Note that the same approach can be applied to various other electromagnetic problems in which spherical wave representation of the fields is used. For example, a plane wave impinging on a sphere at any angle can be expanded into spherical harmonics and transformed to spectral domain easily by following the same procedure. First, one needs to find the equivalent current sources of a z-traveling plane wave located on a sphere with radius larger than the considered

structure (this sphere represents the outer boundary of the area of interest). The equivalent sources are then rotated for a considered angle [13].

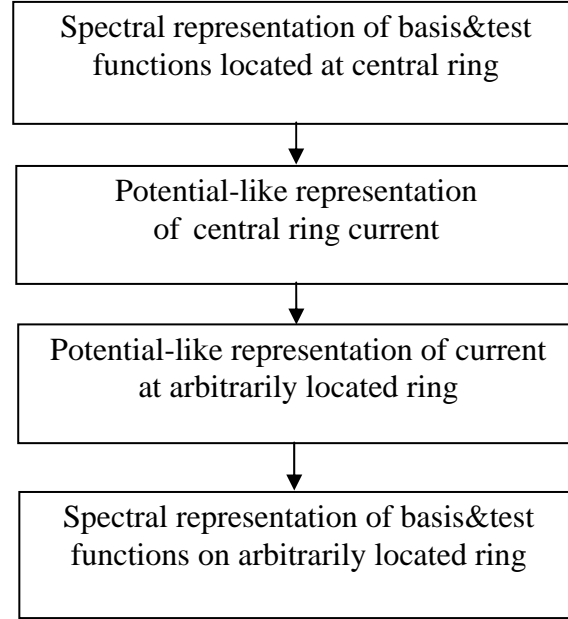


Figure 3.4. Flow chart of the method for calculating spectral representation of basis function

We wanted to evaluate and compare the accuracy of the developed method and the numerical integration approach (Fig. 3.5). We compared the values of Z_{jj} term associated with the dominant entire-domain basis function (equation (4)) when the ring is located at the pole ($\theta = 0^\circ$) and at an arbitrary angle θ . Since Z_{jj} represents the self-coupling term, its value should be the same in all considered cases. Therefore, the value of Z_{jj} term for the ring located at the pole is taken as a reference value when calculating the relative error. The structure dimensions are the same as in the previous example; the radius of the ground plane is 1.0λ . It can be seen that the new method based on the potential-like auxiliary functions has significantly higher accuracy compared to the numerical integration approach. Of course, the accuracy of the latter could also be improved by adding more integration points, but at the expense of increased computation time. Here, it should be pointed out that the new potential-like based approach is already faster than the numerical integration approach by more than two orders of magnitude.

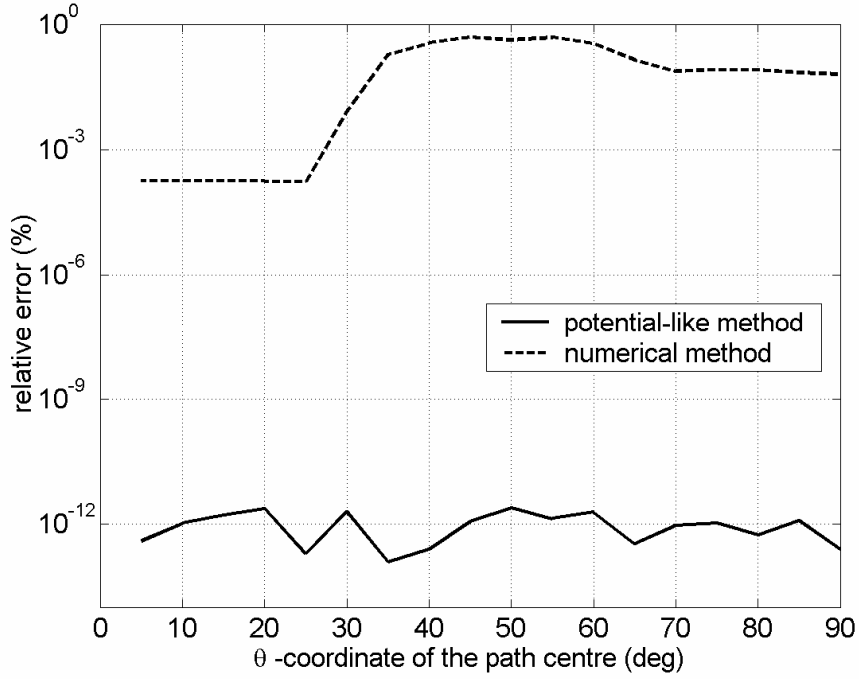


Figure 3.5. Accuracy of calculating self-coupling term Z_{jj} for basis and test functions located at rings with different θ -coordinates.

3.1.5 Hybrid method for the analysis of curved FSS

In order to reduce the number of terms in the Fourier series or vector-Legendre series and to reduce the length of integration in the Fourier transformation we have combined spectral domain method with several asymptotic methods using asymptotic extraction. The basic idea is to subtract the asymptotic part of the Green's function for the analyzed structure, and to calculate it separately [15]. The so-called asymptotic part carries the major contribution to the overall Green's function and the part left after the subtraction is basically the higher-order mode contribution. In essence this means that the asymptotic part is a rough approximation of the analyzed structure without some fine details, multiple layers etc. The major benefit of this approach is that the asymptotic part because of its "simplicity" can now be calculated using a more straightforward methods which can be faster and consume much less computer resources.

To illustrate the concept lets consider the mutual impedance term in the MoM matrix for the spherical FSS:

$$Z_{ji} = - \sum_{m=-\infty}^{\infty} \sum_{n=|m|}^{\infty} r_{ring}^2 \tilde{\mathbf{J}}_j^T(r_{ring}, n, -m) \tilde{\tilde{\mathbf{G}}}(n, m, r_{ring} | r_{ring}) \tilde{\mathbf{J}}_i(r_{ring}, n, m). \quad (22)$$

First we have to extract the asymptotic part and split equation (22) into two parts,

$$\begin{aligned}
Z_{ji} = & - \sum_{m=-\infty}^{\infty} \sum_{n=|m|}^{\infty} r_{ring}^2 \tilde{\mathbf{J}}_j^T(r_{pt}, n, -m) \left\{ \tilde{\tilde{\mathbf{G}}}(n, m, r_{ring} | r_{ring}) - \tilde{\tilde{\mathbf{G}}}_{asym}(n, m, r_{ring} | r_{ring}) \right\} \tilde{\mathbf{J}}_i(r_{ring}, n, m) \\
& - \sum_{m=-\infty}^{\infty} \sum_{n=|m|}^{\infty} r_{ring}^2 \tilde{\mathbf{J}}_j^T(r_{ring}, n, -m) \tilde{\tilde{\mathbf{G}}}_{asym}(n, m, r_{ring} | r_{ring}) \tilde{\mathbf{J}}_i(r_{ring}, n, m)
\end{aligned} \quad (23)$$

By subtracting the asymptotic part from the overall Green's function of the observed structure only the higher order contribution will be evaluated in the first term and the second term can now be calculated using a more efficient method as previously mentioned. As a result reduced length of integration and fewer modes in the inverse Fourier/Legendre series are needed in the computation of the first term in the spectral domain part of Eq. (23). The second term can be calculated in the spatial domain:

$$\begin{aligned}
Z_{ji} = & - \sum_{m=-\infty}^{\infty} \sum_{n=|m|}^{\infty} r_{ring}^2 \tilde{\mathbf{J}}_j^T(r_{pt}, n, -m) \left\{ \tilde{\tilde{\mathbf{G}}}(n, m, r_{ring} | r_{ring}) - \tilde{\tilde{\mathbf{G}}}_{asym}(n, m, r_{ring} | r_{ring}) \right\} \tilde{\mathbf{J}}_i(r_{ring}, n, m) \\
& + \int_{\substack{test \\ function}} \int_{\substack{basis \\ function}} \mathbf{J}_j^T(r_{ring}, \theta, \phi) \tilde{\tilde{\mathbf{G}}}_{asym}(\theta, \phi, r_{ring} | r_{ring}) \mathbf{J}_i(r_{ring}, \theta, \phi) dS dS'
\end{aligned} \quad (24)$$

The selection of the most appropriate method for the calculation of the second term depends on the type of the actual problem. In our case we have a ring type spherical FSS mounted on a thin dielectric sheet that corresponds to a structure comprised out of three layers - air (free space), dielectric sheet and air again. In order to simplify the problem we can replace these three layers with a single layer, or in other words with a homogeneous space surrounding the FSS elements. Green's function describing this problem is basically a free-space Green's function that can be defined as

$$\bar{\mathbf{E}}_j = -\frac{jk}{4\pi} \iint_S \left[\eta \bar{\mathbf{J}} \left(1 + \frac{1}{jkR} \right) - (\eta \bar{\mathbf{J}} \cdot \hat{\mathbf{R}}) \hat{\mathbf{R}} \left(1 + \frac{3}{jkR} - \frac{3}{(kR)^2} \right) \right] \frac{1}{R} e^{-jkR} dS, \quad (25)$$

where $\bar{\mathbf{E}}_j$ is the electric field at a distance R from an electric source $\bar{\mathbf{J}}$ in free space [16]. It is reasonable to assume that the major contribution to the mutual coupling between the individual FSS elements can be described with the coupling in such simplified homogeneous medium. That is why the free space Green's function is selected for the calculation of the asymptotic part in the equation (24). Contribution of the dielectric sheet is of course still present, but hidden in the spectral domain part of the eq. (24).

There are two questions still to be answered: which value to select for effective permittivity of the homogeneous media in the asymptotic problem, and how many modes are needed in spectral representation of the EM fields (with extracted asymptotic parts). Let us first discuss the needed number of modes.

The form of equation (24) that is really coded is

$$\begin{aligned}
Z_{ji} = & - \sum_{m=-N_{\max}}^{N_{\max}} \sum_{n=|m|}^{N_{\max}} r_{\text{ring}}^2 \tilde{\mathbf{J}}_j^T(r_{\text{pt}}, n, -m) \left\{ \tilde{\mathbf{G}}(n, m, r_{\text{ring}} | r_{\text{ring}}) - \tilde{\mathbf{G}}_{\text{asym}}(n, m, r_{\text{ring}} | r_{\text{ring}}) \right\} \tilde{\mathbf{J}}_i(r_{\text{ring}}, n, m) \\
& + \int_{\text{test function}} \int_{\text{basis function}} \mathbf{J}_j^T(r_{\text{ring}}, \theta, \phi) \tilde{\mathbf{G}}_{\text{asym}}(\theta, \phi, r_{\text{ring}} | r_{\text{ring}}) \mathbf{J}_i(r_{\text{ring}}, \theta, \phi) dS dS'
\end{aligned} \tag{26}$$

As an example we have considered an array of circular rings of average radius 2.0 mm (i.e. to the center of the conductor; the conductor width was 0.4 mm), and separation between ring centers 4.9 mm. The rings are printed on a dielectric substrate of thickness 0.0075 mm and permittivity $\epsilon_r = 2.33$. The rings follow the hexagonal grid. The size of the dielectric shell is $r_{\text{ring}} = 37.4$ mm and the array with 3 circles of antenna elements is considered. This curved FSS will be analyzed in details in the next section.

The maximum number of modes N_{\max} is related to the size of the structure. In Figure 3.7 this number ranges from $2.5 \cdot k_0 \cdot r_{\text{ring}}$ to $10.0 \cdot k_0 \cdot r_{\text{ring}}$, respectively (k_0 is the free-space wave number; the effective permittivity used in calculations is $\epsilon_{\text{eff}} = 1.2$). It can be seen that even $3.0 \cdot k_0 \cdot r_{\text{ring}}$ gives very good results. In order to be on the safe side, the number used in the hybrid program is $4.0 \cdot k_0 \cdot r_{\text{ring}}$.

The dependency on the selection of the effective permittivity is given in Figure 3.8. It can be seen that this choice is not critical, i.e. the good results are obtained in a wide interval of possible values (the good results are obtained for $\epsilon_{\text{eff}} = 1.1 - 1.8$). In order to give some general rule (i.e. the rule that would not depend on particular multilayer dielectric structure) we have plotted the transmission coefficient for the case when the FSS elements (rings in the considered case) are printed on a dielectric structure and for the case when the FSS elements are positioned in the free-space (Fig. 3.6). By comparing the resonant frequencies for these two cases (i.e. by comparing the frequencies for which the transmission coefficient reaches the minimum) we can conclude that $\epsilon_{\text{eff}} \approx 1.15$. In all further calculations we have used $\epsilon_{\text{eff}} = 1.2$.

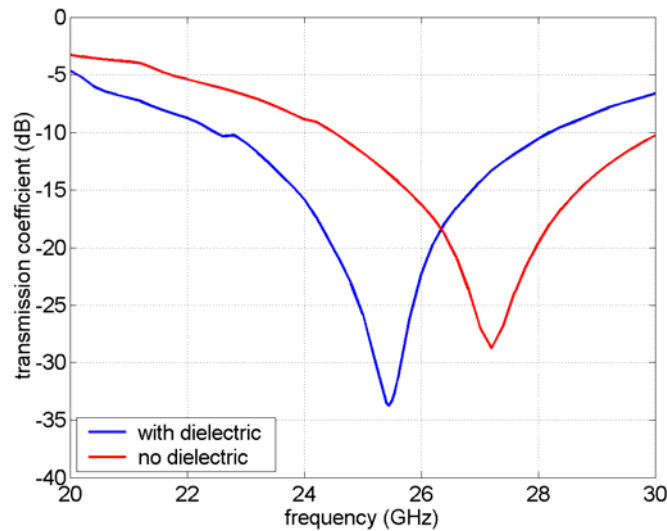


Figure 3.6. Comparison of transmission coefficient for the case when the FSS elements (rings in the considered case) are printed on a dielectric structure and for the case when the FSS elements are positioned in the free-space.

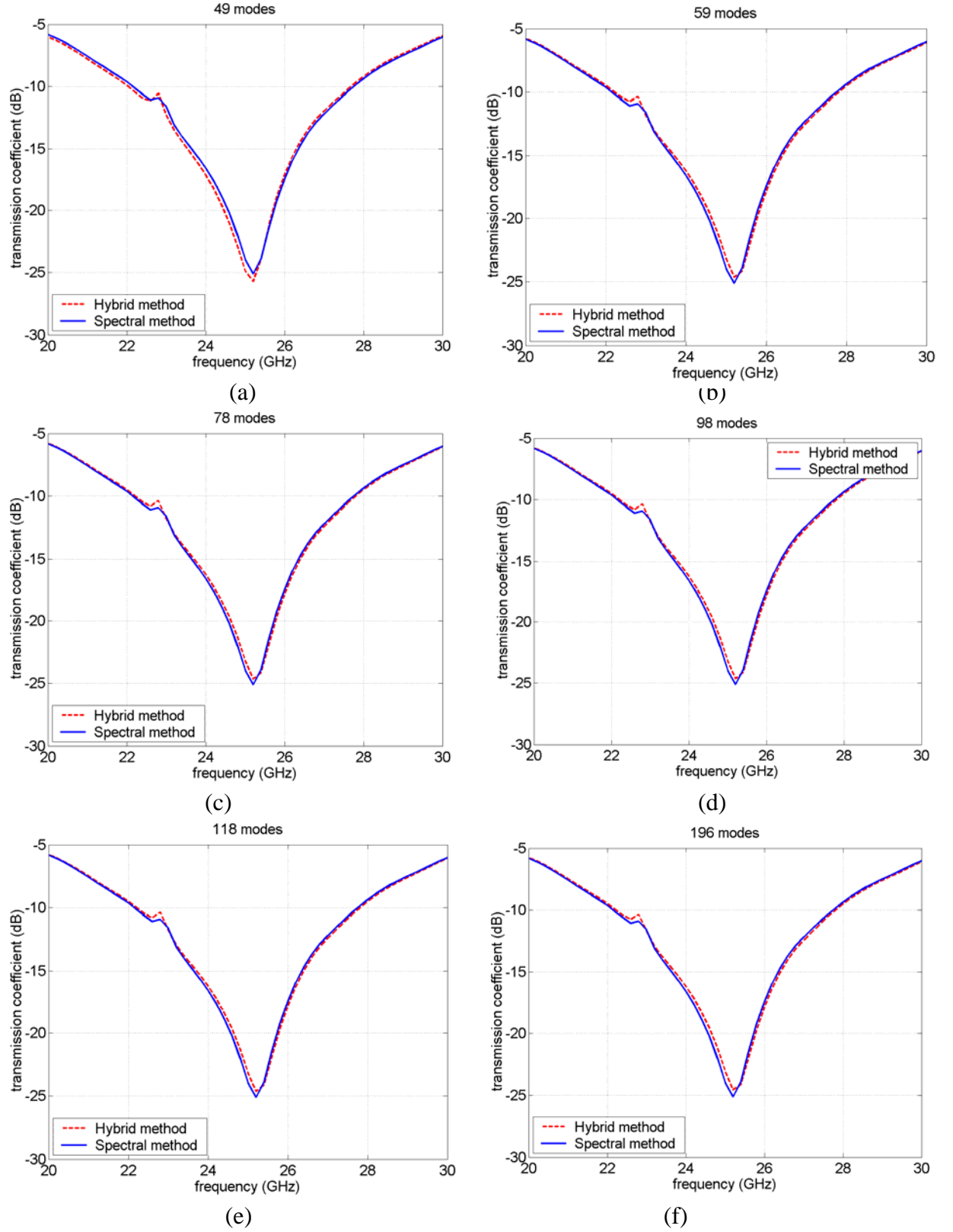


Figure 3.7. Accuracy of the hybrid model – dependence on the number of modes N_{\max} ; (a) $N_{\max} = 2.5 \cdot k_0 \cdot r_{\text{ring}}$, (b) $N_{\max} = 3.0 \cdot k_0 \cdot r_{\text{ring}}$, (c) $N_{\max} = 4.0 \cdot k_0 \cdot r_{\text{ring}}$, (d) $N_{\max} = 5.0 \cdot k_0 \cdot r_{\text{ring}}$, (e) $N_{\max} = 6.0 \cdot k_0 \cdot r_{\text{ring}}$, (f) $N_{\max} = 10.0 \cdot k_0 \cdot r_{\text{ring}}$.

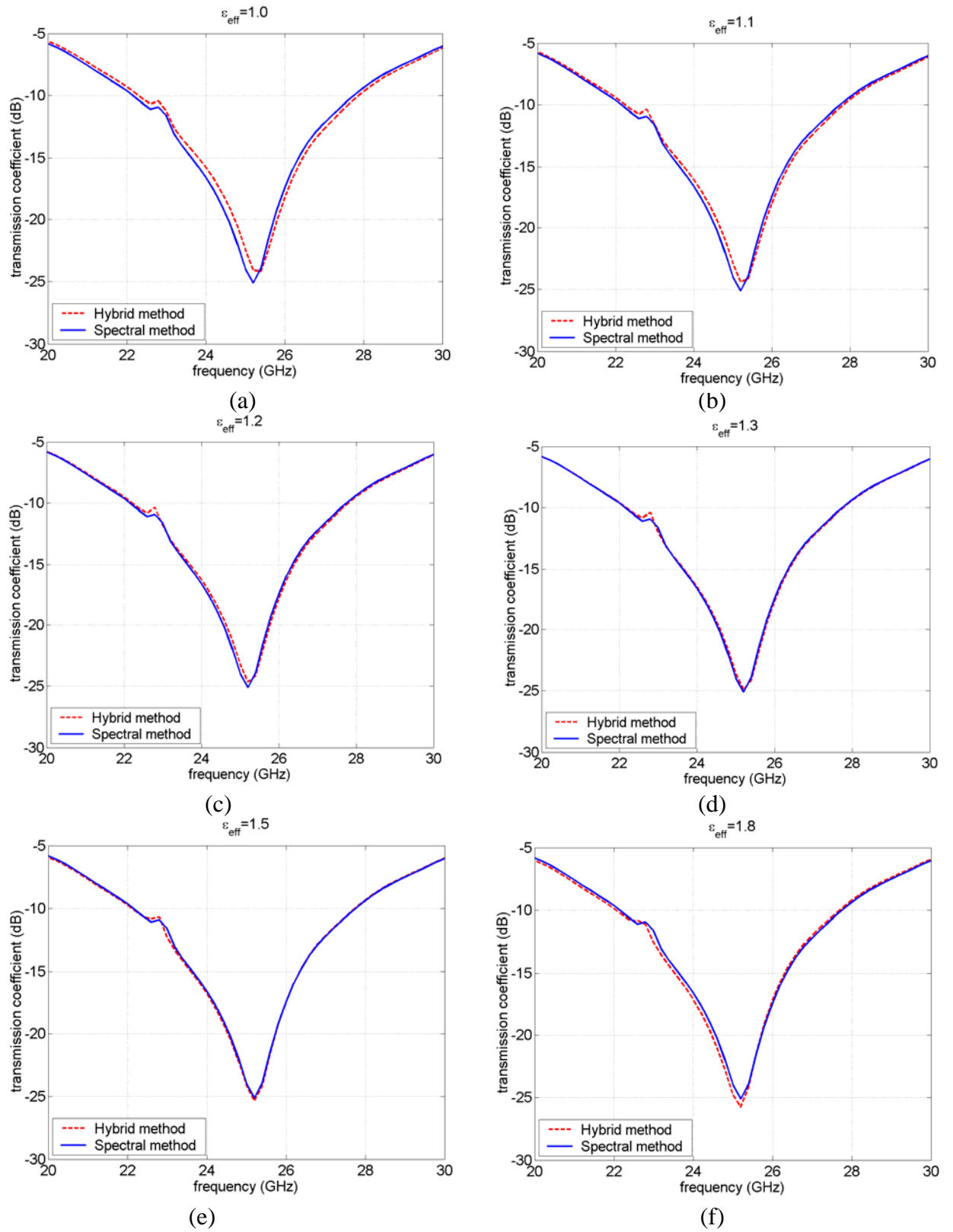


Figure 3.8. Accuracy of the hybrid model – dependence on selection of effective permittivity; (a) $\epsilon_{\text{eff}} = 1.0$, (b) $\epsilon_{\text{eff}} = 1.1$, (c) $\epsilon_{\text{eff}} = 1.2$, (d) $\epsilon_{\text{eff}} = 1.3$, (e) $\epsilon_{\text{eff}} = 1.5$, (f) $\epsilon_{\text{eff}} = 1.8$.

3.1.6 Subarray approach of analyzing curved FSS

Most of the curved FSS are not completely spherical structures. Therefore, it is important to develop an analysis method for curved FSS with general curvature. The main suggested principle is to divide the original array into a set of subarrays, where each subarray is locally approximated with spherical FSS (or cylindrical FSS if more appropriate, see Fig.3.9).

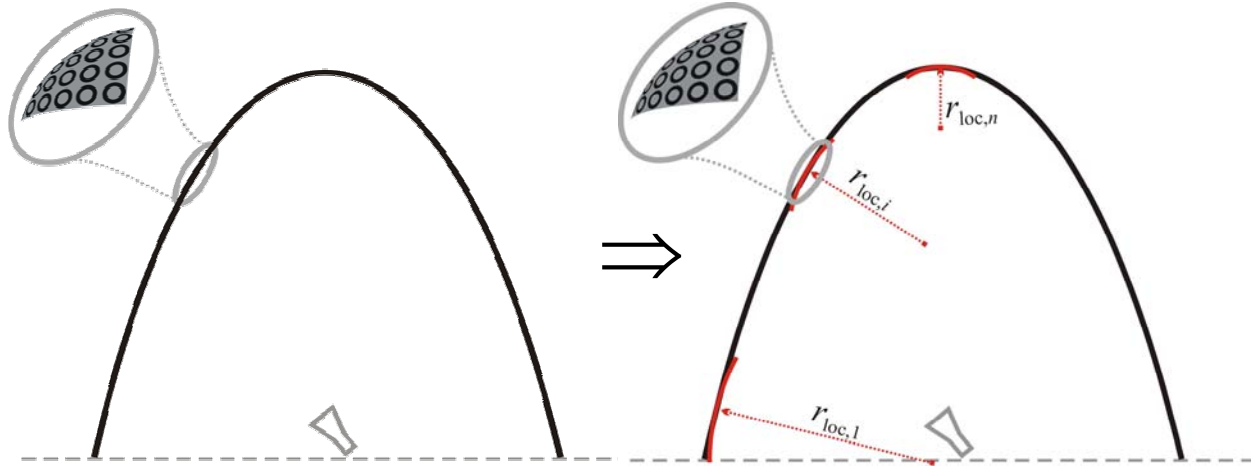


Figure 3.9. A doubly curved frequency selective radome with circular ring elements. Locally, the curved FSS can be approximated as a spherical FSS.

There are two principles of connecting the subproblems (i.e. the results of the subarray analysis) into a global solution. In both cases the inner elements of the subarray are surrounded with outside elements whose current distribution is determined in another subarray problem. By this we distinguish the currents in the inner part of the array, and the currents at the edge elements of each considered subarray. In other words, overlapping elements exist between neighboring subarrays.

Two approaches of connecting subarrays are:

1. The current distribution of the elements in the subarray is individually determined, and therefore a large-scale problem is divided into subproblems of smaller size. In other words, instead of solving a large MoM matrix equation, one needs to solve a set of small-size MoM matrix equations.
2. The coupling MoM matrices of all subarray problems are connected into a global MoM matrix. In this approach, one needs to solve one large MoM linear system of equations. The MoM matrix is sparse since large-distance couplings are not taken into account due to subarray approach. Although this approach is more time consuming, it will be seen that it gives more accurate results since all couplings are globally connected (although large-distance couplings are not considered in this approach – they are approximated with zero value).

3.1.7 Calculation of radiation pattern of a FSS reflector system

There are two main applications of curved FSS – to use it as a subreflector in a reflector system, or to use it as a frequency selective radome. In both cases we are interested in the radiation pattern of a whole radiation system.

Let us consider first the reflector system. As an example, a single FSS reflector system is considered. The shape of the considered reflector is parabolic (although other shapes can be analyzed in the same way), and e.g. a horn antenna, placed in the focus of reflector, is selected as a primary feed. A sketch of the structure is given in Fig. 3.10.

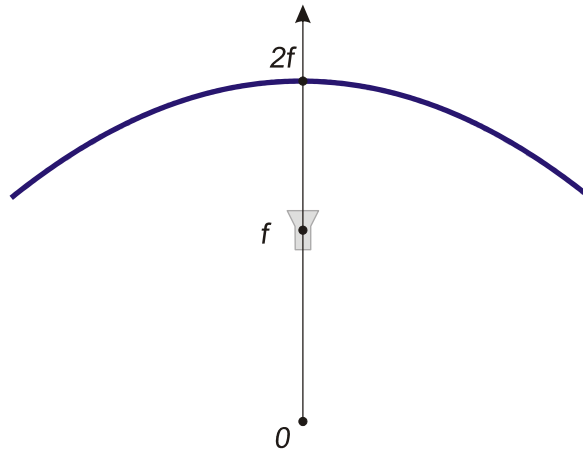


Figure 3.10. Reflector system consisting of a parabolic FSS reflector and a feeding antenna placed in the focus of reflector.

The radiation pattern of the horn antenna (or some other similar feeding antenna) with a linear polarization can be approximated as:

$$E_{feed}(r', \theta', \phi') = \frac{e^{-jk_0 r'}}{r'} E_0 \left[\hat{\theta}' (\cos \theta')^{\alpha_1} \cos \phi' - \hat{\phi}' (\cos \theta')^{\alpha_2} \sin \phi' \right] \quad (27)$$

The expression is written in local spherical coordinate system with the origin at the position of the phase center. It is important to explicitly put the dependence on distance R' in the expression for radiation pattern since the distance of some point at the reflector to the focus point (where the phase center of the horn antenna is positioned) varies a lot for different points at the reflector surface. In other words, this dependence on distance will make a natural tapering of the radiation pattern of the primary feed.

In order to find an optimum between tapering efficiency and spillover efficiency, it can be shown that the tapering of the radiation pattern at the edges of the reflector should be approximately – 10 dB lower compared to the apex value [17]. In more details, the field in the parabolic reflector aperture can be written as:

$$\mathbf{E}_{aperture}(\rho_{aperture}, \phi') = \hat{\mathbf{u}} E_0 \frac{F_{feed}(\theta', \phi')}{r_f} e^{-j2k_0 f}, \quad (28)$$

where the $F_{feed}(\theta', \phi')$ is the normalized radiation pattern of the feed antenna, r_f is the distance between the focal point and the point at the reflector where the considered ray is reflected, and $\hat{\mathbf{u}}$ is the unit vector describing the polarization of the feed antenna. Therefore, the factors α_1 and α_2 will be determined according to the requirement that the radiation pattern at the edges of the reflector should be approximately -10 dB lower compared to the apex value.

Small parabolic reflectors can be approximated with a spherical reflector. In that case the curvature of the equivalent spherical reflector is equal to twice the focal distance (i.e. $r_{ring} = 2 \cdot f_{reflector}$). The equation (27) in the global coordinate system (in which the origin corresponds to the center of the sphere) is equal (see Fig 3.11):

$$\begin{aligned} E_{feed}(R, \theta, \phi) &= \frac{e^{-jk_0 r'}}{r'} \left[\hat{\theta}(\cos \theta')^{\alpha_1} \cos \theta_{\Delta} \cos \phi - \hat{\phi}(\cos \theta')^{\alpha_2} \sin \phi - \hat{r}(\cos \theta')^{\alpha_1} \sin \theta_{\Delta} \cos \phi \right] \\ r'^2 &= r_{ring}^2 + \left(\frac{r_{ring}}{2} \right)^2 - 2r_{ring} \frac{r_{ring}}{2} \cos(\theta) = r_{ring}^2 (1.25 - \cos \theta) \\ \sin \theta_{\Delta} &= \sin \theta \frac{r_{ring}/2}{r'} \\ \theta' &= 180^\circ - (180^\circ - \theta - \theta_{\Delta}) = \theta + \theta_{\Delta} \end{aligned} \quad (29)$$

The voltage vector is calculated in the spectral domain:

$$V_j = \sum_{m=-\infty}^{\infty} \sum_{n=|m|}^{\infty} r_{ring}^2 \tilde{\mathbf{J}}_j^T(r_{ring}, n, -m) \tilde{\mathbf{E}}_{feed}(r_{ring}, n, m) \quad (30)$$

The E-field radiated by the primary feed in the spectral domain is calculated as (δ represents the Kronecker symbol):

$$\begin{aligned} \tilde{E}_{feed, \theta}(n, m) &= \frac{\pi}{\sqrt{2\pi S(n, m)}} \delta(|m| - 1) \cdot \\ &\left[\int_0^{\theta_{\max}} \frac{d\bar{P}_n^{|m|}(\cos \theta)}{d\theta} \sin \theta \cdot \frac{e^{-jkR'}}{R'} (\cos \theta')^{\alpha_1} \cos \theta_{\Delta} d\theta + \int_0^{\theta_{\max}} \bar{P}_n^{|m|}(\cos \theta) \cdot \frac{e^{-jkR'}}{R'} (\cos \theta')^{\alpha_2} d\theta \right] \end{aligned} \quad (31a)$$

$$\begin{aligned} \tilde{E}_{feed, \phi}(n, m) &= \frac{jm \cdot \pi}{\sqrt{2\pi S(n, m)}} \delta(|m| - 1) \cdot \\ &\left[\int_0^{\theta_{\max}} \bar{P}_n^{|m|}(\cos \theta) \cdot \frac{e^{-jkR'}}{R'} (\cos \theta')^{\alpha_1} \cos \theta_{\Delta} d\theta + \int_0^{\theta_{\max}} \frac{d\bar{P}_n^{|m|}(\cos \theta)}{d\theta} \sin \theta \cdot \frac{e^{-jkR'}}{R'} (\cos \theta')^{\alpha_2} d\theta \right] \end{aligned} \quad (31b)$$

In most practical cases the FSS elements (rings in our case) are not just standing in free-space without any supporting structure. In practice they are usually printed on thin dielectric slab. In order take into account this thin slab, we have determined the transmission coefficient in the spectral domain (since the voltage vector is calculated in the spectral domain). In more details, for each incoming spherical harmonic the outgoing spherical harmonic is calculated and the ratio between amplitudes of these two harmonics corresponds to the spectral transmission coefficient. The spherical harmonic representation is derived with the wave potential approach. The radial component of the magnetic vector potential in the spectral domain is equal:

$$\tilde{A}_r(r, n, m) = \begin{cases} 1 \cdot \hat{H}_n^{(2)}(k_0 r) + C_1 \cdot \hat{H}_n^{(1)}(k_0 r) & r < R_1 \\ C_2 \cdot \hat{H}_n^{(2)}(k_1 r) + C_3 \cdot \hat{H}_n^{(1)}(k_1 r) & R_1 \leq r < R_2 \\ C_4 \cdot \hat{H}_n^{(2)}(k_0 r) & r \geq R_2 \end{cases} \quad (32)$$

Here the part containing the Schelkunoff spherical Hankel functions of the second type represents the outgoing waves, and the part containing the Schelkunoff spherical Hankel functions of the first type represents the incoming waves. The four constants C_1 , C_2 , C_3 and C_4 are determined by fulfilling the boundary conditions. In this case these boundary conditions are that the spectral-domain θ -component of the electric field and the spectral-domain ϕ -component of the magnetic field are continuous at two boundaries (defined with radii R_1 and R_2). In order to calculate the amplitude of the outgoing spherical harmonic we need to solve the following system of linear equations (the continuity condition for \tilde{E}_θ and \tilde{H}_ϕ at the boundaries R_1 and R_2 , respectively):

$$\begin{aligned} -C_1 \cdot \frac{\eta_0}{jR_1} H_n^{(1)'}(k_0 R_1) + C_2 \cdot \frac{\eta_1}{jR_1} H_n^{(2)'}(k_1 R_1) + C_3 \cdot \frac{\eta_1}{jR_1} H_n^{(1)'}(k_1 R_1) &= \frac{\eta_0}{jR_1} H_n^{(2)'}(k_0 R_1) \\ -C_1 \cdot \frac{1}{R_1} H_n^{(1)}(k_0 R_1) + C_2 \cdot \frac{1}{R_1} H_n^{(2)}(k_1 R_1) + C_3 \cdot \frac{1}{R_1} H_n^{(1)}(k_1 R_1) &= \frac{1}{R_1} H_n^{(2)}(k_0 R_1) \\ C_2 \cdot \frac{\eta_1}{jR_2} H_n^{(2)'}(k_1 R_2) + C_3 \cdot \frac{\eta_1}{jR_2} H_n^{(1)'}(k_1 R_2) - C_4 \cdot \frac{\eta_0}{jR_2} H_n^{(2)'}(k_0 R_2) &= 0 \\ C_2 \cdot \frac{1}{R_2} H_n^{(2)}(k_1 R_2) + C_3 \cdot \frac{1}{R_2} H_n^{(1)}(k_1 R_2) - C_4 \cdot \frac{1}{R_2} H_n^{(2)}(k_0 R_2) &= 0 \end{aligned} \quad (33)$$

The transmission coefficient for the spherical harmonic containing θ -component of the electric field is defined as

$$T_{\tilde{E}_\theta} = C_4 \quad (34)$$

In analog way we can determine the transmission coefficient for the spherical harmonic containing ϕ -component of the electric field. In order to obtain the system of linear equations (defined by the continuity condition for \tilde{H}_θ and \tilde{E}_ϕ at the boundaries R_1 and R_2 , respectively) we can use the duality principle – we can easily obtain the needed 4 equations by the substitution

$$\begin{aligned}
\tilde{E}_\theta &\rightarrow \tilde{H}_\theta \\
\tilde{H}_\phi &\rightarrow -\tilde{E}_\phi \\
\eta &\rightarrow \frac{1}{\eta}
\end{aligned} \tag{35}$$

It is interesting to notice that the amplitude of transmission coefficient is drastically reduced (actually approaching zero) for higher-order spherical harmonics. The approximate number of mode for which the transmission coefficient is very small (less than 10^{-5}) is equal $\text{int}[k_0\sqrt{\epsilon_r}R_{ring}]$ (less than 10^{-12} for spherical harmonics larger than $\text{int}[k_0\sqrt{\epsilon_r}R_{ring}]+10$) ; which is connected with the division of spherical harmonics to radiated and non-radiated harmonics. This approximate expression is the same as the one given in [18] where this division to radiated and non-radiated harmonics is investigated. To be on safe side, we can conclude that all radiated harmonics are included in the first $\text{int}[k_0\sqrt{\epsilon_r}R_{ring}]+10$ spherical harmonics.

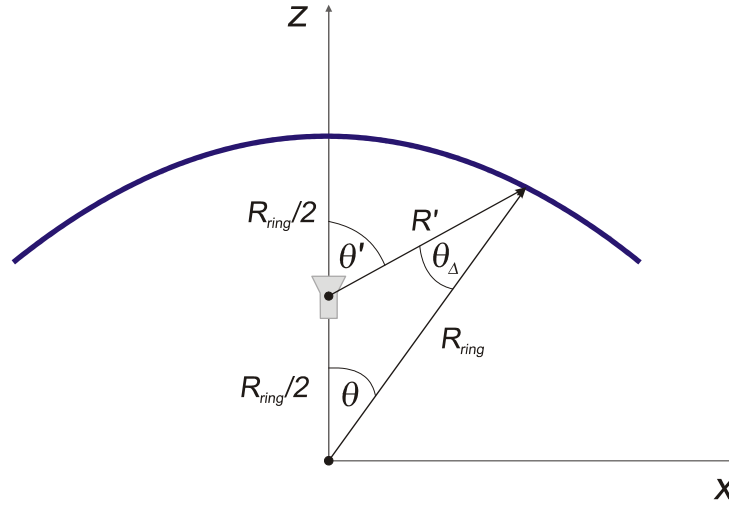


Figure 3.11. Connection between global and local coordinate system for a reflector system consisting of a spherical FSS reflector and a feeding antenna placed in the focus of reflector.

3.1.8 The analysis of dual structure – slots in the curved PEC surface

Similar procedure can be derived for the dual case scenario when the observed structure is a concave metal sheet with annular slots covered with dielectric layers. The analysis in this case has to be split into two parts, inner and outer problems, as shown in Fig. 3.12.

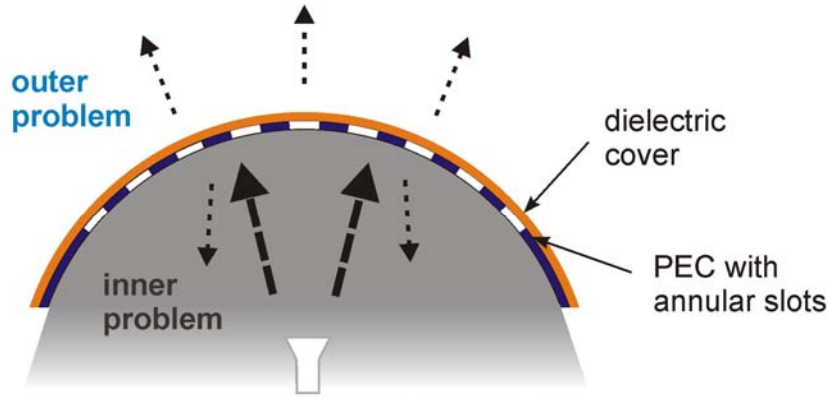


Figure 3.12. Sketch of the dual problem – curved FSS consisting of annular slots placed in the multilayer curved structure.

Using the equivalence theorem the two parts of the problem can be connected. The mutual admittance term in this case is:

$$Y_{ji} = - \sum_{m=-\infty}^{\infty} \sum_{n=|m|}^{\infty} r_{slot}^2 \tilde{\mathbf{M}}_j^T(r_{slot}, n, -m) \left(\tilde{\tilde{\mathbf{G}}}_{OUT}(n, m, r_{slot} | r_{slot}) + \tilde{\tilde{\mathbf{G}}}_{IN}(n, m, r_{slot} | r_{slot}) \right) \tilde{\mathbf{M}}_i(r_{slot}, n, m) \quad (36)$$

Again as in the ring type FSS case we can apply the asymptotic extraction, which results in;

$$\begin{aligned} Y_{ji} = & - \sum_{m=-\infty}^{\infty} \sum_{n=|m|}^{\infty} r_{slot}^2 \tilde{\mathbf{M}}_j^T(r_{slot}, n, -m) \left\{ \left(\tilde{\tilde{\mathbf{G}}}_{OUT}(n, m, r_{slot} | r_{slot}) + \tilde{\tilde{\mathbf{G}}}_{IN}(n, m, r_{slot} | r_{slot}) \right) \right. \\ & \left. - \left(\tilde{\tilde{\mathbf{G}}}_{OUT,asym}(n, m, r_{slot} | r_{slot}) + \tilde{\tilde{\mathbf{G}}}_{IN,asym}(n, m, r_{slot} | r_{slot}) \right) \right\} \tilde{\mathbf{M}}_i(r_{slot}, n, m) \\ & - \sum_{m=-\infty}^{\infty} \sum_{n=|m|}^{\infty} r_{pt}^2 \tilde{\mathbf{M}}_j^T(r_{slot}, n, -m) \left(\tilde{\tilde{\mathbf{G}}}_{OUT,asym}(n, m, r_{slot} | r_{slot}) + \tilde{\tilde{\mathbf{G}}}_{IN,asym}(n, m, r_{slot} | r_{slot}) \right) \tilde{\mathbf{M}}_i(r_{slot}, n, m) \end{aligned} \quad (37)$$

and similarly as before the extracted part can be evaluated in the spatial domain;

$$\begin{aligned}
Y_{ji} = & - \sum_{m=-\infty}^{\infty} \sum_{n=|m|}^{\infty} r_{slot}^2 \tilde{\mathbf{M}}_j^T(r_{slot}, n, -m) \left\{ \left(\tilde{\mathbf{G}}_{OUT}(n, m, r_{slot} | r_{slot}) + \tilde{\mathbf{G}}_{IN}(n, m, r_{slot} | r_{slot}) \right) \right. \\
& \left. - \left(\tilde{\mathbf{G}}_{OUT,asym}(n, m, r_{slot} | r_{slot}) + \tilde{\mathbf{G}}_{IN,asym}(n, m, r_{slot} | r_{slot}) \right) \right\} \tilde{\mathbf{M}}_i(r_{slot}, n, m) \\
& + \int_{\substack{test \\ function}} \int_{\substack{basis \\ function}} \mathbf{M}_j^T(r_{slot}, \theta, \phi) \left(\tilde{\mathbf{G}}_{OUT,asym}(\theta, \phi, r_{slot} | r_{slot}) + \tilde{\mathbf{G}}_{IN,asym}(\theta, \phi, r_{slot} | r_{slot}) \right) \mathbf{M}_i(r_{slot}, \theta, \phi) dS dS'
\end{aligned} \tag{38}$$

Considering the nature of the problem the free space Green's function is not a proper choice for the calculation of the extracted part. However, smooth canonical metallic structures can be very efficiently analyzed using Uniform Theory of Diffraction (UTD). The outer part is a typical UTD problem; apertures on a smooth PEC surface, and can be relatively easy implemented. The UTD formulation used for the computation of the outer asymptotic Green's function $\tilde{\mathbf{G}}_{OUT,asym}(\theta, \phi, r_{pt} | r_{pb})$ is a generalized formulation for arbitrary convex structures given by Pathak et al. [19] :

$$\begin{aligned}
\tilde{\mathbf{G}}_{OUT,asym}(Q | Q') = & -\frac{jk}{4\pi} \cdot \left[2Y_0 \left\{ \hat{b}' \hat{b} \left\{ \left(1 - \frac{j}{kt} \right) V(\xi) + D^2 \left(\frac{j}{kt} \right)^2 V(\xi) + T_0^2 \frac{j}{kt} [U(\xi) - V(\xi)] \right\} \right. \right. \\
& \left. \left. + \hat{t}' \hat{t} \left\{ D^2 \frac{j}{kt} V(\xi) + \frac{j}{kt} U(\xi) - 2 \left(\frac{j}{kt} \right)^2 V(\xi) \right\} + [\hat{t}' \hat{b} + \hat{b}' \hat{t}] \left\{ T_0 \frac{j}{kt} [U(\xi) - V(\xi)] \right\} \right\} \right] \cdot DG_0(kt)
\end{aligned} \tag{39}$$

Here ξ is a generalized Fock parameter, $U(\xi)$ and $V(\xi)$ are the corresponding soft and hard surface Fock integrals, D is the ray divergence factor and Q and Q' are coordinates of the source and observation points which have distance t (see [19] for details).

However, UTD can't be used straight away due to the existence of the dielectric cover on the PEC, so again there is a need to define some effective permittivity value which is to be used in the UTD calculation. It can be shown that the best choice is to use the value of the permittivity of the layer that is next to the PEC (see [20] for details), and in our case this simply means that the actual value of the permittivity of the dielectric cover should be used for the calculation of the asymptotic outer problem.

A bit more complex is the inner problem. A simple geometrical optics approach would be the first choice for a concave problem, however the circular holes in the PEC act as sources at the inner surface and generate multiple reflected ray fields that have caustics that lie near the boundary. Geometrical optics in such case is insufficient to give an accurate description of the surface fields and some additional methods have to be considered. Approach often used is the implementation of the whispering gallery modes into the analysis. Our inner problem can now be solved using a field solution that is comprised out of N geometrical optics rays and M whispering gallery modes [21]:

$$G_{IN,asym} \sim \sum_{n=0}^N G_n + \sum_{m=1}^M G_m - \frac{1}{2} G_N. \tag{40}$$

G_n here comes from the geometrical optics representation and is given by:

$$G_n \sim \frac{1}{\pi} (-j)^n \int_{Cn'} \exp[jka q_n(w)] dw, \quad (41)$$

where a is the sphere radius and $q_n(w)$ is defined as

$$q_n(w) = |\phi - \phi'| \sin w + 2(n+1) \left[\cos w - \left(\frac{\pi}{2} - w \right) \sin w \right]. \quad (42)$$

The second contribution is from the whispering gallery modes and it is defined as

$$G_m = \frac{j}{ka} e^{j\nu_m |\phi - \phi'|} J_{\nu_m}(ka) \left[\frac{\partial}{\partial \nu} J_{\nu}'(ka) \right]_{\nu_m}^{-1}. \quad (43)$$

Details of this calculation are given in [21].

3.1.9 Structure of the program

If one considers the expressions needed to be calculated when implementing the spectral-domain moment method (equation (4)), one can notice that several parts depend only on geometry, i.e. they do not depend on frequency. For example, the vector-Legendre transforms of basis and test functions depend only on angular dimensions. Furthermore, if one considers the expressions that are used inside the G1DMULT algorithm, it can be seen that all expressions depend only on the spectral variable n , i.e. they do not depend on the spectral variable m (the ϕ dependence is included in the matrix $\overline{\mathbf{L}}$, see eqs. (1a)-(1d)). Therefore, the needed computer time can be drastically reduced if one precalculates parts that do not depend on frequency. More precisely, the vector-Legendre transforms of basis and test functions and the needed Legendre functions are calculated only once at the beginning of the program, whereas the spectral-domain Green's functions are calculated only once per each frequency point outside the loop over m . The flow chart of the developed program is given in Figure.3.13.

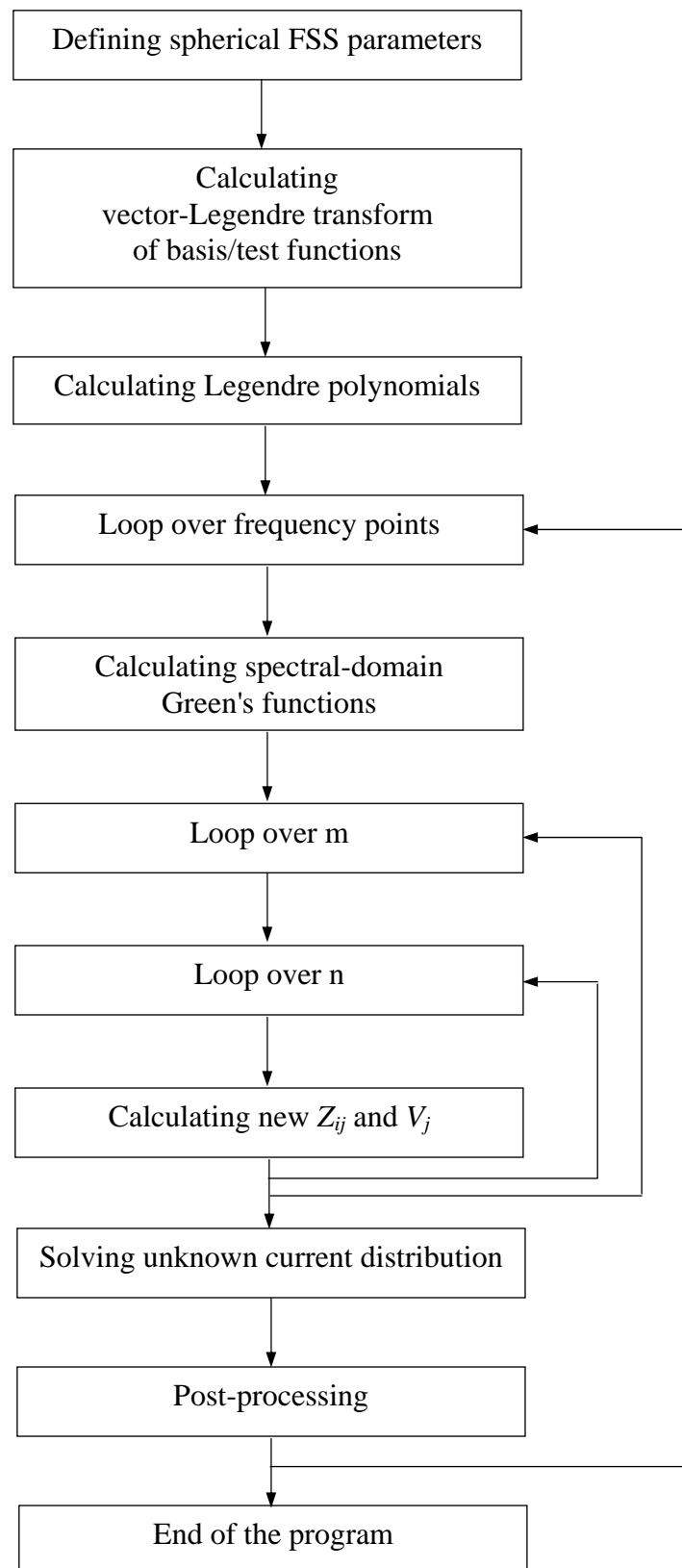


Figure 3.13. The flow chart of the program cFSS.

4 PROJECT OUTCOMES - RESULTS

4.1 Numerical results

4.1.1 Scattering properties of curved FSS

There are two types of considerations for curved FSS – when the excitation is an incident plane wave approaching the structure from the outside, and when the excitation is an antenna inside the radome. In this report first we will consider only the reflection and transmission properties of curved FSS when the excitation is a plane wave defined with

$$\mathbf{E}^{inc}(x, y, z) = \hat{\mathbf{x}} \mathbf{E}_0 e^{jkz} \quad (44)$$

As an example we have considered an array of circular rings of average radius 2.0 mm (i.e. to the center of the conductor; the conductor width was 0.4 mm), and separation between rings centers 4.9 mm. The rings are printed on a dielectric substrate of thickness 0.0075 mm and permittivity $\epsilon_r = 2.33$. The rings follow the triangular grid. The measured resonant frequency of the planar array is around 23 GHz [5]; see Fig. 4.2 (the dependence of the transmission coefficient on angle of incidence is given in Fig. 4.3). In spherical case, the two types of grids are considered: hexagonal grid and icosahedron grid (see Fig. 4.1).

First, we have analyzed a spherical array with the radius of curvature 18.7 mm, i.e. the θ - coordinates of rings are 0, 15, 30, 45 and 60 degrees (we have considered arrays up to 61 elements with the hexagonal grid and up to 51 elements with the icosahedral grid, as shown in Fig. 4.1). Such a relatively small radius of curvature (around $1.6 \lambda_0$ at the central wavelength) is selected to emphasize the difference between planar and conformal periodic structures.

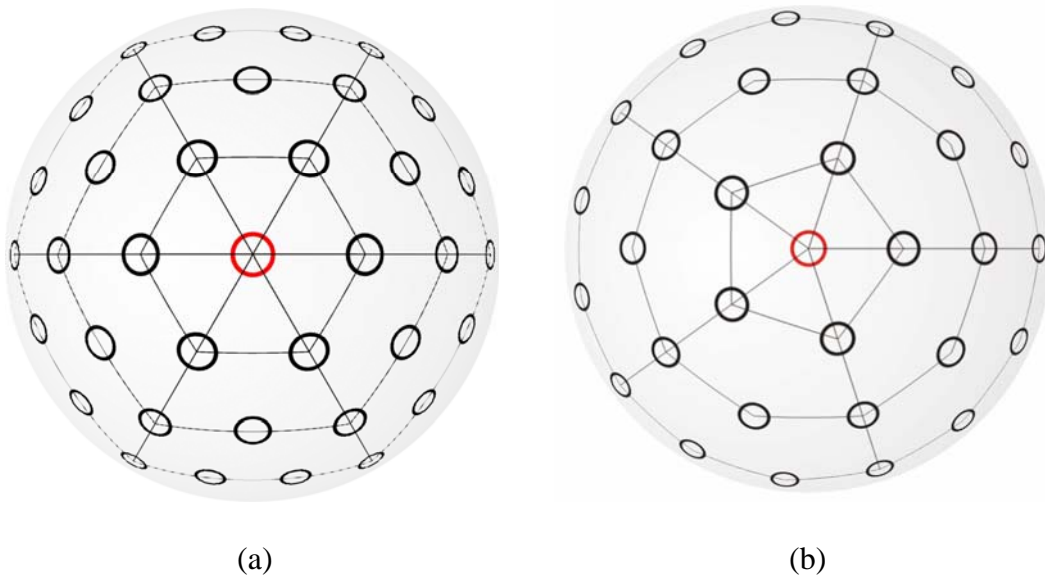
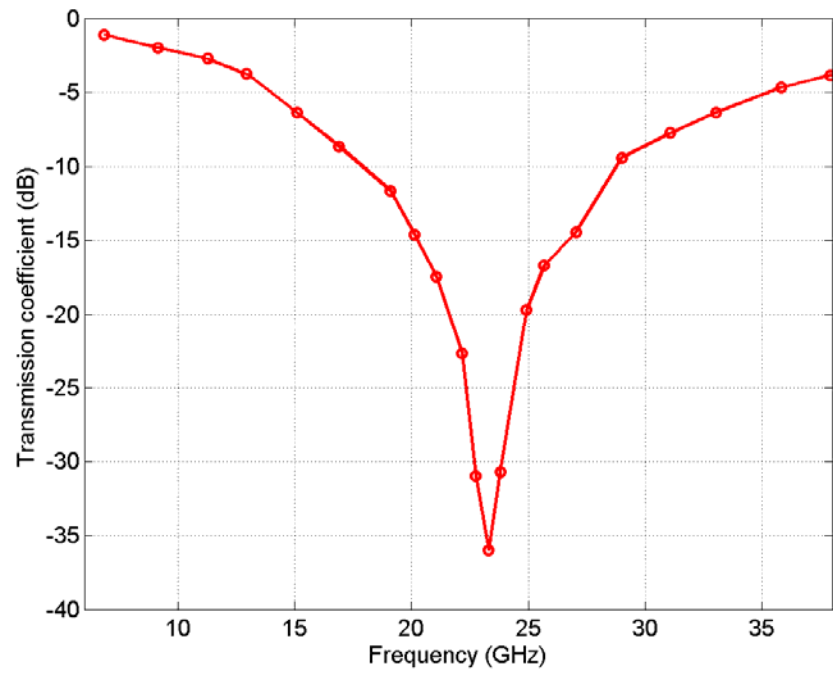
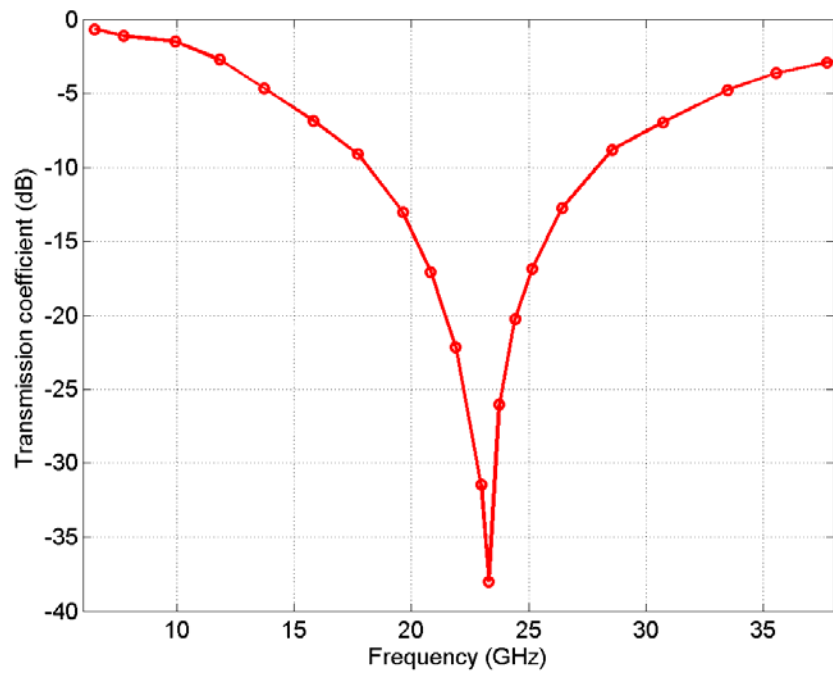


Figure 4.1. Geometry of the spherical FSS; (a) hexagonal structure, (b) icosahedral structure



(a)



(b)

Figure 4.2. Measured results of the transmission coefficient for the planar case – normal incidence (from [5]); (a) E plane, (b) H plane.

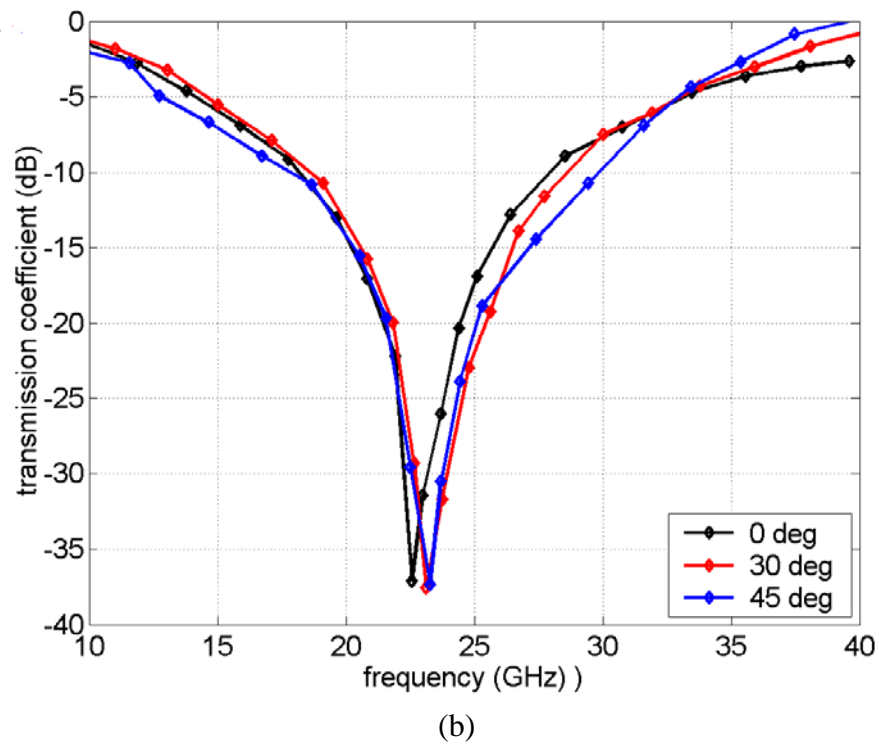
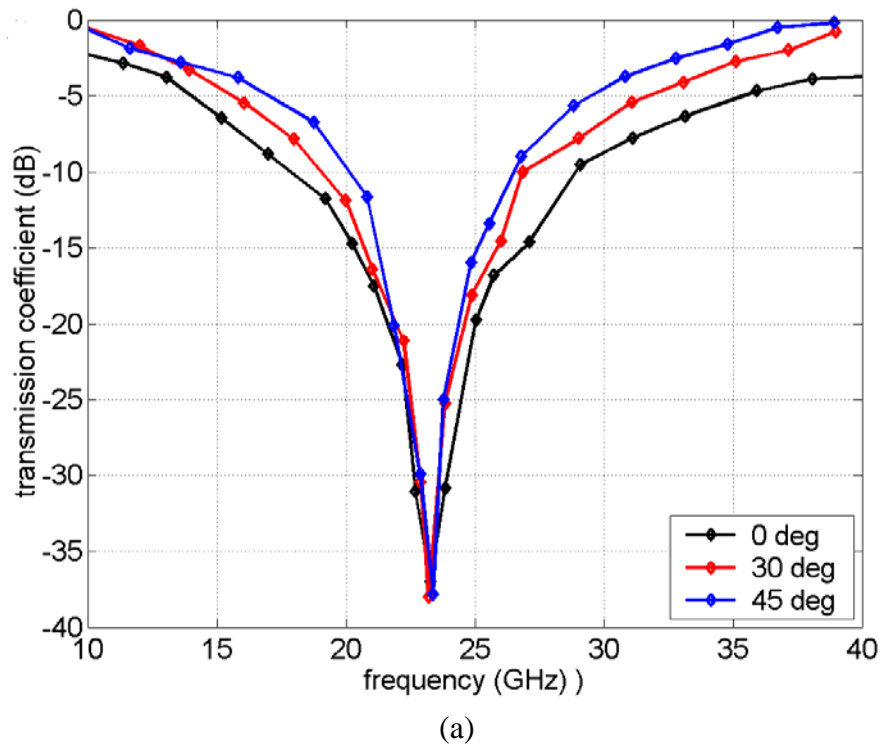
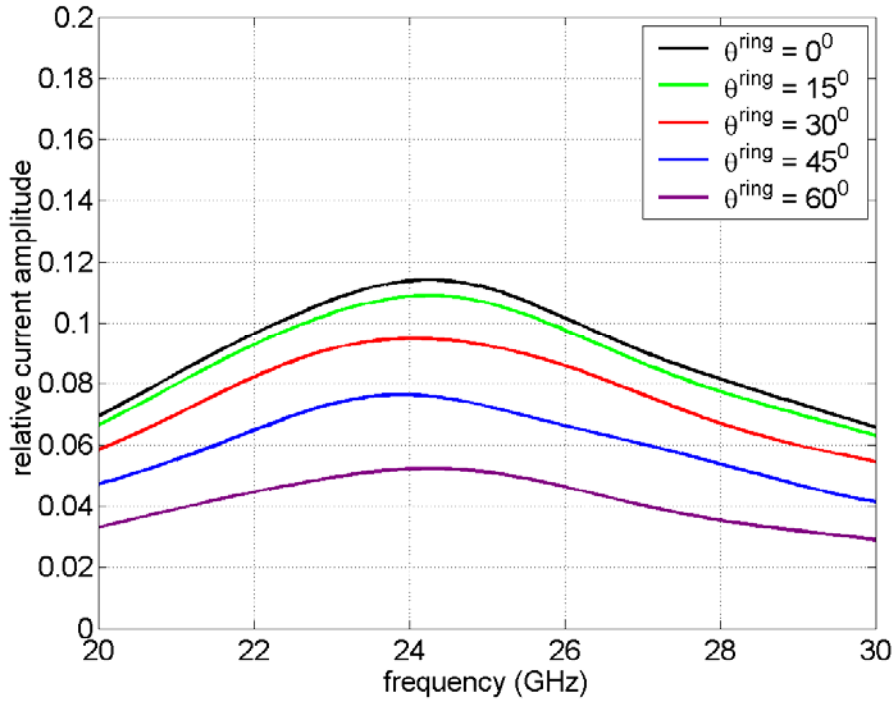


Figure 4.3. The dependency of the transmission coefficient on angle of incidence. The measured results of the planar FSS are shown (from [5]); (a) E plane, (b) H plane.

First we have calculated the influence of varying relative angle of incidence (defined as an angle with the surface normal vector), i.e. the input plane wave approaches the rings from a different angle of incidence, depending on the ring's position in the curved structure. For that purpose we have developed two versions of the program – one that rigorously includes the mutual coupling effect, and one where the mutual coupling is ignored (i.e. the moment method matrix has only self-coupling terms located around the matrix diagonal). In Fig. 4.4 we have shown how the induced current amplitude varies with the relative angle of incidence of the plane wave excitation (the considered rings have ϕ -coordinate $\phi^{ring} = 0^\circ$). It can be seen that the resonant frequency of the isolated ring stays almost constant (one of the reasons why the circular rings are selected for building curved FSS), and that only the amplitude changes due to the change of the angle of incidence (described with the factor $\cos\theta^{inc}$, see Fig. 4.4.a). The mutual coupling is not considered in Fig. 4.4.a. Once we take the mutual coupling into account the situation is quite different, as shown in Fig. 4.4.b and 4.4.c. Therefore, it is important to rigorously take into account mutual coupling effects.



(a)

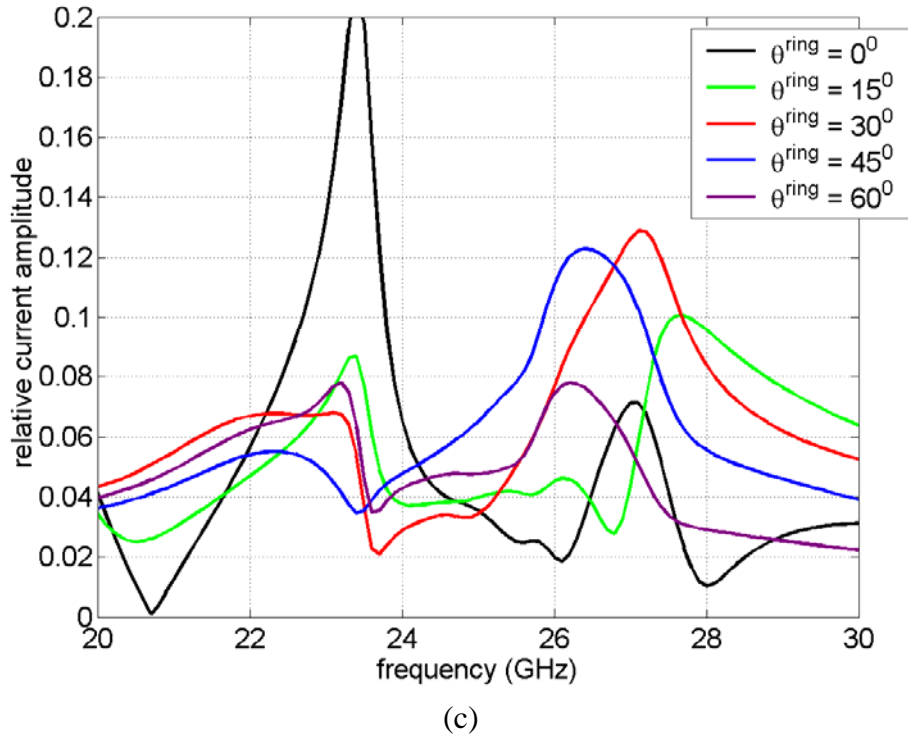
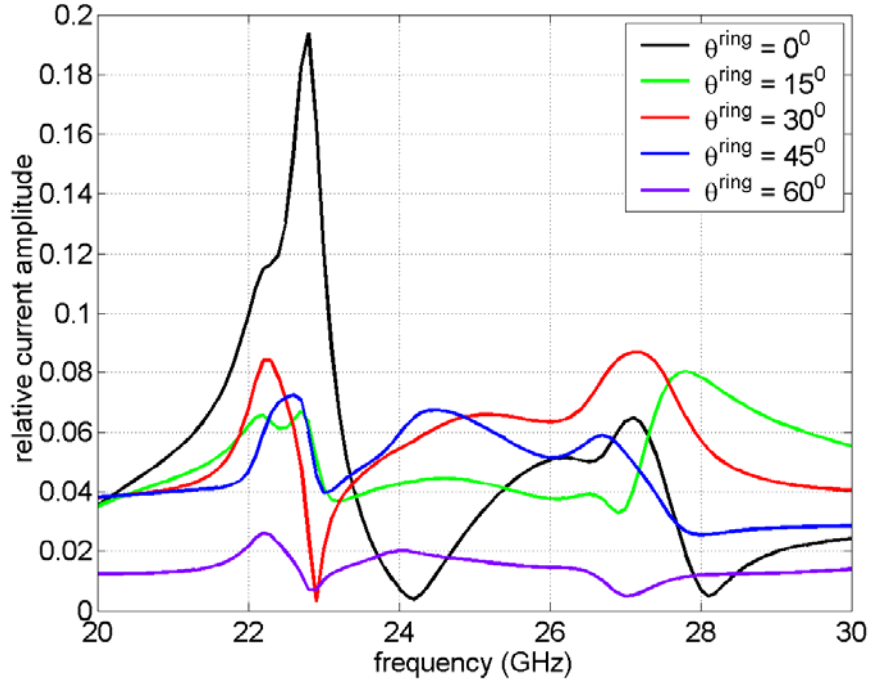
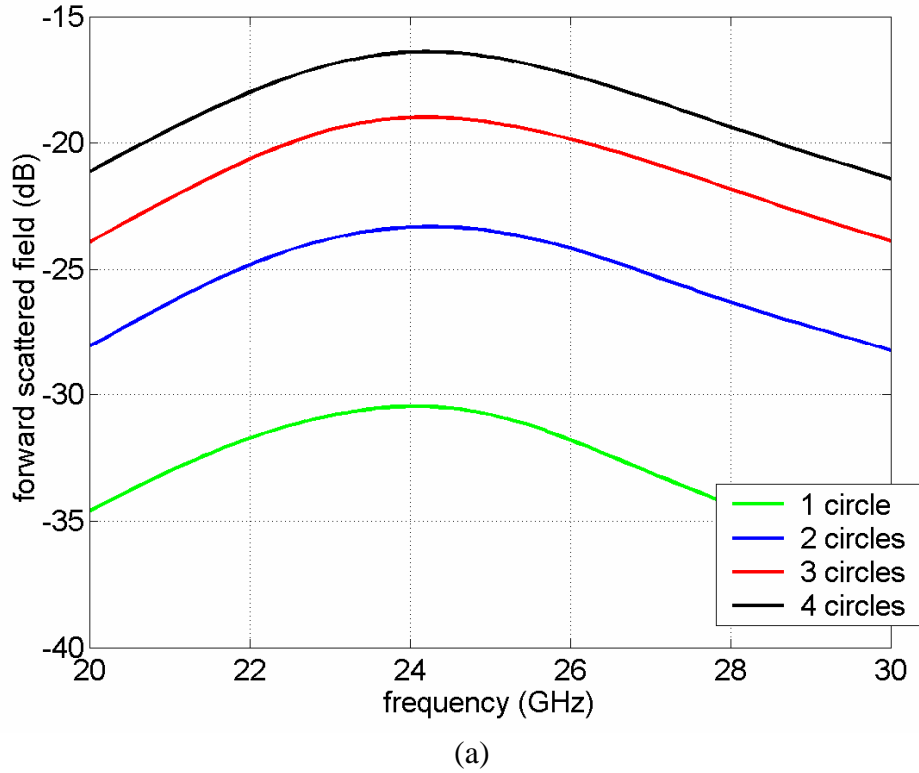
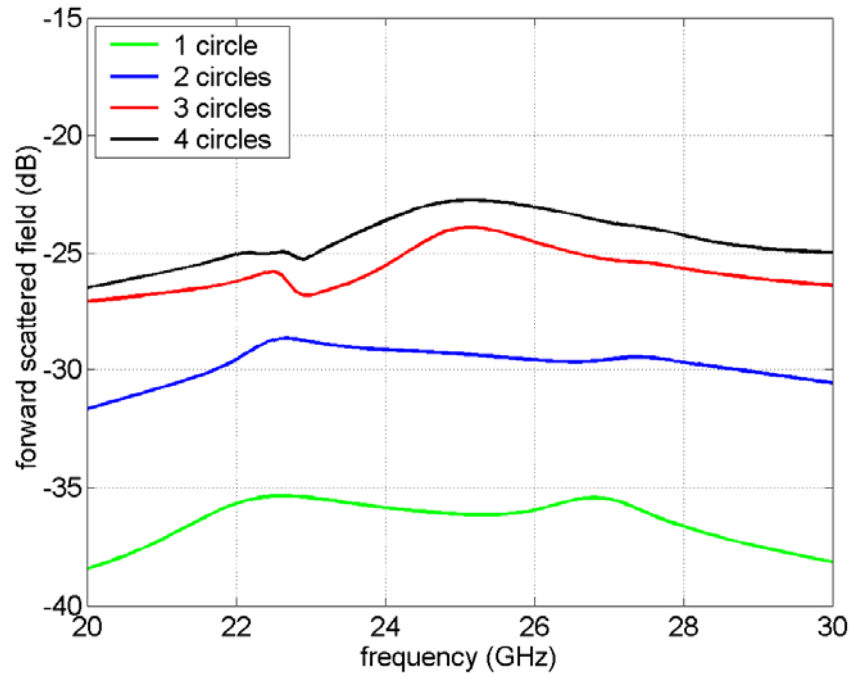


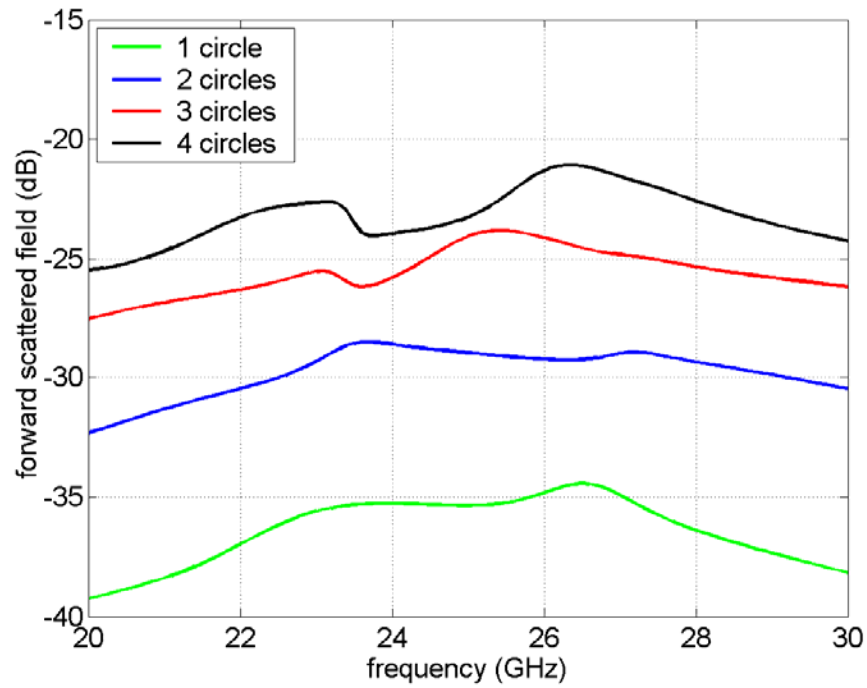
Figure 4.4. Variation of the current amplitude as a function of ring position (the ϕ -coordinate of the considered rings is $\phi^{ring} = 0^\circ$); (a) mutual coupling is not considered, (b) mutual coupling is rigorously considered; hexagonal structure, (c) mutual coupling is rigorously considered; icosahedral structure. The radius of the FSS structure is 18.7 mm, the FSS consists of 4 circles of elements around the central ring element.

Next, we have considered the variation of the forward scattered field as a function of the FSS size (Fig. 4.5.), i.e. as a function of the number of circles of ring elements around the central ring (placed at the pole) that define the spherical hexagonal or icosahedronal structure (see Fig.4.1.; in each hexagonal/icosahedronal circle the elements have the same θ -coordinate). The forward scattered field is a measure of a shadow that is produced by FSS, i.e. it corresponds to the $T - 1$ of the equivalent planar FSS, where T is the transmission coefficient. As in the previous case, we have considered two cases depending on whether or not the mutual coupling effects are considered. When the mutual coupling is taken into account the forward scattered field is not so regular anymore, and it has more than one local maximum.





(b)



(c)

Figure 4.5. Variation of the forward scattered field with the size of the array (number of circles of elements around the central element) in the spherical FSS structure (1 circle of elements correspond to the array of 7 elements, two circles of elements correspond to the array of 19 elements, etc.); (a) mutual coupling is not considered, (b) mutual coupling is rigorously considered; hexagonal structure, (c) mutual coupling is rigorously considered; icosahedronal structure.

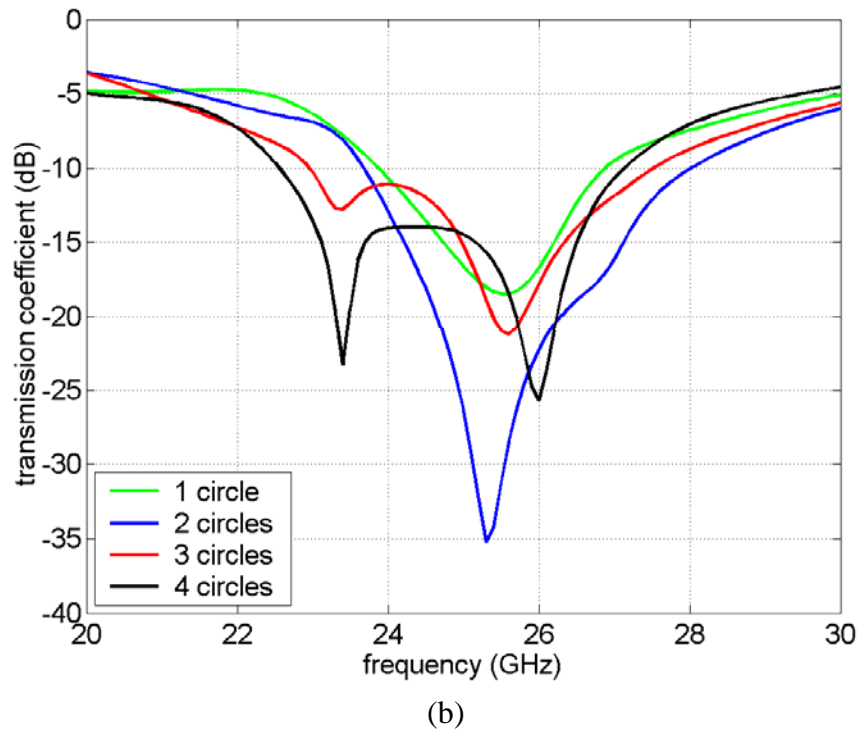
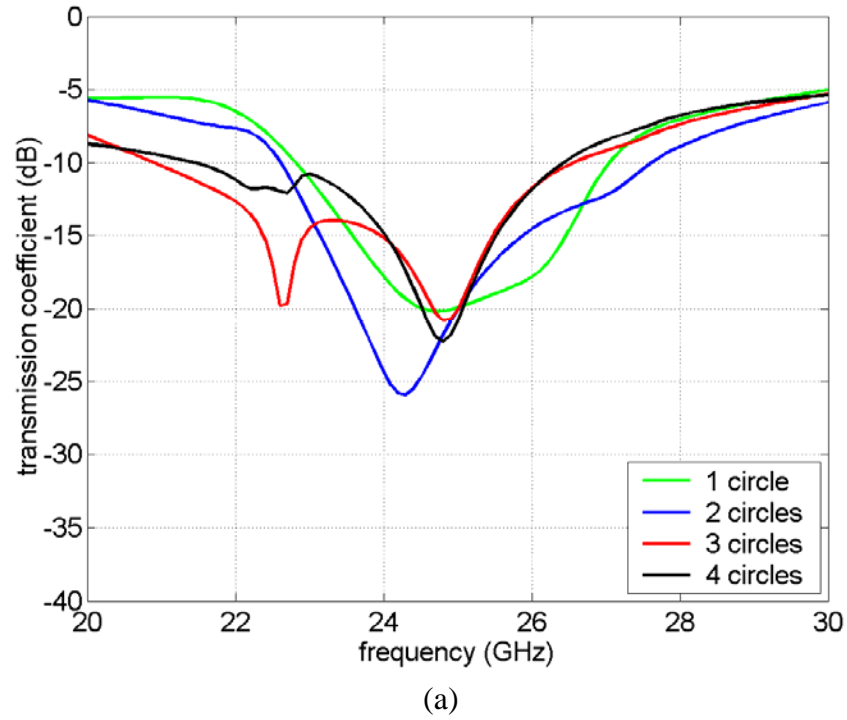


Figure 4.6. Transmission coefficient of the spherical FSS; (a) hexagonal structure, (b) icosahedronal structure. The angular distance between circles of elements in the considered FSS is 15° ; the angle of the cone with elements varies from the 15° (1 circle of elements around the central ring element) to 60° (4 circles of elements around the central ring element).

The transmission coefficient T for the curved FSS is defined as the ratio of the magnitude of the total E-field (incident and scattered) to the magnitude of the E-field due to the aperture field alone (i.e. in the absence of the array) $T = \left| \mathbf{E}^{scatt} + \mathbf{E}^{aperture} \right| / \left| \mathbf{E}^{aperture} \right|$ [14]. The incident field $\mathbf{E}^{aperture}$ in the upper expression is calculated as the far field at a distance z in the axial direction radiated by a circular aperture uniformly illuminated with a field of unit amplitude. In the case of the curved FSS printed on a dielectric, the influence of the dielectric slab is included in $\mathbf{E}^{aperture}$.

The transmission coefficient of the curved FSS from the previous example, following the hexagonal or the icosahedral grid, is shown in Fig. 4.6 (the angular distance between circles of elements is 15°). As in the previous example we have considered the dependency of the transmission coefficient on the FSS size – the angle of the cone with elements varies from 15° (1 circle of elements around the central ring element) to 60° (4 circles of elements around the central ring element).

It can be seen that the transmission coefficient for the curved FSS is quite non-regular (at least for small radii of curvature). Almost all the curves have two minimums. The question is can we approximate the analysis of curved FSS with the local planar approximation. In order to verify the local planar approach (i.e. the analysis approach where the currents at the FSS elements are determined by considering locally infinite planar array with average distance between elements) we have compared the results obtained with the rigorous method (without approximation on mutual coupling calculation) and with the local planar approach, see Fig. 4.7. It can be seen that it is not possible to use the local planar approximation, at least for curved FSS with small radius of curvature. The accuracy of the local planar approximation will be discussed in details later on.

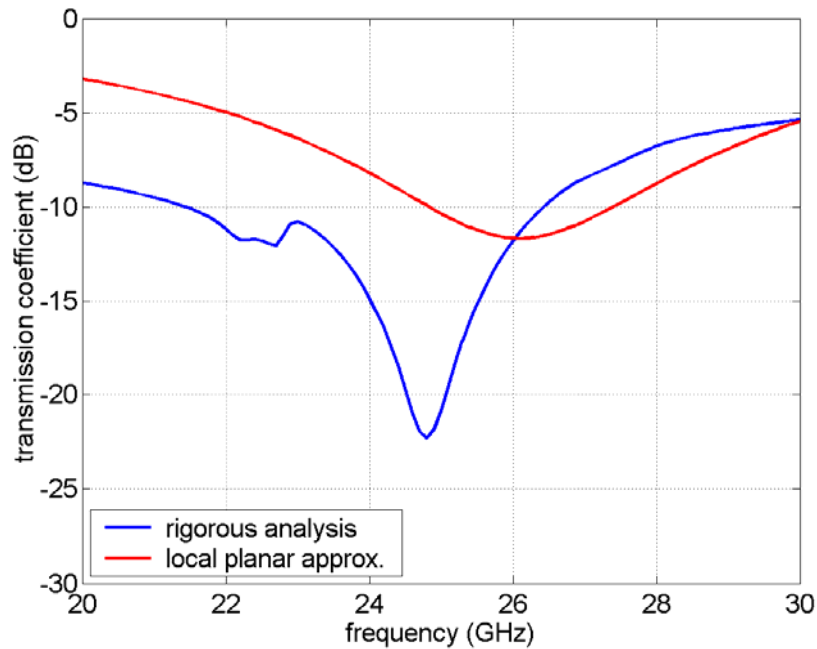


Figure 4.7. Transmission coefficient of the spherical FSS (hexagonal grid; 4 circles of elements around the central ring element) – comparison of the rigorous analysis approach and the analysis approach based on the local planar approximation.

The main reason why the transmission coefficient is so different compared to the transmission coefficient of the equivalent planar structure (Fig. 4.3) is that it is impossible to ensure the same distance between elements when considering double-curved periodic structure. For the considered spherical case (hexagonal or icosahedronal grid) the minimum and maximum distances d between the neighboring elements can be easily computed using the cosine law for spherical triangles [22]:

$$\cos d = \cos \theta_1 \cos \theta_1 + \sin \theta_1 \sin \theta_1 \cos(\phi_1 - \phi_2). \quad (45)$$

Table 1 gives the minimum and maximum distances d between the neighboring elements for ring elements belonging to different rows of the considered spherical FSS.

Circle number	normalized d_{\min}	normalized d_{\max}
0	1.0	1.0
1	0.99	1.23
2	0.99	1.28
3	0.94	1.45
4	0.87	1.45

(a)

Circle number	normalized d_{\min}	normalized d_{\max}
0	1.0	1.0
1	1.0	1.32
2	1.0	1.38
3	1.0	1.38
4	1.0	1.37

(b)

Table 1. The minimum and maximum distances d between the neighboring elements for ring elements belonging to different circles of elements of the considered spherical FSS; (a) hexagonal structure, (b) icosahedronal structure. The radius of the structure is 18.7 mm, i.e. the angular distance between the circles of elements of the hexagonal/ icosahedronal structure is 15° .

The influence of the element spacing on the resonant frequency is illustrated in Fig. 4.8 where the transmission coefficient of the equivalent planar FSS is plotted (planar FSS with triangular grid; FSS dimensions are the same as before). It can be seen that the resonant frequency is increased when the distance between the ring elements is enlarged. This explains why we have

two peaks in the transmission coefficient – different element distances cause different resonant frequencies.

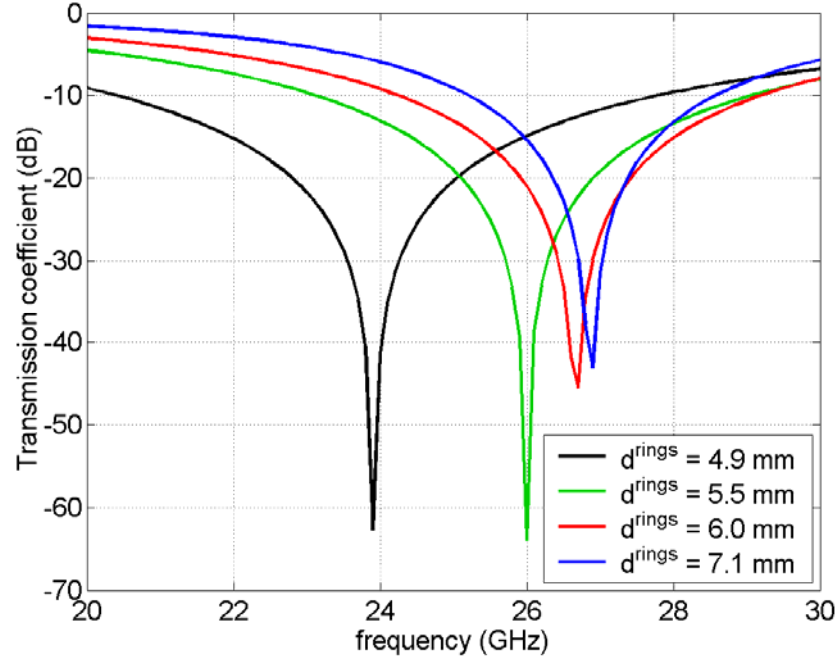


Figure 4.8. Transmission coefficient of the planar FSS as a function of the distance d^{rings} between the ring elements.

With enlarging the structure radius the angular distance between rows of elements is reduced. In other words, the angular distance between rows of elements of 7.5° , 5.0° and 3.75° corresponds to structure radius r_{ring} of 37.4 mm, 56.1 mm and 74.8 mm, respectively (the structure geometry is given in Fig. 3.1). The array “approaches” the planar case in which there is no variation in element spacing. That is illustrated in Table 2 where the FSS with four times larger radius is considered. Table 2 gives the minimum and maximum distances d between the neighboring elements for ring elements belonging to different rows of the spherical FSS with $r_{\text{ring}} = 74.8$ mm.

Circle number	normalized d_{min}	normalized d_{max}
0	1.0	1.0
1	1.0	1.24
2	1.0	1.31
3	1.0	1.34
4	1.0	1.36

(a)

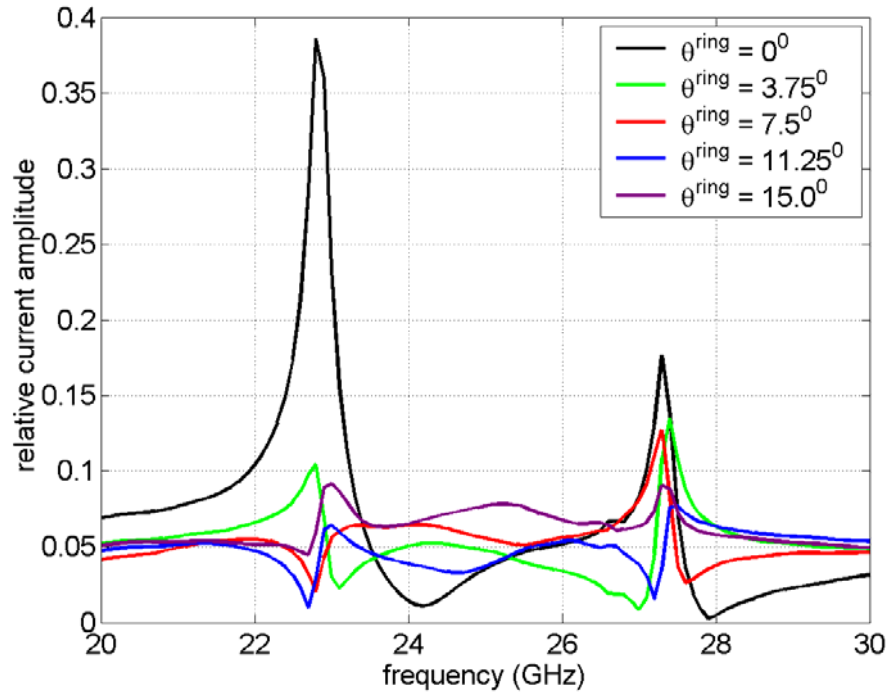
Circle number	normalized d_{\min}	normalized d_{\max}
0	1.0	1.0
1	1.0	1.33
2	1.0	1.42
3	1.0	1.42
4	1.0	1.30

(b)

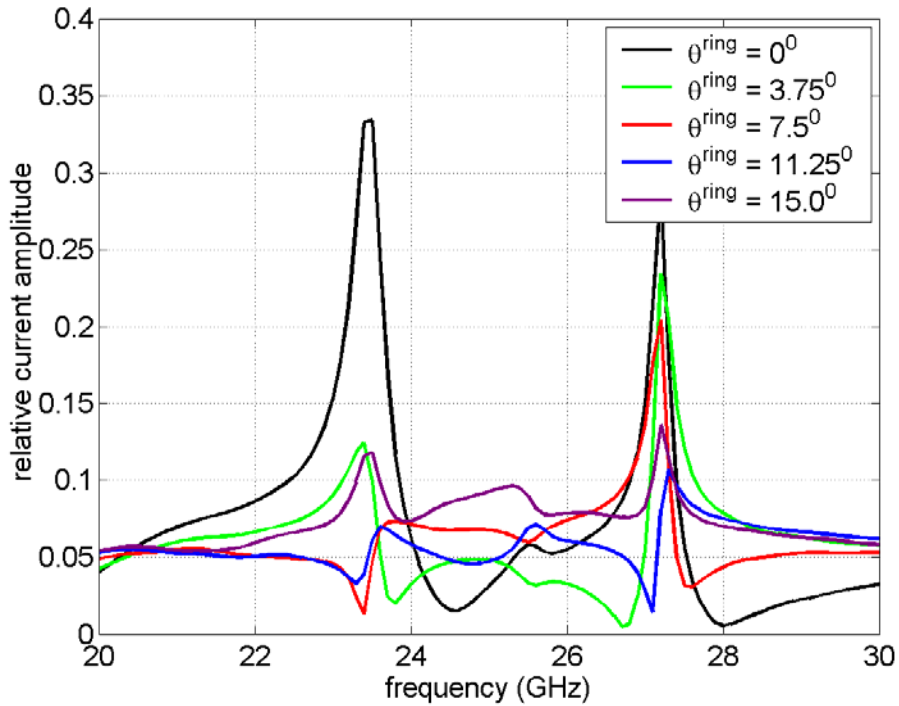
Table 2. The minimum and maximum distances d between the neighboring elements for ring elements belonging to different circles of elements of the considered spherical FSS; (a) hexagonal structure, (b) icosahedronal structure. The radius of the structure is 74.8 mm, i.e. the angular distance between the circles of elements of the hexagonal/ icosahedronal structure is 3.75° .

It is interesting to notice that the distances between FSS elements are more uniform only in the case of hexagonal grid, i.e. in the case of icosahedron grid the situation is even worse. The reason for that is that in the case of hexagonal grid we have started with the planar case and we have adapted the grid for spherical case. In the case of icosahedron grid we have started with a small sphere and we have adapted the grid for spheres with large radii.

The current distribution, the forward scattered field and the transmission coefficient for the spherical FSS with both hexagonal and icosahedron grid with $r_{\text{ring}} = 74.8$ mm is shown in Figs. 4.9 - 4.11. It can be seen that although the current distribution is still quite non-regular the scattered field and the transmission coefficient start to “behave” like in the planar case. In other words, due to “planar behavior of the structure”, there is only one minimum in the transmission coefficient curve, and the resonant frequency does not depend on the size of the FSS. Furthermore, since the distance between FSS elements is larger for icosahedron grid (see Table 2) the resonant frequency is higher for the FSS with icosahedron grid (see Fig. 4.8; the resonant frequency of the curved FSS with hexagonal/icosahedron grid is 25.4 GHz and 26.2 GHz, respectively).

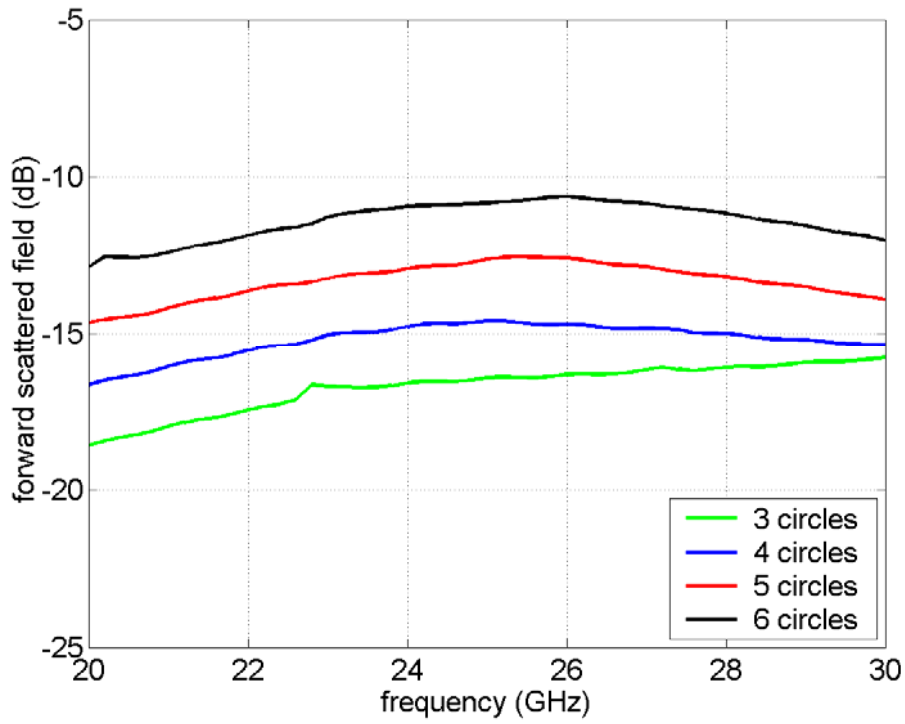


(a)

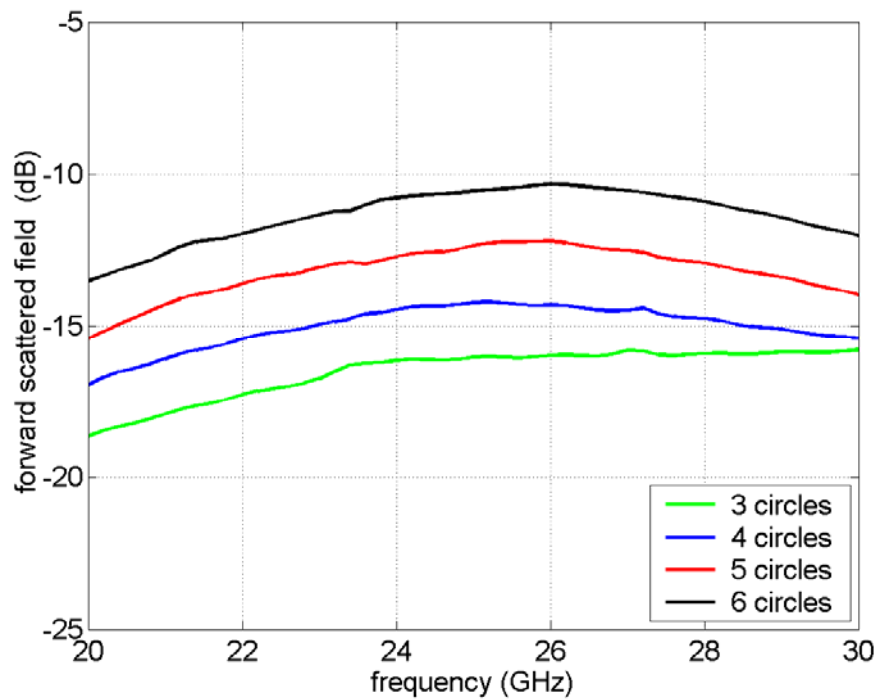


(b)

Figure 4.9. Variation of the current amplitude as a function of ring position (the ϕ -coordinate of the considered rings is $\phi^{ring} = 0^\circ$); (a) hexagonal structure, (b) icosahedral structure. The radius of the FSS structure is 74.8 mm, the FSS consists of 4 circles of elements around the central ring element.



(a)



(b)

Figure 4.10. Forward scattered field of the spherical FSS as a function of the FSS size, i.e. as a function of the number of circles of ring elements around the central ring; (a) hexagonal structure, (b) icosahedral structure. The angular distance between circles of elements in the considered FSS is 3.75° ($r_{\text{ring}} = 74.8$ mm).

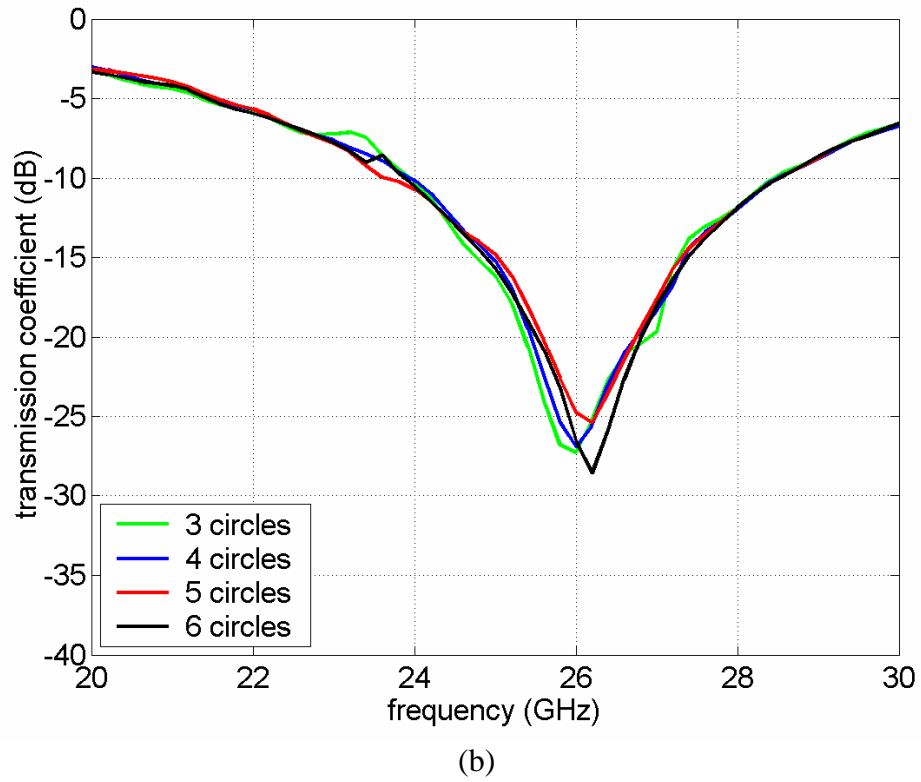
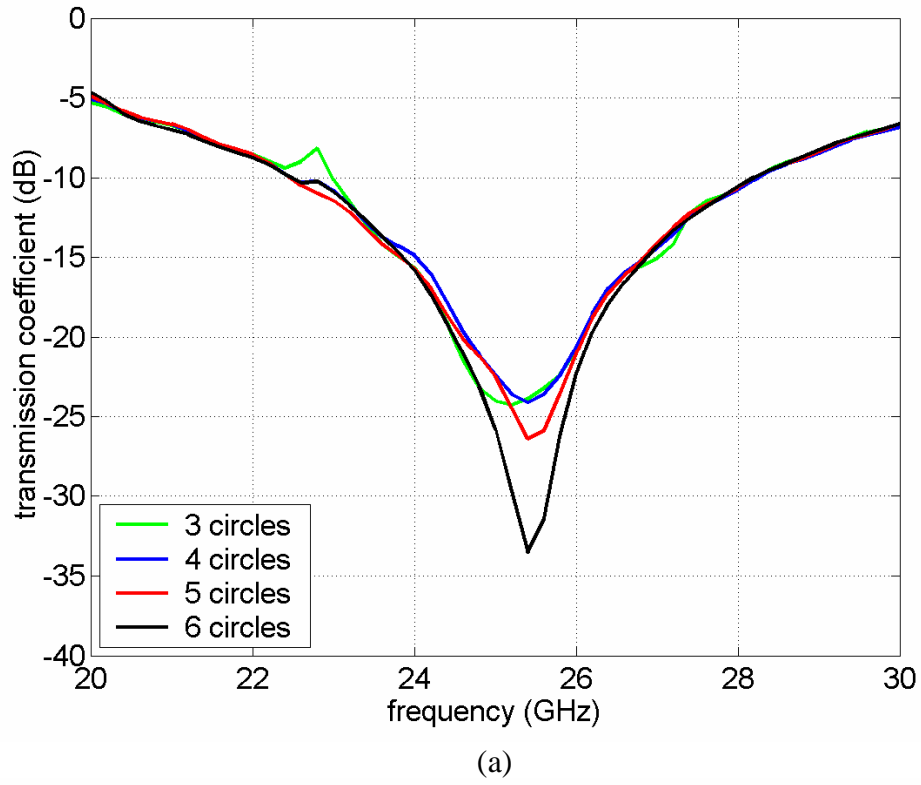


Figure 4.11. Transmission coefficient of the spherical FSS as a function of the FSS size, i.e. as a function of the number of circles of ring elements around the central ring; (a) hexagonal structure, (b) icosahedronal structure. The angular distance between circles of elements in the considered FSS is 3.75° ($r_{\text{ring}} = 74.8$ mm).

It is interesting to notice that the minimum/maximum distance mostly depends on the angular position of the FSS elements. In Table 3 the minimum/maximum distance is considered for the spherical FSS with radius $r_{\text{ring}} = 74.8$ mm. The considered elements have the same angular position (θ - coordinate) as the elements of the FSS with the 4 times smaller radius (i.e. as the elements considered in table 1). By comparing the tables 1 and 3 we can conclude that for the FSS with hexagonal grid the minimum/maximum distance depends mostly on angular position, while for the FSS with icosahedron grid the minimum/maximum distance depends also on size of the structure (still the dominant factor is the angular position of the FSS elements).

Circle number	normalized d_{\min}	normalized d_{\max}
0	1.0	1.0
4	1.0	1.36
8	1.0	1.37
12	0.94	1.45
16	0.87	1.43

(a)

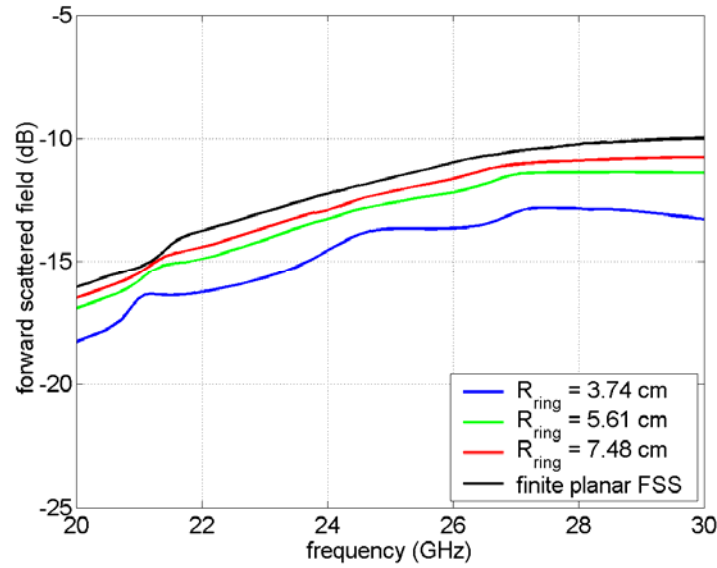
Circle number	normalized d_{\min}	normalized d_{\max}
0	1.0	1.0
4	1.0	1.30
8	1.0	1.40
12	1.0	1.41
16	1.0	1.43

(b)

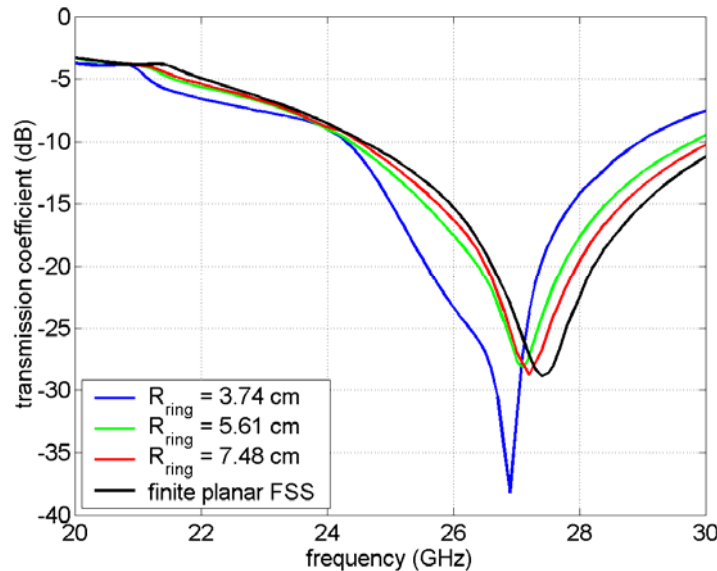
Table 3. The minimum and maximum distances d between the neighboring elements for ring elements belonging to different circles of elements of the considered spherical FSS; (a) hexagonal structure, (b) icosahedronal structure. The radius of the structure is 74.8 mm, i.e. the angular distance between the circles of elements of the hexagonal/ icosahedronal structure is 3.75° .

One of the important practical questions is how to determine the radius of the FSS for which the structure starts to behave as an equivalent planar FSS. In order to answer this question we have compared the transmission coefficient of the finite planar FSS with spherical FSS of different radius (the finite FSS is obtained by $r_{\text{ring}} \rightarrow \infty$). The permittivity of the dielectric supporting

structure is equal to 1.0 since our program for planar FSS can analyze only the finite FSS in homogeneous space. The curved FSS has hexagonal grid, and the structure radius is taken as parameter. The structure radius of 3.74 cm, 5.61 cm and 7.48 cm corresponds to the angular distance between circles of elements of 7.5° , 5.0° , and 3.75° , respectively. The dimensions of the rings are the same as before, and 6 circles of ring elements around the central element are present. As it can be seen in Fig. 4.12, with enlarging the structure radius the transmission coefficient (and the forward scattered field) approaches the transmission coefficient (forward scattered field) of the planar case. Furthermore, for structures larger than $r_{\text{ring}} = 56.1 \text{ mm}$ ($4.7 \lambda_0$ at the central frequency) there is practically no difference between planar and curved results (only a slight shift of the resonant frequency is present). Therefore, we can conclude that for structures with radius of curvature larger than $\sim 5\lambda_0$ one can use the local planar approximation.



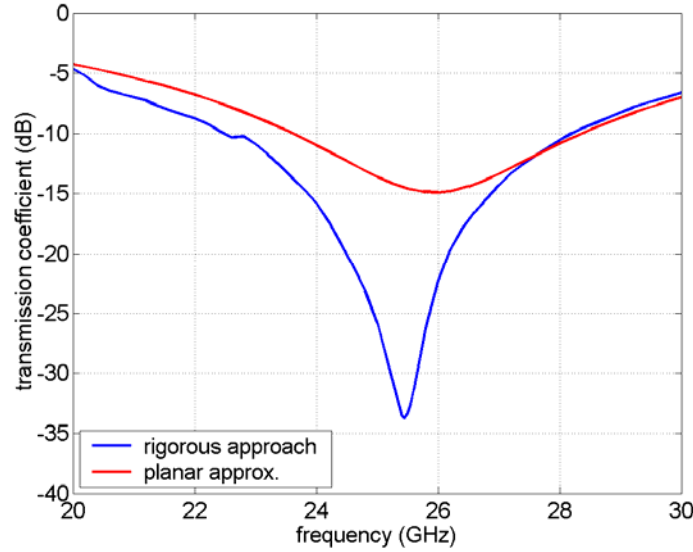
(a)



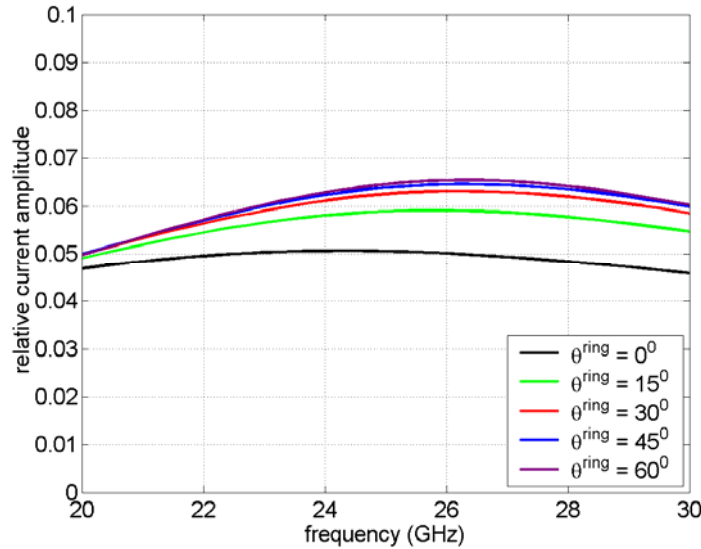
(b)

Figure 4.12. Dependency of the forward scattered field (a) and of the transmission coefficient (b) on the structure radius. The comparison with the results of the finite planar FSS is also given.

Another important practical question is can we use the local planar approximation when analyzing curved FSS. In other words, the current distribution at each FSS element is determined by considering the equivalent infinite planar FSS (i.e. planar FSS with the distance between elements that locally matches the curved FSS). In Fig. 4.13 the comparison of two analysis methods is given for the array with $r_{\text{ring}} = 74.8$ mm, $\epsilon_r = 2.33$ and the array consist of 6 circles around the central ring element. It can be seen that the local planar approximation cannot describe curved FSS properly (the difference between calculated transmission coefficients is too large). The reason for that is illustrated in Fig. 4.13.b – the current distribution is “too simple”, i.e. the included mutual coupling effects that correspond to infinite planar FSS are too simple for the considered complex structure (curved FSS with non-uniform element distribution).



(a)



(b)

Figure 4.13. Transmission coefficient (a) and current distribution (b) of spherical FSS with hexagonal grid ($r_{\text{ring}} = 74.8$ mm, 6 circles of elements around the central ring element are present). The results are obtained using the local planar approximation. The comparison with the transmission coefficient obtained using rigorous approach is also given.

4.1.2 Subarray approach of analyzing curved FSS

The proposed analysis method of a large curved FSS is based on subdividing the FSS into a set of subarrays, each with different local radius of curvature. In this way each subarray can be treated as a small spherical or cylindrical FSS. Therefore, by using the proposed approach, it is possible to analyze general curved FSS mounted on multilayer dielectric supporting structure.

There are two principles of connecting the results of each subproblem into the global solution:

1. The current distribution of the FSS elements in each subarray is individually determined. In this way a set of small MoM problems are solved instead of solving a large-scale MoM problem. The current distribution of the whole array is simply determined by mapping the each FSS element to the corresponding subarray problem, i.e. the current distribution at each FSS element is the same as the one determined by the corresponding subarray problem. The largest advantage of this approach is that we do not need to solve a huge linear system (usually with much more than 1000 unknowns).
2. Each FSS element is associated with the corresponding subarray problem. Furthermore, all these subproblems are connected into a global problem. In this approach we have to solve the huge linear system (corresponding to the superposition of all subproblems). However, we need to calculate mutual coupling terms only for the neighboring elements (therefore, saving a lot of CPU time).

Both approaches are tested by analyzing the spherical FSS with hexagonal grid containing 6 circles of elements around the central element (the FSS has totally 127 ring elements). Two cases are considered – when the structure radius is $r_{\text{ring}} = 37.4$ mm and $r_{\text{ring}} = 74.8$ mm, i.e. the angular distance between circles of elements is 7.5° and 3.75° , respectively. Fig. 4.14 gives results of both approaches when each subarray contains 3 circles of elements around the central FSS element. In the first approach, the inner part of each subarray consists of 7 elements (the inner parts directly determine the current distribution of the whole FSS; the edge effects are included in the outer part of each subarray). It can be seen that the first approach gives less accurate results. The reason for that probably lies in the nature of spherical FSS, i.e. in the complexity of mutual coupling effects present in curved FSS. In other words, it is not enough to locally consider mutual coupling effects (although strong coupling effects are present between nearby elements), but one must consider secondary coupling as well (ring a is coupled with ring b , ring b is coupled with ring c , ring c is coupled with ring d , etc.).

In Fig 4.15 we have investigated how many elements we need to include in each subarray in order to accurately predict the electromagnetic properties of the total FSS (the parameters of the large spherical FSS are the same like in the previous example). Only the results obtained using the second approach are shown here. It can be seen that good results are obtained using three circles of elements around each considered FSS element. However, one can also notice that there is always some discrepancy between the subarray and the rigorous approach. That also indicates the complexity of the mutual coupling effects in the curved FSS in which it is not possible to fulfill periodical symmetry (i.e. there is always some variation in the distance between different neighboring elements).

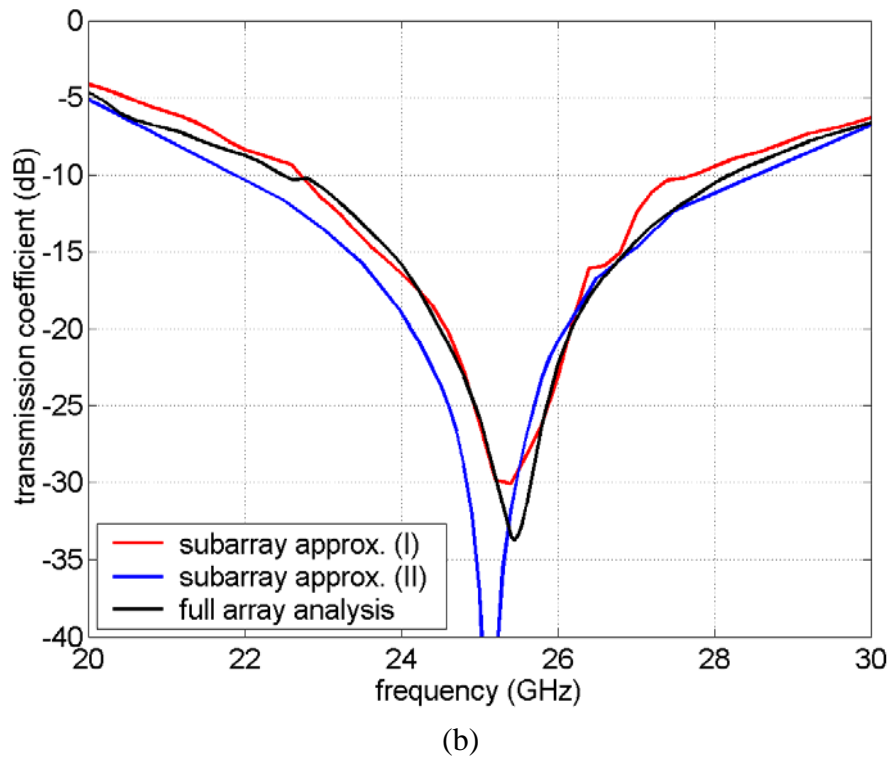
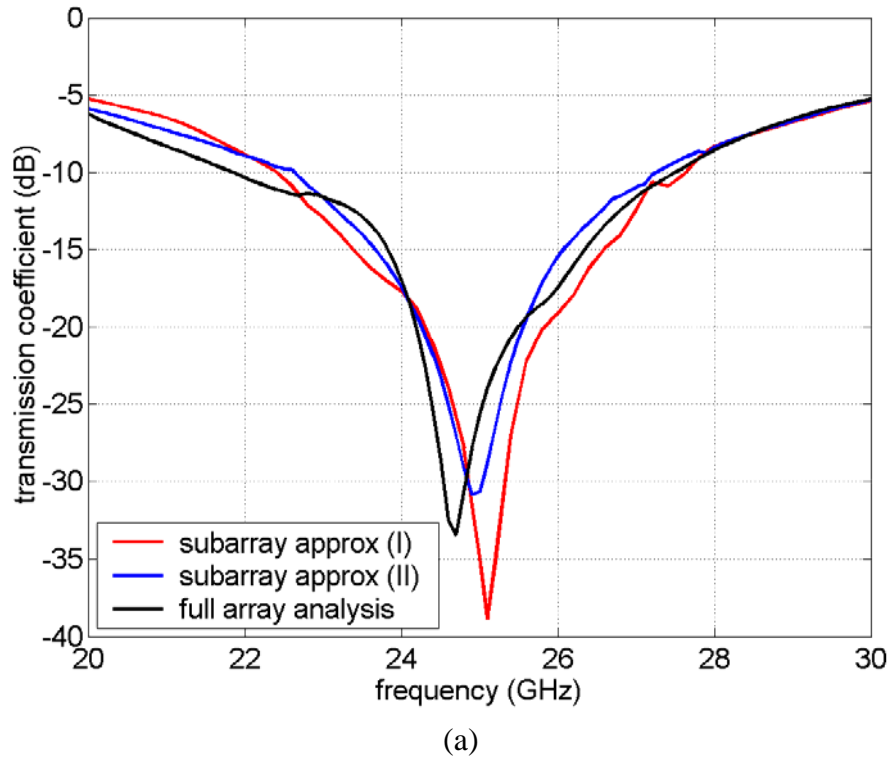
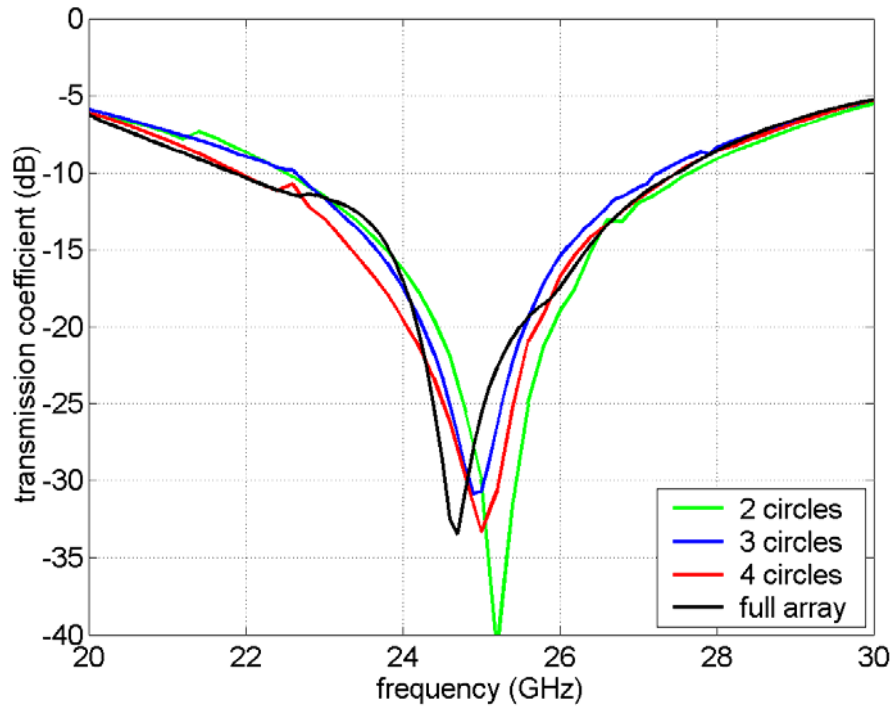
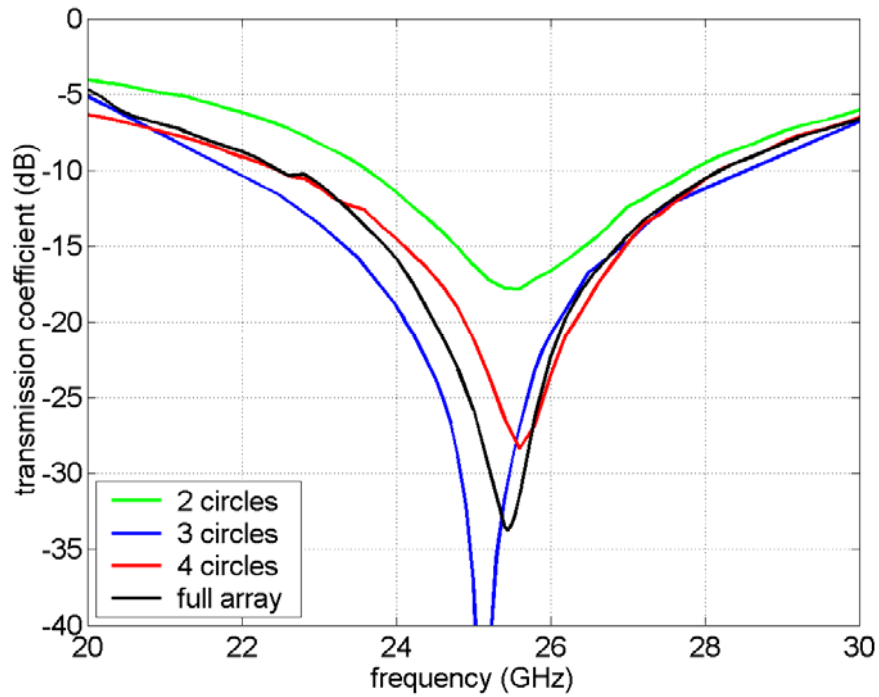


Figure 4.14. Transmission coefficient of a spherical FSS following the hexagonal grid with 6 circles of elements around the central element. (totally 127 elements are present). Transmission coefficient is calculated using the subarray approach where all the subproblems are connected into a global problem. (a) $r_{\text{ring}} = 37.4$ mm, (b) $r_{\text{ring}} = 74.8$ mm.



(a)



(b)

Figure 4.15. Transmission coefficient of a spherical FSS following the hexagonal grid with 6 circles of elements around the central element. (totally 127 elements are present). Transmission coefficient is calculated using two versions of the subarray approach and using the rigorous approach. (a) $r_{\text{ring}} = 37.4$ mm, (b) $r_{\text{ring}} = 74.8$ mm.

4.1.3 Radiation pattern of the FSS reflector system and of the FSS radome

In order to illustrate the possibility of using curved FSS for building frequency-selective reflector, we have considered a single FSS reflector system. The shape of the considered reflector is spherical, which is a good approximation of the parabolic reflector if the angular width is not too large. As a feed antenna we have considered a horn antenna placed in the focus of reflector (the distance between the apex of the reflector and the focal point is equal to half of the reflector radius, $f_{\text{reflector}} = r_{\text{ring}} / 2$). Sketch of the structure is given in Fig. 4.16.

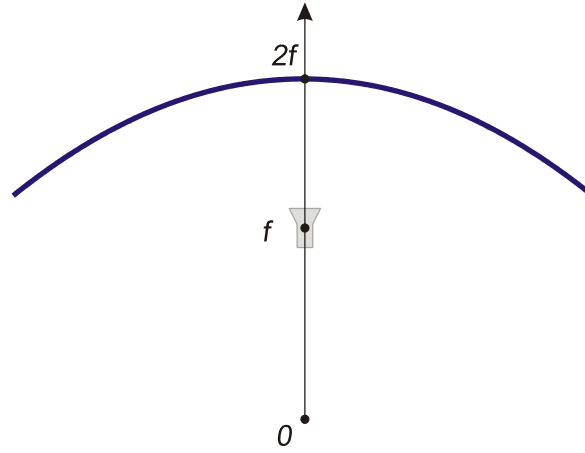


Figure 4.16. Reflector system consisting of a spherical FSS reflector and a feeding antenna placed in the focus of reflector.

The radiation pattern of the horn antenna (or some other similar feeding antenna) with a linear polarization can be approximated as:

$$E_{\text{feed}}(r', \theta', \phi') = \frac{e^{-jkr'}}{r'} \left[\hat{\theta}' (\cos \theta')^{\alpha_1} \cos \phi' - \hat{\phi}' (\cos \theta')^{\alpha_2} \sin \phi' \right] \quad (46)$$

The expression is written in local spherical coordinate system with the origin at the position of the phase center. It is important to explicitly put the dependence on distance r' in the expression for radiation pattern since the distance of some point at the reflector to the focus point (where the phase center of the horn antenna is positioned) varies a lot for different points at the reflector surface. In other words, this dependence on distance will make a natural tapering of the radiation pattern of the primary feed [17].

In order to find the optimum between tapering efficiency and spillover efficiency, it can be shown that the tapering of the radiation pattern at the edges of the reflector should be approximately -10 dB [17]. Therefore, the factors α_1 and α_2 will be determined according this requirement.

We have considered 3 examples of simple reflector system. The parameters of each considered structure are given in Table 4: radius of reflector r_{ring} , number of circles of elements around the central ring element (placed at the apex), angular size of the reflector, and factors α_1 and α_2 of the feeding horn. The working frequency in all considered cases was 25.4 GHz (frequency for

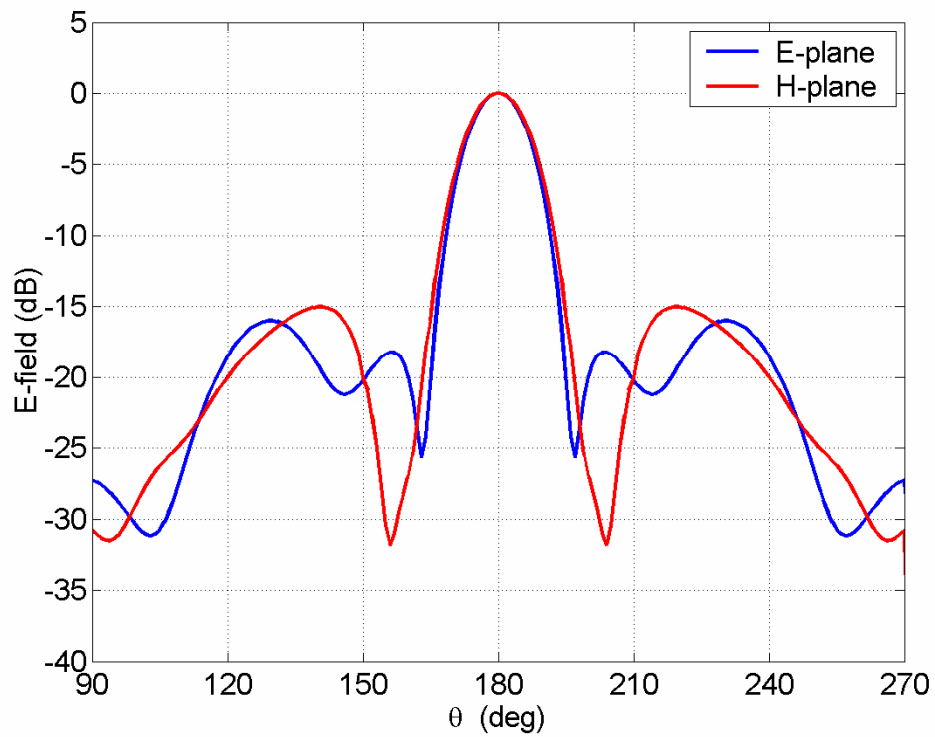
which the transmission coefficient of the curved FSS with radius $r_{\text{ring}} = 74.8$ mm has the minimum).

Reflector number	Reflector radius r_{ring} (mm)	Number of circles of FSS elements	Angular size of the array (from the origin)	Angular size of the array (from the focal point)	Factors α_1 and α_2
1	37.4	6	45°	73.7°	0.6017
2	74.8	6	22.5°	42.1°	3.4167
3	74.8	8	30°	53.8°	1.7793

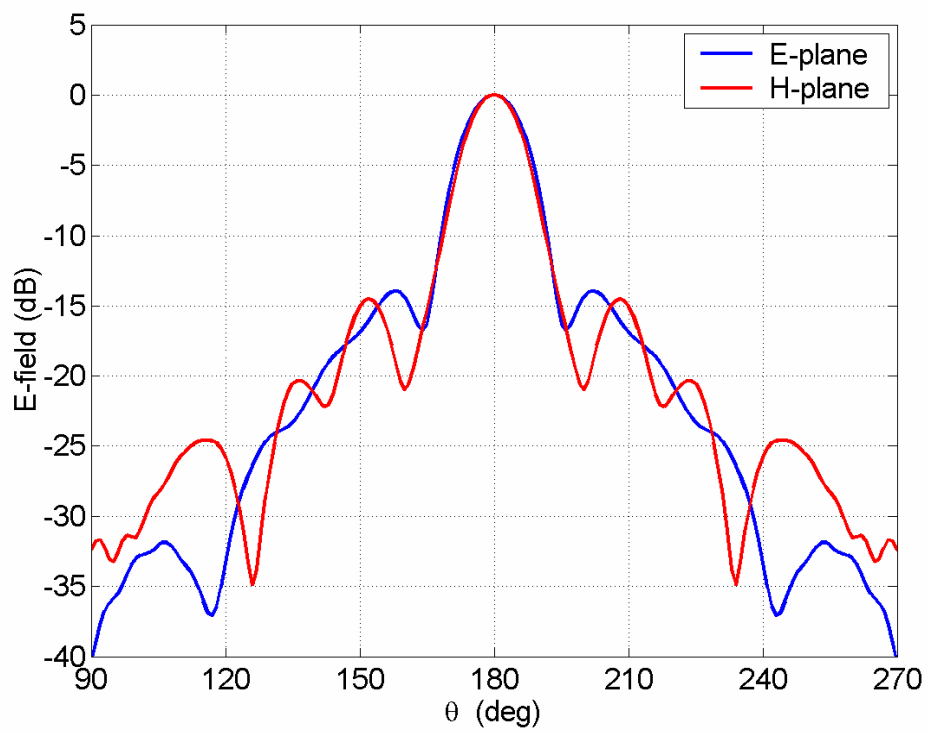
Table 4. The parameters of the considered reflector systems.

The radiation pattern of the reflector system is given in Figure 4.17. It can be seen that with enlarging the size of the FSS (mostly determined with the number of circles of FSS elements around the central ring element placed at the apex) the beamwidth is getting narrower and, consequently, the directivity is getting larger.

The frequency dependency of the radiation pattern is illustrated in Fig. 4.18. We have considered the first case, i.e. the radius of the structure is $r_{\text{ring}} = 37.4$ mm and the curved FSS consisting out of 6 circles of elements around the central FSS element. It can be seen that with enlarging the working frequency the beamwidth is getting narrower. Furthermore, the FSS is not completely reflective at frequencies $f = 20$ GHz and $f = 30$ GHz resulting in the loss of the directivity



(a)



(b)

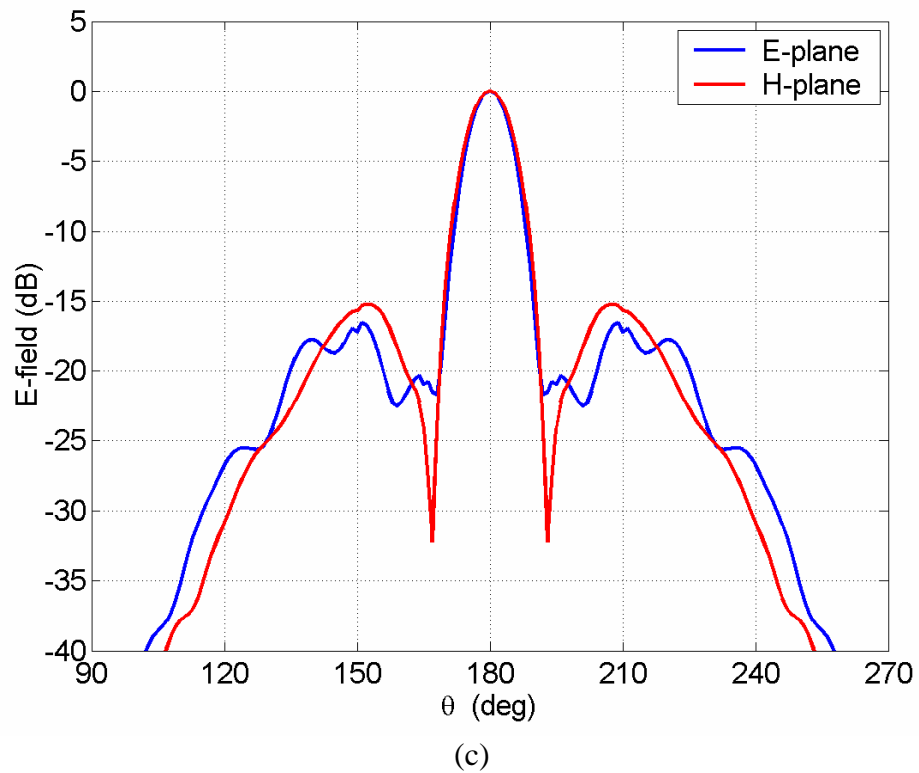
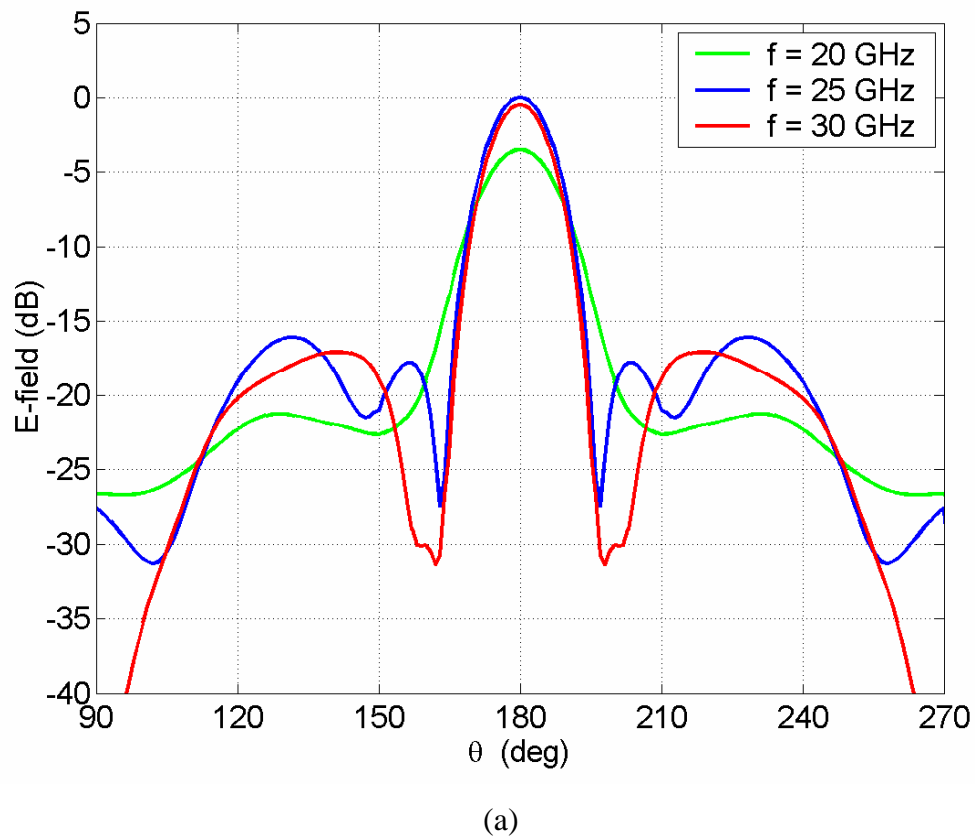


Figure 4.17. Normalized radiation patterns of the reflector system described in Table 4. The working frequency is 25.4 GHz; (a) case 1, (b) case 2, (c) case 3.



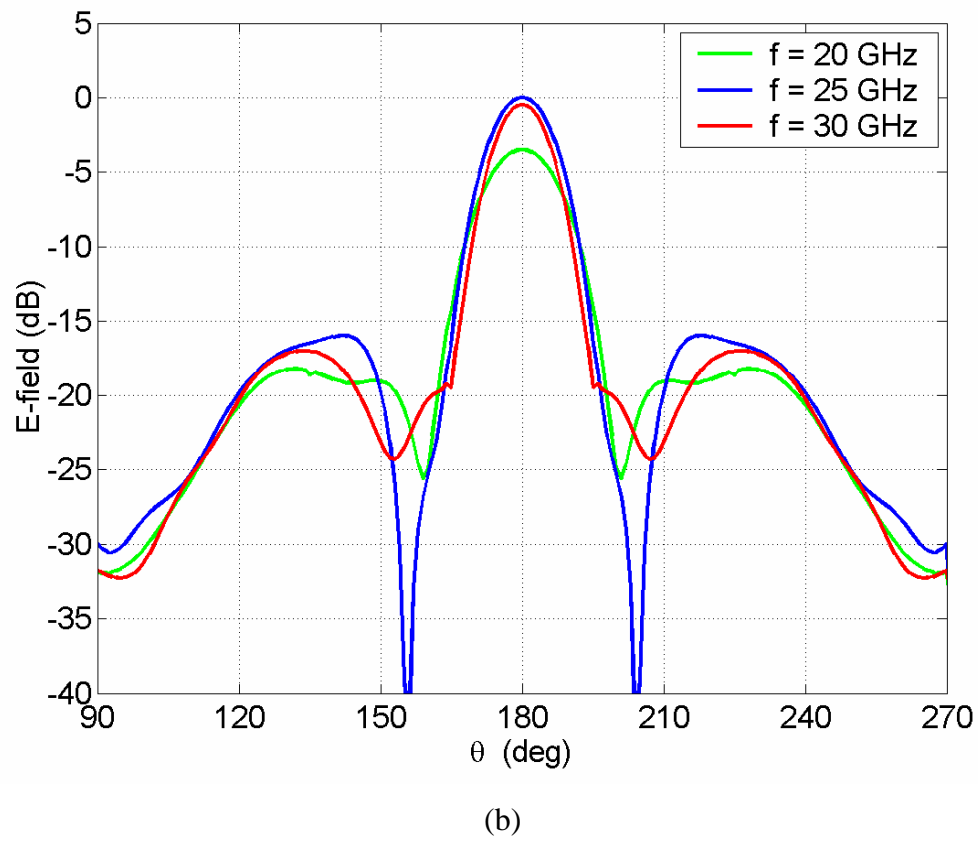


Figure 4.18. Frequency dependence of the radiation pattern of the reflector system. The spherical FSS is described in Table 4 (case 1); (a) E-plane, (b) H-plane.

As an example of the dual case, an annular slot FSS radome, we have considered an array of annular slots of average radius 2.0 mm (i.e. to the center of the slot; the slot width was 0.4 mm), and separation between annular slot centers is 4.9 mm. The slots are printed in a spherical ground plane placed on a dielectric substrate of thickness 0.0075 mm and permittivity $\epsilon_r = 2.33$. The annular slots follow the triangular grid. Inside the radome there is a horn with symmetric linearly polarized radiation pattern whose -10 dB beamwidth is 60° . The horn is placed in the origin of the coordinate system, i.e. the distance to all annular slots is the same.

In Fig. 4.19 two cases are considered: a radome with radius $r_{\text{slot}} = 18.7$ mm with 6 circles of slots around the central slot element placed at the apex (i.e. the hemispherical structure; the structure contains 109 slots), and a radome with radius $r_{\text{slot}} = 37.4$ mm with 8 circles of slots around the central slot element placed at the apex (the conical angle of the area containing annular slots is 60° ; the structure contains 217 slots).

Fig. 4.19 shows the comparison of the radiation patterns of the horn & radome structure (both in the E- and H-planes) and of the horn without the radome. The working frequency is $f = 25$ GHz. It can be seen that there is a large difference between the radiation patterns if the radome is included into the analysis. This difference is also strongly frequency depended; see Fig 4.20, where the radiation pattern of the horn & radome structure is given for different frequencies for the hemispherical slotted structure. These results indicate that the frequency selective radome requires a careful design if we want to obtain the radome that does not disturb the radiation pattern of the primary feed antenna.

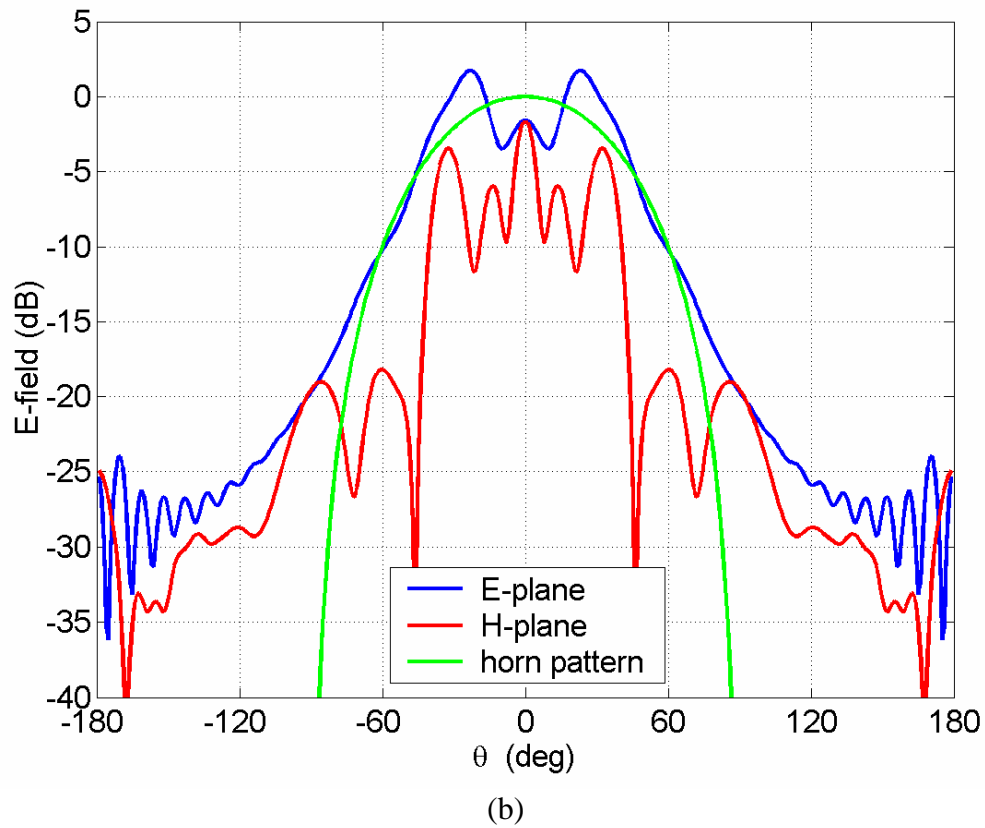
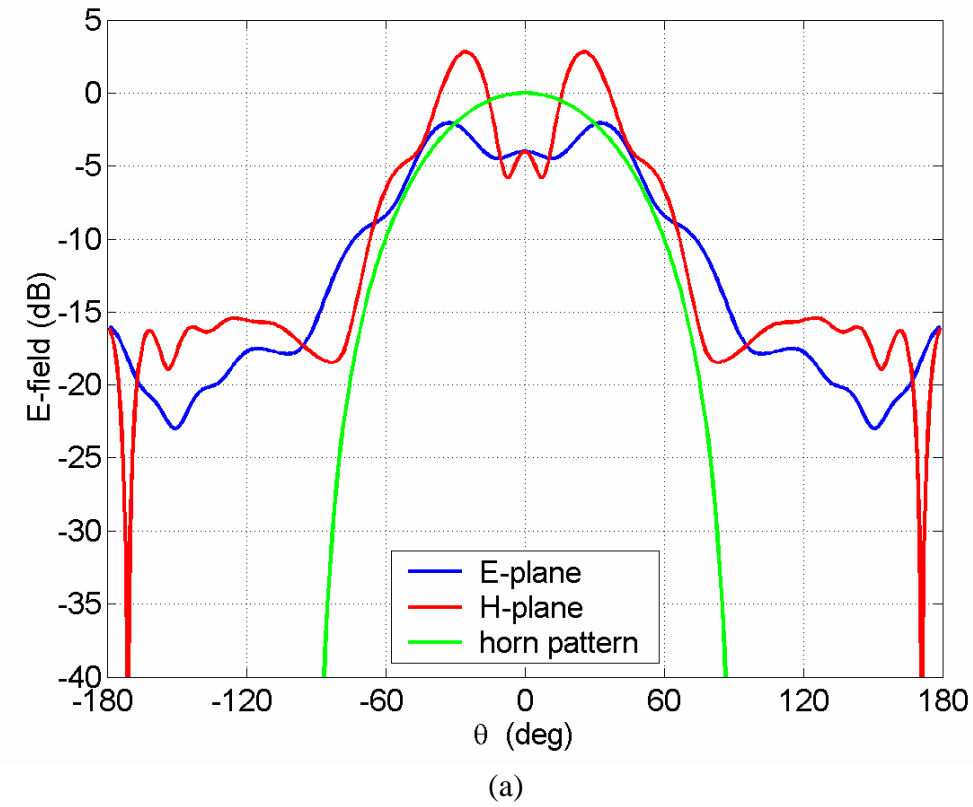


Figure 4.19. The radiation pattern of the horn with a spherical FSS radome in both E- and H-planes. For comparison the radiation pattern of the horn without radome is also given. The working frequency is $f = 25$ GHz. (a) $r_{\text{slot}} = 18.7$ mm (b) $r_{\text{slot}} = 37.4$ mm.

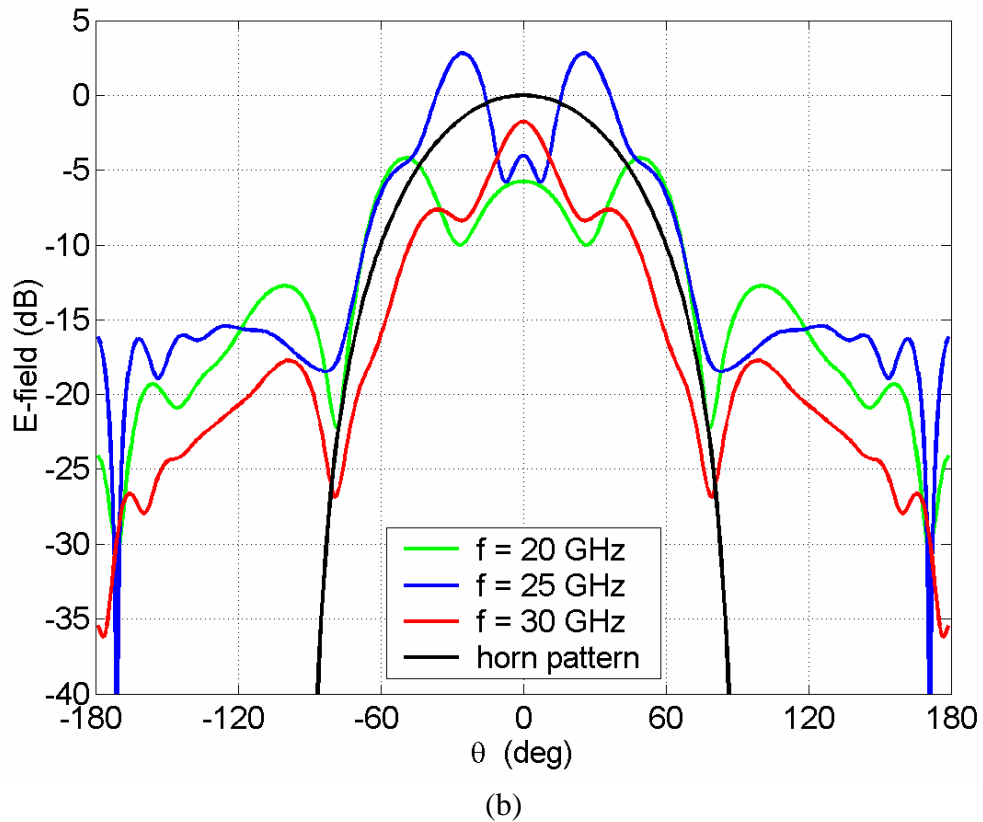
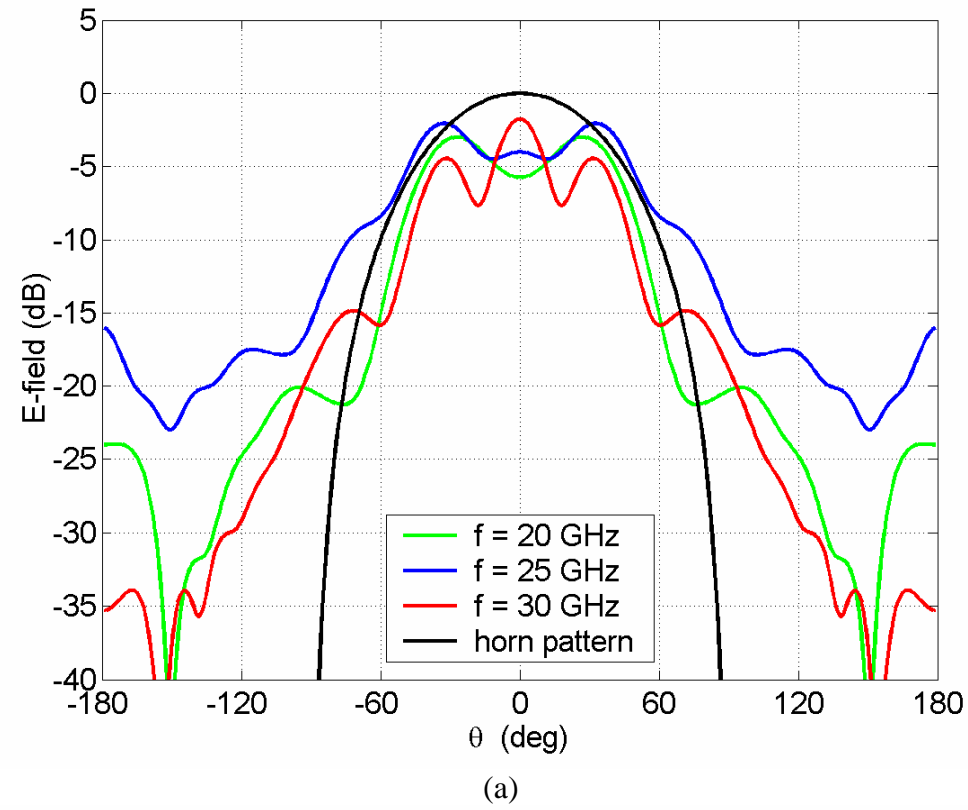


Figure 4.20. The radiation pattern of the horn with a spherical FSS radome as a function of frequency. The radius of the structure is $r_{\text{slot}} = 18.7$ mm. For comparison the radiation pattern of the horn without radome is also given. The working frequency is $f = 25$ GHz. (a) E-plane, (b) H-plane.

4 CONCLUSIONS

Conclusions

During the 12 months assigned to this project the software for the analysis of curved frequency selective surfaces (curved FSS) was developed. Both single and double curved structures can be analyzed, and also there is a possibility to use patches or apertures as the FSS elements. The proposed building elements of the FSS are circular metallic rings due to their good polarization and resonant frequency properties, and by using this elements all the possibilities of this software were shown. Most importantly, the following characteristics can be obtained: (a) reflection (radar cross-section) from the curved structure, (b) transmission (radiation pattern) through the curved structure, and (c) losses due to the periodic structure.

The basic idea of the proposed analysis model is to approximate the curved structure with overlapping subarrays - spherical periodic structures of an appropriate (local) radius of curvature. The influence of the overlapping subarray size and the number of overlapping elements on the FSS characteristics have been analyzed and it is shown that at least two circles of FSS elements around the central element are needed for good approximation of the current.

The individual spherical subarrays are analyzed using the Method of Moments (MoM) in the spectral domain. This analysis has been accelerated using a new technique for calculating the mutual coupling in which two additional potential-like auxiliary functions are defined, containing the information about the coordinates only in respective arguments of the product of Legendre and exponential functions. Consequently, this term can be transformed from one coordinate system to another very simply, by use of the additional theorem for associated Legendre functions. The importance of rigorous analysis of mutual coupling effects is demonstrated on several examples.

A significant acceleration of the algorithm is achieved using a newly developed hybrid method for the calculation of the MoM impedance/admittance matrix terms. The developed method combines the spectral domain approach with a free space method or Uniform Theory of Diffraction (UTD) in order to simplify and accelerate the calculation of the highly oscillating integrals, which need to be evaluated in the MoM analysis. Major benefit of this hybrid method is that it can be applied to very large multilayered structures (i.e. structures with large radii) and provide the results reasonably fast.

The realized outcomes of the project are:

- Program “cFSS” that analyzes spherical frequency selective periodic structures consisting of circular ring elements. Circular rings as elements for building curved FSS were selected due to their good polarization and resonant frequency properties. The program calculates:
 - Current distribution at each ring in the subarray of the analyzed FSS without mutual coupling taken into account,
 - Current distribution at each ring in the subarray of the analyzed FSS with mutual coupling between the ring elements rigorously taken into account,
 - Scattered field of the analyzed subarray with and without mutual coupling taken into account,
 - Transmission coefficient of the analyzed subarray,
 - Electromagnetic properties of the whole curved FSS structure, obtained by calculating scattered electromagnetic field of the whole FSS (the needed current distribution is obtained by solving a set of subarray problems),
 - Radiation pattern of the FSS reflector system where the primary feed is characterized with the known far-field radiation pattern,
 - Radiation pattern of the FSS radome system where, as FSS elements, circular annular apertures are considered (so-called dual problem).

5 Bibliography

- [1] Josefsson, L., and Persson, P.: ‘Conformal Array Antenna Theory and Design’ (Wiley - IEEE Press, 2006).
- [2] Tomasic, B., Turtle, J., and Liu, S.: ‘A geodesic sphere phased array for satellite control and communication’, International Union of Radio Science, XXVIIth General Assembly, Maastricht, The Netherlands, August 2002.
- [3] Tomasic, B., Turtle, J., and Liu, S.: ‘Spherical arrays – design considerations’, Proceedings of *18th International Conference on Applied Electromagnetics and Communications, (ICECOM'05)*, Dubrovnik, Croatia, 2005, 487-493.
- [4] Rahmat-Samii, Y. and Tulinsteff, F.: ‘Diffraction analysis of frequency selective surface antenna,’ *IEEE Trans. on Antennas and Propagat.*, 1993, **Vol. 41**, pp. 476-482.
- [5] Parker, E. A., and Hamdy, S. M. A., ‘Rings as elements for frequency selective surfaces,’ *Electronics Letters*, **vol. 17**, pp. 612-614, (1981).
- [6] Harrington, R.F.: ‘Time-harmonic electromagnetic waves’ (McGraw Hill, New York, 1961).
- [7] Sipus, Z., Kildal, P.-S., Leijon, R. and Johansson, M.: ‘An algorithm for calculating Green’s functions for planar, circular cylindrical and spherical multilayer substrates,’ *Applied Computational Electromagnetics Society Journal*, 1998, **vol. 13**, pp. 243-254.

- [8] Tam, W.Y., and Luk, K.M.: 'Resonances in spherical-circular microstrip structures of cylindrical-rectangular and wraparound microstrip antennas,' *IEEE Trans. Microwave Theory Tech.*, 1991, **Vol. 39**, pp. 700-704.
- [9] Sipus, Z., Burum, N., Skokic, S., and Kildal, P.-S.: 'Analysis of spherical arrays of microstrip antennas using moment method in spectral domain,' *IEE Proceedings - Microwaves, Antennas and Propagation*, 2006, **Vol. 153**, pp. 533-543.
- [10] Tam, W.Y., and Luk, K.M.: 'Far field analysis of spherical-circular microstrip antennas by electric surface current models,' *IEE Proceedings - Microwaves, Antennas and Propagation*, 1991, **Vol. 138**, pp. 98-102.
- [11] Sengupta, D. L., Smith, T. M., and Larson, R. W.: 'Radiation Characteristics of Spherical Array of Circularly Polarized Elements,' *IEEE Trans. on Antennas and Propagat.*, 1968, **Vol. 16**, pp. 2-7.
- [12] Vilenkin, N. Ja.: 'Special Functions and the Theory of Group Representation,' (American Mathematical Society, Providence, 1968).
- [13] Sipus, Z., and Skokic, S.: 'Application of Vilenkin's additional theorem in the analysis of spherical antennas and periodic structures,' *Proceedings of the 1st European Conference on Antennas and Propagation*, Nice, France, 2006, paper 363810zs in CD.
- [14] Savia, S.B., Parker, E. A., and Philips, B.: 'Finite planar- and curved-ring-element frequency-selective surfaces,' *IEE Proceedings - Microwaves, Antennas and Propagation*, 1999, **Vol. 146**, pp. 401-406.
- [15] Pozar, D.M.: 'Improved computational efficiency for the moment method solution of printed dipoles and patches,' *Electromagnetics*, 1984, **Vol. 3**, No. 3&4, pp. 299-309.
- [16] Kildal, P.-S.: '*Foundations of Antennas - A Unified Approach*,' Studentlitteratur AB, 2000.
- [17] Stutzman, W.L., Thiele, G.A.: *Antenna Theory and Design*, Wiley, 1998.
- [18] Hansen, J.E, (editor): *Spherical near-field antenna measurements*, Peregrinus Ltd., 1988.
- [19] Pathak, P.H., Wang, N.: 'Ray analysis of Mutual Coupling Between Antennas on a Convex Surface,' *IEEE Trans. Antennas Propagation*, 1981, **Vol. AP-29**, No. 6, pp. 911-922.
- [20] Bosiljevac, M., Persson, P., Sipus, Z.: 'Hybrid spectral domain - UTD method applied to conformal antenna analysis,' *Proceedings of the European Conference on Antennas and Propagation EuCap 2006*, Nice, 2006.
- [21] Ishihara, T., Felsen, L.B., Green, A.: 'High-Frequency Fields Excited by a Line Source Located on a Perfectly Conducting Concave Cylindrical Surface', *IEEE Trans. Antennas Propagation*, 1978., **Vol. AP-26**, No. 6, pp.757-767.
- [22] Abramowitz, M., and Stegun, I.: '*Handbook of mathematical functions*' Dover, 1965.

6 APPENDIX

6.1 cFSS program - text file interface

The programs cFSS and cFSSpat, developed for the analysis of spherical frequency selective surfaces (FSS), interact with the user and with each other using ASCII text files. This scheme, with all files in question is presented in Fig. 6.1.

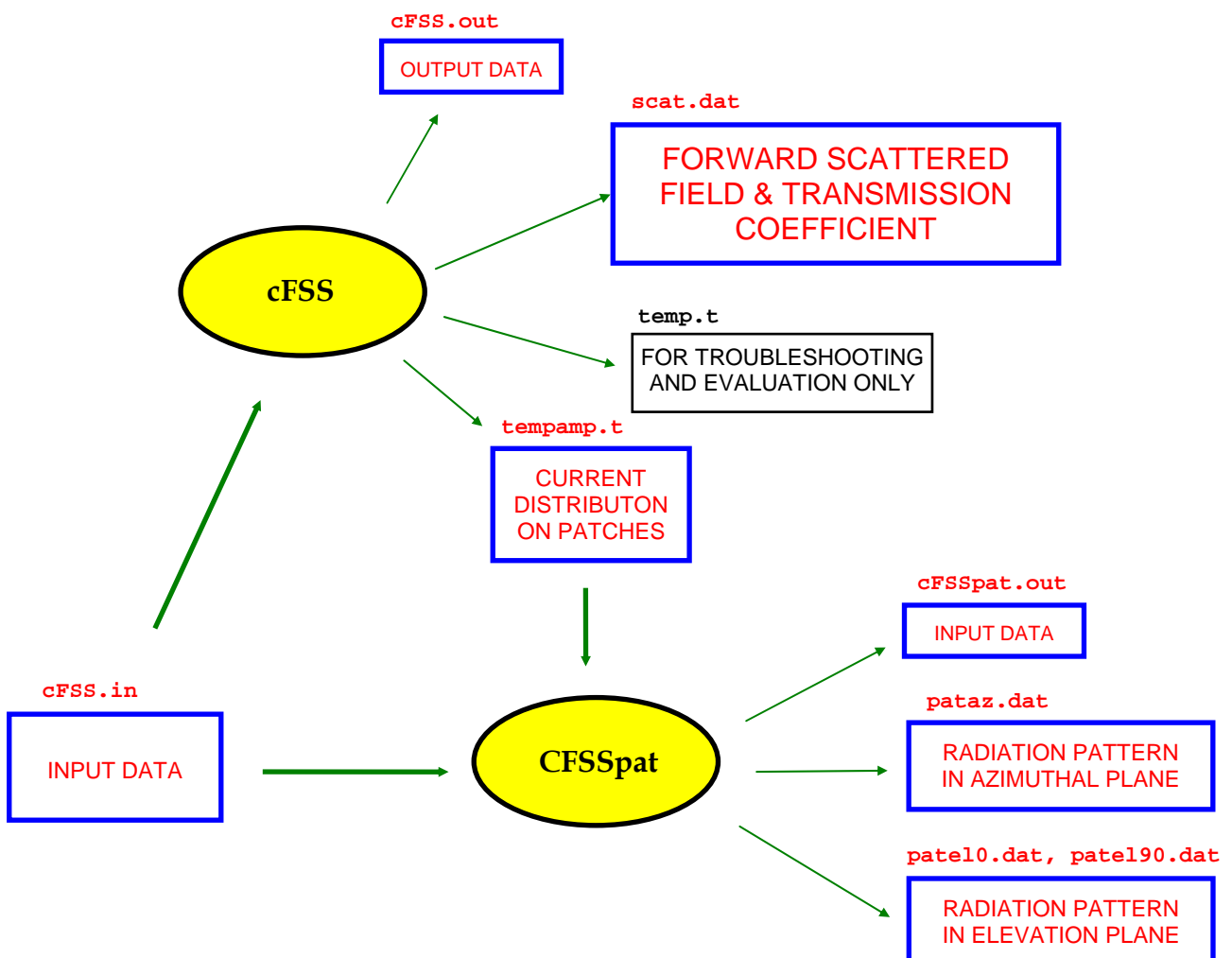


Figure 6.1. Input and output files for the programs cFSS and cFSSpat.

6.1.1 The cFSS.in file

The name of the input file for both cFSS and cFSSpat programs is **cFSS.in**. Each line possesses the value of several variables and short description of these variables. Since our intention was to make a compatible program with previously developed programs cFSS/cFSSpat we have decided to use the input/output files with the same names and structures. The parts of the input/output files that have different meaning are written in bold letters. The input variables, which must have values when the call of the cFSS and cFSSpat is made, are:

First line:

Fmin, Fmax, Nfrequency, Modecal REAL, REAL, INTEGER, CHARACTER

Fmin and *Fmax* are the minimum and maximum frequency (in GHz). *Nfrequency* is the number of frequency points for which the array is analyzed. These values are used only when the call of the SMiSPA program is made. cFSSpat program calculates the radiation pattern only for one frequency, and that frequency is *Fmin*. If we first calculate the patch currents at *Nfrequency* frequency points (by calling cFSS program), then we can choose the frequency point for which we want to calculate the radiation pattern by choosing *Fmin*. The only condition is that the patch currents are calculated for the chosen frequency point.

Second line:

R_{in} REAL

R_{in} is the inner radius of the structure (in cm).

Third line:

Nlayer INTEGER

Nlayer is the number of dielectric layers.

Next *Nlayer* lines:

h, EpsilonR, Tdelta REAL

Each line contains three parameters: *h*, *EpsilonR* and *Tdelta* that describe the thickness, the relative permittivity and loss tangent of each dielectric layer, respectively.

Next line:

Npatlayer INTEGER

Npatlayer is the numbers of the dielectric layer at top of which the patches (elements of the FSS structure) are placed. In other words, the patches are placed between dielectric layers *Npatlayer* and *Npatlayer*+1. If the patches are placed in the middle of some dielectric layer, an additional dielectric layer should be introduced, i.e. the considered dielectric layer should be split into two parts and the patches should be placed at the interface between these two dielectric layers.

Next line:

Npat1, Npat2, Lattice INTEGER, CHARACTER

Lattice represents the type of the grid lattice – *H* means hexagonal lattice, *I* means icosahedron lattice, *R* means rectangular lattice, and *F* means that the position of each patch is read at the end of the input file. For hexagonal and icosahedron lattice *Npat1* is the number of circles of elements in the array, and *Npat2* denotes the ratio between the sides of equilateral triangles of the hexagonal/icosahedron structure and of the considered array (for example, *Npat1*=3 and *Npat2*=4 means that angle between circles of FSS elements is $60/4 = 15^\circ$, and that we have $1 + 6 + 12 = 19$ elements in the array). For rectangular lattice *Npat1* and *Npat2* are the number of patches in the θ - and ϕ -directions, respectively. If the patch position is read from the file, then *Npat1* and *Npat2* have no meaning and therefore they can have arbitrary values.

Next line:

Dpat1, Dpat2 REAL

Dpat1 and *Dpat2* denote the inner and outer diameter of the rings (in cm), respectively.

Next line:

Dpatth, Dpatphi REAL

In the case of rectangular array grid (i.e. if the variable *Lattice* is equal *R*) *Dpatth* and *Dpatphi* are the distances between centers of the patches (in cm) in the θ - and ϕ -directions, respectively. If the variable *Lattice* is equal *H*, *I* or *F*, this line has no meaning and thus

Dpatth and *Dpatphi* can be arbitrary numbers.

Next line:

Modeexci CHARACTER

Modeexci determines the type of excitation: *P* or *p* means the plane wave excitation (traveling along the z-axis towards $-\infty$), *H* or *h* means that the curved FSS is excited by a horn.

Next line:

α_1, α_2 , PatternMode REAL

This line is characterization of the feed (horn) antenna: α_1 and α_2 are the exponentials in the far-field approximation of the primary feed (horn antenna), see eq. (27). *Patternmode* represents the mode of calculating radiation pattern: *Patternmode* = 1 means that both the incident (primary antenna) field and the scattered field (from curved FSS) are calculated, *Patternmode* = 0 means that only the scattered field (from curved FSS) is calculated, *Patternmode* = -1 means that only the incident field from the primary (horn) antenna is calculated. If the array is excited by the plane wave, this line has no meaning.

The next six lines are needed only when the call of the cFSSpat program is made. They are:

<u>Phimin, Phimax, Nphi</u>	<u>REAL, REAL, INTEGER</u>
	The minimum and maximum angles of ϕ (in deg) in the azimuthal plane, and the number of points that are calculated in the azimuthal pattern, respectively. The azimuthal plane is defined by $\theta = 90^\circ$.
<u>Thetamin, Thetamax, Ntheta</u>	<u>REAL, REAL, INTEGER</u>
	The minimum and maximum angles of θ (in deg) in the elevation plane, and the number of points that are calculated in the elevation pattern, respectively.
<u>Theta0, Phi0</u>	<u>REAL</u>
	The values of the θ and ϕ coordinates (in deg) of the main beam, respectively. The E-field values of the radiation pattern are normalized by the amplitude of the E-field with <i>Theta0</i> and <i>Phi0</i> coordinates.
<u>Typepolar</u>	<u>CHARACTER</u>
	<i>Typepolar</i> denotes the type of polarization of radiation pattern. <i>L</i> or <i>l</i> means linear polarization, <i>C</i> or <i>c</i> means circular polarization.

If needed (i.e. if *Lattice* = *F*), next *Npat* x *Nport* lines after one blank line are:

<u>Thetapat, Phipat</u>	<u>REAL, INTEGER, REAL</u>
	<i>Thetapat</i> and <i>Phipat</i> represent the θ and ϕ coordinate (in degrees) of the center of each FSS element.

6.1. 2 Description of the output files

There are six output files: 'cFSS.out', 'cFSSpat.out', 'Scat.dat', 'PatAz.dat', 'PatEl0.dat' and 'PatEl90.dat', and in them we can find data about the geometry as well as the calculated values of the forward scattered field (i.e. of the transmission coefficient), and of the radiation pattern in the elevation and azimuthal planes.

cFSS.out - output file of the cFSS program. The file contains data about the array geometry. The first part of the file contains the values of the input file. Therefore, it looks similar to the input file 'cFSS.in'. The second part contains the calculated forward scattered field and the transmission coefficient. The first column is the working frequency (in GHz), the second column is the calculated transmission coefficient (in dB), the third and fourth column are the amplitude

(in dB) and the phase of the forward scattered field, and the fifth and sixth column are the amplitude (in dB) and the phase of the backward scattered field.

cFSSpat.out - output file of the cFSSpat program. The file contains data about the array geometry. The first part of the file contains the values of the input file. Therefore, it looks similar to the input file 'cFSS.in'. The second part describes the array that is analyzed. It is a list of the all patch elements in the array with their coordinates and amplitude and phase of the patch current. First two columns are the patch number-coordinates, the third column is the number of the basis function on the considered patch, and the forth and fifth columns are the θ and ϕ coordinate of the patch. The sixth and seventh columns are the amplitude and phase (in deg) of the considered basis function, respectively.

Scat.dat - output file of the cFSS program. The file contains the calculated forward scattered field and the transmission coefficient. The first column is the working frequency (in GHz), the second column is the calculated transmission coefficient (in dB), the third and fourth column are the amplitude (in dB) and the phase of the forward scattered field, and the fifth and sixth column are the amplitude (in dB) and the phase of the backward scattered field.

PatAz.dat - output file of the cFSSpat program. The file contains the field values in the azimuthal plane (the azimuthal plane is defined by $\theta = 90^\circ$). The input values of variables *Phimin*, *Phimax* and *Nphi* determine the ϕ values in the azimuthal plane for which the radiation pattern is calculated. The field values are normalized with the field value with *Theta0* and *Phi0* coordinates that are defined in the input file. The first and second columns are the θ and ϕ coordinates (in deg) for which the radiation pattern is calculated. If the chosen type of polarization is linear (parameter *Typepolar* in the input file), then the third and the fourth columns are the normalized θ and ϕ -components of the electric field, respectively. If the chosen type of polarization is circular, then the third and the fourth columns are the normalized right-hand circular polarization (RHCP) and left-hand circular polarization (LHCP) components of the electric field, respectively.

PatEl0.dat - output file of the cFSSpat program. The file contains the field values in the elevation plane which is defined by $\phi = 0^\circ$. The input values of variables *Thetamin*, *Thetamax* and *Ntheta* determine the θ values in the elevation plane for which the radiation pattern is calculated. The field values are normalized with the field value with coordinates *Theta0* and *Phi0* that are defined in the input file. The first and second columns are the θ and ϕ coordinates (in deg) for which the radiation pattern is calculated. If the chosen type of polarization is linear (parameter *Typepolar* in the input file), then the third and the fourth columns are the normalized θ and ϕ -components of the electric field, respectively. If the chosen type of polarization is circular, then the third and the fourth columns are the normalized right-hand circular polarization (RHCP) and left-hand circular polarization (LHCP) components of the electric field, respectively.

PatEl90.dat - output file of the cFSSpat program. The file contains the field values in the elevation plane which is defined by $\phi = 90^\circ$. The input values of variables *Thetamin*, *Thetamax* and *Ntheta* determine the θ values in the elevation plane for which the radiation pattern is calculated. The field values are normalized with the field value with coordinates *Theta0* and *Phi0* that are defined in the input file. The first and second columns are the θ and ϕ coordinates (in deg) for which the radiation pattern is calculated. If the chosen type of polarization is linear (parameter *Typepolar* in the input file), then the third and the fourth columns are the normalized

θ - and ϕ -components of the electric field, respectively. If the chosen type of polarization is circular, then the third and the fourth columns are the normalized right-hand circular polarization (RHCP) and left-hand circular polarization (LHCP) components of the electric field, respectively.